Contents

List of Figures

List of Tables

Introduction

During the last few years the neutrino scenario has dramatically changed. Atmospheric neutrino [50], solar neutrino [51] and reactor antineutrino [53] [1] experiments have given model independent evidences of neutrino oscillations.

In this scenario there are two general theoretical possibilities for massive neutrinos, depending on the conservation or not of the total lepton charge. In the first case neutrinos are Dirac particles, while in the second they are Majorana particles. At the moment the question about the neutrino nature is still without an answer. The solution of the problem of the nature of the massive neutrinos will be of fundamental importance to understand the origin of the small neutrino masses and of the pattern of neutrino mixing. The investigation of neutrino oscillations does not allow to solve this problem.

Experiments looking for the DBD0ν of even-even nuclei have the highest sensitivity to possible violations of the total lepton number L and to Majorana neutrino masses. DBD0ν experiments try to measure the effective Majorana electron neutrino mass $|< m_\nu >|$ by measuring the rate of the DBD0ν transition. Unfortunately the calculations of the nuclear matrix elements presently available [21] [10] [43] [6] show a spread of results, due to different models and hypothesis used for their computation. To overcome this problem it is fundamental to search for DBD0ν on several nuclei [7].

DBD0ν can be searched for with different experimental methods. One possible direct approach is based on the bolometric technique. The energy released in dielectric and diamagnetic crystals gives rise to measurable temperature increases when working at low temperature (T $\sim$10 mK). Cryogenic detectors offer therefore a wide choice of DBD candidates. The isotope ^{130}Te is and excellent candidate to search for DBD due to its high transition energy (2528.8 $\pm$1.3 keV) and large isotopic abundance (33.8%) which allows a sensitive experiment to be performed with natural tellurium. Of the various compounds of this element, TeO$_2$ appears to be the most promising, due to its good thermal and mechanical properties.

Because of the rarity of the searched process, spurious counts due to environmental radioactivity, intrinsic contaminations and cosmic ray activation of the detector and of the other experimental setup materials, airbone activity (Rn) and neutrons can obscure the signal counts of interest. A good knowledge of the radioactive sources that mainly contribute to the measured background in the DBD0ν energy region, is therefore of fundamental importance in order to study new strategies to reduce such contaminations and consequently improve the sensitivity of the experiment.

This PHD thesis work was focused on the analysis of the data collected with two bolometric experiments, aimed to search for the DBD0ν of the isotope ^{130}Te . It mainly consisted in the development of a background model, able to describe the observed spectra in terms of environmental radioactivity, radioactive bulk contaminations of the whole detector setup and surface contaminations of the material directly facing the detector itself. The developed model is based both on the analysis of the collected data by means of sophisticated analysis procedures and on the direct comparison between measured and Montecarlo simulated spectra. The Montecarlo spectra are obtained

by means of a C++ code, based on the Geant4 package. With this code it is possible to simulate detected events due to radioactive contaminations of the environment or of the various experimental parts. Different detector geometries has been introduced in the code, in order to account for the different structures of the analyzed experiments. The first large mass array (MiDBD experiment) to which the present PHD research activity has been devoted, consisted of 20 TeO$_2$ bolometers of 340 g each ($3\times3\times6$ cm^3 crystals), four of which isotopically enriched (two enriched in Te^{128} and two in ^{130}Te with isotopic abundance of 82.3% and 75% respectively), for a total TeO$_2$ mass of 6.8 kg. It was operated since 1997 in the hall A of the National Laboratories of Gran Sasso (LNGS). From the analysis of the background data of this experiment we gained a better knowledge of the radioactive sources responsible of the measured background, which induced us to develop a radiopure cleaning process for the surfaces of the detectors and of all the experimental parts facing them. The developed cleaning process was adopted in the rebuilding of the MiDBD experiment performed at the end of 2000. The detector was completely rebuilt with a new structure, similar to the one foreseen for the CUORICINO and CUORE experiments, and this allowed to improve the internal roman lead shield. The background spectra measured in both the MiDBD runs were analyzed and by the comparison between them we could verify the effectiveness in reducing the backgroun of the cleaning procedure adopted.

The MiDBD experiment was completed in 2001. It was replaced by the larger mass experiment CUORICINO. The CUORICINO detector is a tower-like structure made by eleven planes of 4-crystal modules ($5\times5\times5$ cm^3 crystals of 790 g mass each) and two additional planes of 9-crystal modules ($3\times3\times6$ cm^3 crystals of 330 g mass each), for a total TeO$_2$ mass of 40.7 kg. All the crystals are made of natural tellurium but 4 isotopically enriched crystals (the ones already used in MiDBD). With the appropriate new detector geometry, the background model developed for MiDBD was used also to analyze the data acquired with CUORICINO.

This same background model, after a correct implementation of the new detector geometry, was used also to evaluate the experimental sensitivity of the next generation experiment CUORE. The CUORE project is a bolometric detector made by about 1000 TeO$_2$ $5\times5\times5$ cm^3 crystals, arranged in a cylindrical structure of 19 towers. Each tower consistes of 13 planes each, similar to those used in CUORICINO. The designed detector should be able to reach the sensitivity in the range 0.01 eV to the present upper bounds. From the analysis of the background measured with MiDBD-I, MiDBD-II and CUORICINO, important informations have been obtained in terms of materials contaminations and contributions to the background in the DBD0ν energy regions of the performed experiments. These informations have been used to evaluate by means of the Montecarlo code the background level expected in CUORE when using the materials presently at our disposal. At the same time the Montecarlo code has been used to evaluate the maximum contamination level acceptable for every single experimental part in order to reach the required sensitivity. A plan of material selection and radioactive measurements was therefore developed.

Chapter 1

Neutrino Physics scenario

Introduction

In 1930 W.Pauli postulated the existence of the neutrino in order to reconcile data on the radioactive decay of nuclei with energy conservation. The postulated neutrino was a massless or very light neutral particle and just served to balance energy and momentum in beta decays. The first theory about this nuclear decay was published in 1934 by E.Fermi. In 1959 the first direct observation of electron antineutrino form a nuclear reactor was performed by F.Reines and C.Cowan. By the 1960 's neutrino beams became one of the most important tools of particle physics and leaded to the discovery of the muon neutrino.

Neutrinos are also produced in natural sources. Starting in the 1960 's, neutrinos produced in the sun and in the atmosphere have been observed. In 1987, neutrinos from a supernova in the Large Magellanic Cloud were also detected.

The properties of the neutrino and in particular the question of its mass have intrigued physicists mind ever since it was proposed.

In the laboratory neutrino masses have been searched for in two types of experiments: direct kinematic searches of neutrino mass and neutrinoless double beta decay (DBD0ν) experiments.

In 1957 B.Pontecorvo realized that the existence of neutrino masses would imply the possibility of neutrino oscillations. Neutrino flavor oscillation have been searched for using either neutrino beams from reactors or accelerators, or natural neutrinos generated at astrophysical sources or in the atmosphere. In the last years, experiments studying natural neutrino fluxes have provided us with the strongest evidence of neutrino masses and mixing.

The discovery of neutrino oscillations and the consequent a non-vanishing neutrino masses give strong indications for theoretical physics beyond the Standard Model (SM).

The first part of this chapter will be devoted to an introduction to neutrino mass theory, from the SM to neutrino oscillation. In the second part the experimental data and the actual scenario for neutrino physics will be overviewed.

1.1   The standard Model and Neutrino masses

The Standard Model of particle physics represents our comprehensive description of the strong, weak and electromagnetic interactions. Since it was conceived in the 1960 's by Glashow, Salam and Weinberg, it has successfully passed numerous experimental tests. It is based on a gauge theory

that assumes local gauge invariance of the Lagrangian under transformations

$$SU(3)_c \times SU(2)_L \times U(1)_Y \tag{1.1}$$

Since in this theory all the fundamental particles are fermions, they are described by the Dirac Lagrangian as:

$$L_l = \bar{\psi}_i(x)[i\gamma^\mu \delta_\mu - m]\psi_i(x) \tag{1.2}$$

where ψ_i is the fermion field operator.

In the absence of any direct evidence for their mass, neutrinos were introduced in the SM as massless fermions for which no gauge invariant renormalizable mass term could be constructed. They are singlets of $SU(3)_c \times U(1)_{em}$, and are supposed to interact only via weak interactions. The SM has three active neutrinos, accomodated in lepton doublets,

$$L_l = \begin{pmatrix} \nu_{Ll} \\ l_L \end{pmatrix}, \quad l = e, \mu, \tau \tag{1.3}$$

where e, μ, τ are the charged lepton mass eigenstates. In this scenario the charged current (CC) interaction terms for leptons are

$$-L_{CC} = \frac{g}{\sqrt{2}} \sum_l \overline{\nu_{Ll}} \gamma^\mu l_L^- W_\mu^+ + h.c. \tag{1.4}$$

In addition the SM neutrinos have neutral current (NC) interactions

$$-L_{NC} = \frac{g}{2cos\theta_W} \sum_l \overline{\nu_{Ll}} \gamma^\mu \nu_{Ll} Z_\mu^0 + h.c. \tag{1.5}$$

1.1.1 The see-saw mechanism

After the results from the oscillation experiments various theories trying to explain the origin of neutrino masses were developed. Recent measurements [2] have constrained the sum of the flavor neutrino masses to 700 meV farther below the other fermion masses. The smallness of the neutrino mass is difficult to be explained in a SM approach, but can be derived in different extensions of the SM, like in GUTs or in the left-right symmetric gauge theories.

Left-right symmetric theories are based on the group SU(2)$_L \times$ SU(2)$_R \times$ U(1), where SU(2)$_L$ is referred to as the left-handed isospin I$_L$ group associated to a boson W_L, and the SU(2)$_R$ as the right-handed isospin I$_R$ group associated to a boson W_R. The left-handed and right-handed quarks and leptons are arranged in SU(2)$_L$ and SU(2)$_R$ doublets respectively:

$$\begin{pmatrix} u_L \\ d_L \end{pmatrix}, \quad \begin{pmatrix} \psi_L \\ e_L \end{pmatrix} \tag{1.6}$$

for the left-handed fermions, and

$$\begin{pmatrix} u_R \\ d_R \end{pmatrix}, \quad \begin{pmatrix} \psi_R \\ e_R \end{pmatrix} \tag{1.7}$$

for the right-handed fermions, where ψ_L and ψ_R are the left-handed and right-handed ν_e fields respectively, arising from the left and right handed projection of the Dirac field ψ:

$$\psi_{L,R} \equiv P_{L,R}\psi \tag{1.8}$$

2

where $P_{L,R} \equiv \frac{(1\pm\gamma_5)}{2}$ is the left-right projection operator. If we would assume that $\psi_{R,L}$ are Dirac fields the Lagrangian density will include a mass term of the form:

$$-L_m = M\bar{\psi}\,\psi = M(\bar{\psi}_R\,\psi_L + h.c.) \tag{1.9}$$

that leads, via the introduction of the Higgs scalar field ϕ and the spontaneous symmetry breaking mechanism, to the usual mass term for fermions in the Dirac equation. If we derive the neutrino mass in this way there is no reason for the neutrinos having a mass smaller than the other fermions. To overcome this problem we need to find other bilinear products involving ψ_L and ψ_R that conserve the invariance of the Lagrangian. This is obtained in the see-saw mechanism, based on the left-right symmetric model, by introducing two more Higgs fields, Δ_L and Δ_R are introduced, with properly chosen quantum numbers. Since $\psi_{L(R)}$ is in an $SU(2)_{L(R)}$ doublet it has quantum numbers $I_{L(R)} = 1/2$ and $I_{R(L)} = 0$. Therefore, the bilinear products involving ψ_L and ψ_R have the following quantum numbers:

$$\begin{aligned}
\bar{\psi}_R\psi \, has \, I_L &= 1/2 & I_R &= 1/2; \\
\overline{(\psi_L)^c}\psi_L \equiv \psi_L^t\Omega\psi_L \, has \, I_L &= 1 & I_R &= 0; \\
\overline{(\psi_R)^c}\psi_R \equiv \psi_R^t\Omega\psi_R \, has \, I_L &= 0 & I_R &= 1;
\end{aligned} \tag{1.10}$$

where $\omega = i\gamma_2\gamma_0$ with γ_2 and γ_0 two of the Dirac matrices. These terms, with constant coefficients, are forbidden by the $SU(2)_L \times SU(2)_R \times U(1)$ invariance of the Lagrangian. However, allowed terms (with total $I_L = L_R = 0$) may be constructed by coupling these bilinears to the Higgs fields Φ, Δ_L and Δ_R with quantum numbers:

$$\begin{aligned}
\Phi &: I_L = 1/2 & I_R &= 1/2; \\
\Delta_L &: I_L = 1 & I_R &= 0; \\
\Delta_R &: I_L = 0 & I_R &= 1;
\end{aligned} \tag{1.11}$$

Therefore the only possible bilinear products of ψ_L and ψ_R that are Lorentz invariant are three Yucawa couplings to the neutrino fields:

$$\bar{\psi}_R\phi\psi_L \;\; , \;\; \overline{(\psi_L)^c}\delta_L\psi_L \;\; , \;\; \overline{(\psi_R)^c}\delta_R\psi_R \tag{1.12}$$

where the first term is the usual Dirac term. The most general Lagrangian mass term results:

$$-L_m = M\bar{\psi}\,\psi = M(\bar{\psi}_R\,\psi_L + h.c.) + \frac{M_L}{2}[\overline{(\psi_R)^c}\psi_L + h.c.] + \frac{M_R}{2}[\overline{(\psi_L)^c}\psi_R + h.c.] \tag{1.13}$$

where the first term is the Dirac term (1.9) while the second and the third are Majorana mass terms, being M_D, M_L and M_R proportional to the vacuum expectation value of ϕ, Δ_L and Δ_R respectively. Rewriting the Lagrangian in terms of two new field χ_L and χ_R:

$$\chi_L = \frac{\psi_L + \psi_L^c}{\sqrt{2}} \;\; , \;\; \chi_R = \frac{\psi_R + \psi_R^c}{\sqrt{2}} \tag{1.14}$$

arranged in a doublet $\chi = \begin{pmatrix} \chi_L \\ \chi_R \end{pmatrix}$ we obtain:

$$-L = \bar{\chi}\gamma_\mu\delta_\mu\chi + \bar{\chi}[M]\chi \tag{1.15}$$

where $[M]$ is a real symmetric matrix, called the neutrino mass matrix:

$$\begin{pmatrix} M_L & M_D \\ M_D & M_R \end{pmatrix} \tag{1.16}$$

where for various theoretical reasons $< \Delta_L >$ is usually set to zero while $< \Delta_R >$ must be very large since no effects of right-handed currents have been seen experimentally up to 549 GeV ([3]) ($< \Delta_R > \sim M_{GUT}$). The Dirac term arises form the same mechanism giving mass to the fermions, so we can say $< \phi > \sim m_f$ with f a fermion.

Diagonalizing the mass matrix $[M]$ by a rotation in the two-dimensional space of the vector χ (in practice the diagonalization is performed with a unitary matrix (U V)), we obtain the usual free Lagrangian for two particles ν and N, with masses

$$M_\nu \simeq \frac{M_D^2}{M_R} \ , \ M_N \simeq M_R \tag{1.17}$$

where the two particles ν and N are found to be two Majorana fermions $\nu^C = \nu$ and $N^C = N$ being C the charge conjugation operator. Therefore we can say we have obtained two mass eigenstates that correspond to Majorana particles, with 2 spin state each and masses of the order of meV and of M_{GUT} respectively.

1.1.2 Neutrino oscillations

A phenomenological consequence of neutrino mass is the possibility of neutrino flavor oscillations. Indeed neutrino oscillation can arise only if neutrinos are massive and mixed, or in other words, the neutrino state that is produced by electroweak interactions is not a mass eigenstate. This phenomenon was first pointed out by Pontecorvo in 1957 while the possibility of arbitrary mixing between two massive neutrino states was first introduced in 1962 by Maki, Nakagawa and Sakata. If neutrinos have masses, the weak eigenstates ν_α, produced in weak interactions are, in general, linear combinations of the mass eigenstates ν_i

$$| \ \nu_\alpha > = \sum_{i=1}^{n} U_{\alpha \ i}^* \ | \ \nu_i > \tag{1.18}$$

where n is the number of light neutrino species and U is the left part of the unitary mixing matrix used for the diagonalization of the mass matrix $[M]$ [4, 5]. In the case of three neutrino species we obtain:

$$\begin{pmatrix} \nu_e \\ \nu_\mu \\ \nu_\tau \end{pmatrix} = \begin{pmatrix} U_{e1} & U_{e2} & U_{e3} \\ U_{\mu 1} & U_{\mu 2} & U_{\mu 3} \\ U_{\tau 1} & U_{\tau 2} & U_{\tau 3} \end{pmatrix} \cdot \begin{pmatrix} \nu_1 \\ \nu_2 \\ \nu_3 \end{pmatrix} \tag{1.19}$$

After travelling a distance L (or, equivalently for relativistic neutrinos, a time t), a neutrino originally produced with flavour α evolves as follows:

$$| \ \nu_\alpha(t) > = \sum_{i=1}^{n} U_{\alpha \ i}^* \ | \ \nu_i(t) > . \tag{1.20}$$

It can be detected in the charged-current (CC) interaction $\nu_\alpha \ N' \to l_\beta \ N$ with a probability

$$P_{\alpha\beta} = |< \nu_\beta \ | \ \nu_\alpha(t) >|^2 = | \sum_{i=1}^{n} \sum_{j=1}^{n} U_{\alpha \ i}^* \ U_{\beta \ j} \ < \nu_j(0) \ | \ \nu_i(t) >|^2 \tag{1.21}$$

where E_i and m_i are respectively the energy and the mass of the neutrino mass eigenstate ν_i. In the standard approximation $| \ \nu >$ is a plane wave and its temporal evolution at a time t is

$$| \ \nu_i(t) > = e^{-iE_i t} \ | \ \nu_i(0) > . \tag{1.22}$$

Experiment	L (m)	E (MeV)	$\Delta m^2 (eV^2)$
Solar	10^{11}	1	10^{-11}
Atmospheric	$10^4 - 10^7$	$10^2 - 10^5$	$10^{-1} - 10^{-4}$
Reactor	$10^2 - 10^6$	1	$10^{-2} - 10^{-3}$
Accelerator	10^2	$10^3 - 10^4$	$\gtrsim 0.1$
Long Baseline Accelerator	$10^5 - 10^6$	10^4	$10^{-2} - 10^{-3}$

Table 1.1: *Characteristic values of L and E for various neutrino sources and experiments.*

In all cases of interest to us, the neutrinos are relativistic:

$$E_i = \sqrt{p_i^2 + m_i^2} \simeq p_i + \frac{m_i^2}{2E_i}. \tag{1.23}$$

Furthermore we can assume that $p_i \simeq p_j \equiv p \simeq E$. Then, in the case of CP conservation, we obtain the following transition probability:

$$P_{\alpha\beta} = \delta_{\alpha\beta} - 4 \sum_{i=1}^{n-1} \sum_{j=i+1}^{n} Re[U_{\alpha\,i}\,U_{\beta\,i}^*\,U_{\alpha\,j}^*\,U_{\beta\,j}] sin^2 x_{ij} \tag{1.24}$$

where in convenient units

$$x_{ij} = 1.27\,\Delta m_{ij}^2(eV^2)\,\frac{L(km)}{E(GeV)} \tag{1.25}$$

with L=t the distance between the source of ν_α and the detector (that is, the detection point of ν_β) and $\Delta m_{ij}^2 \equiv m_i^2 - m_j^2$ with $i,j = 1,2,3$ the three neutrino mass eigenstates. The transition probability (1.24) has an oscillatory behavior, with oscillation length

$$L^{osc} = \frac{4\pi E}{\Delta m_{ij}^2}. \tag{1.26}$$

and amplitude that is proportional to elements in the mixing matrix. Thus in order to have oscillations, neutrinos must have different masses ($\Delta m_{ij}^2 \neq 0$) and they must mix ($U_{\alpha i} U_{\beta i} \neq 0$), since flavor oscillation is due to interference between different mass eigenstates.

An oscillation experiment is characterized by the typical neutrino energy E and by the source-detector distance L. Source extensions (dimensions) can play also a significant role. In order to be sensitive to a given value of Δm_{ij}^2 an experiment has to be set up with $E/L \approx \Delta m_{ij}^2$ ($L \sim L^{osc}$). The typical values for the sensitivities for different types of neutrino sources are summarized in Tab. (1.1). If $(E/L) >> \Delta m_{ij}^2$ ($L << L^{osc}$), the oscillation cannot give rise to appreciable effects because $sin^2\theta_{ij} << 1$. For $(E/L) << \Delta m_{ij}^2$ ($L >> L^{osc}$), the oscillating phase goes through many cycles before detection and, since in general neutrino beams are not monochromatic, the phase is averaged to $< sin^2\theta_{ij} >= 1/2$ and the oscillation pattern is washed out.

For a two neutrino case, the mixing matrix depends on a single parameter θ:

$$U = \begin{pmatrix} cos\theta & sin\theta \\ -sin\theta & cos\theta \end{pmatrix} \tag{1.27}$$

and there is a single mass-squared difference Δm^2. Then $P_{\alpha\beta}$ of eq. (1.24) takes the well known form

$$P_{\alpha\beta} = \delta_{\alpha\beta} - (2\delta_{\alpha\beta} - 1)sin^2 2\theta sin^2 x. \tag{1.28}$$
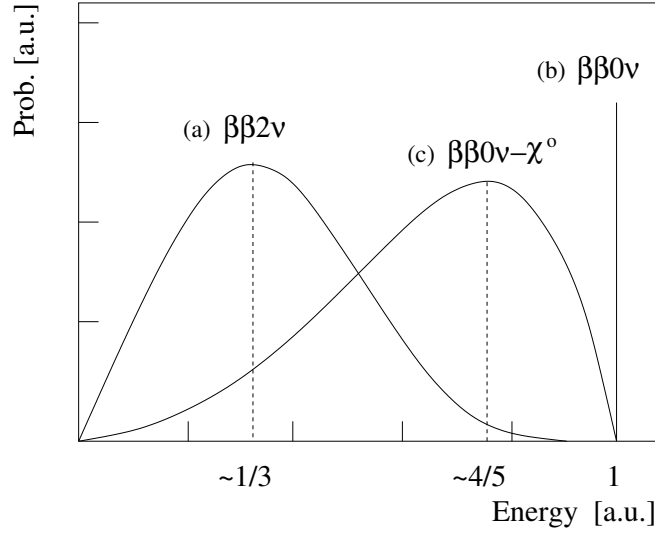
Figure 1.1: *Spectra of the sum of the electron kinetic energies for (a) DBD2ν (b) DBD0ν and (c) dBDχ.*

In a more general case CP is not conserved and the unitary mixing matrix U contains N^2 real parameters, where N is the number of different neutrino eigenstates. N of these parameters corresponds to unphysical phases, N(N-1)/2 are angles and N(N-1)/2 are physically relevant phases describing possible CP violations.

Oscillation experiments only violate the flavor lepton number but conserve the total lepton number. With such experiments one can determine, in principle, all angles and (N-1)(N-2)/2 phases. These phases, common to the Dirac and Majorana neutrinos, describe CP violation responsible for the possible differences of the oscillation probabilities $\nu_l \rightarrow \nu_{l'}$ and $\bar{\nu}_l \rightarrow \bar{\nu}_{l'}$. The remaining (N-1) phases affect only neutrino oscillation-like processes that violate the total lepton number, such as the DBD0ν decay. Such phases are physically significant only for Majorana neutrinos while for Dirac neutrinos they are unphysical. This is because for Majorana neutrinos one cannot perform the transformation $\nu_i \rightarrow \nu'_i = e^{i\alpha_i}\nu_i$, which would violate the self-coniugation property.

1.1.3 Double Beta Decay

Double Beta Decay is a rare transition between two nuclei with the same mass number A, involving the change of the nuclear charge Z by two units. The decay can proceed only if the initial nucleus is less bound than the final one. For practical reasons both must be more bound than the intermediate nucleus. These conditions are fulfilled in nature for many even-even nuclei. Typically the decay can proceed from the ground state (spin and parity always 0^+) of the initial nucleus to the ground state (also 0^+) of the final one, although the decay into excited states ($0^+ or 2^+$) is in some cases also energetically possible.

The two neutrino decay DBD2ν

$$(Z, A) \rightarrow (Z + 2, A) + e_1^- + e_2^- + \bar{\nu}_{e1} + \bar{\nu}_{e2} \tag{1.29}$$

conserves not only the electric charge but also the total lepton number and is allowed by the SM.

On the other hand the neutrinoless decay DBD0ν

$$(Z, A) \rightarrow (Z + 2, A) + e_1^- + e_2^- \tag{1.30}$$

6

violates lepton number conservation and is therefore forbidden in the standard electroweak theory.

In various extensions of the SM ([8]) a massless neutral boson χ is postulated, giving the possibility of a third decay channel via the emission of such a boson (called Majoron) (DBDχ)

$$(Z, A) \rightarrow (z + 2, A) + e_1^- + e_2^- + \chi \tag{1.31}$$

It's easy to distinguish the three decay modes (DBD2ν, DBD0ν and DBDχ) by analyzing the shape of the electron sum energy spectra, which are determined by the phase space of the outgoing light particles (see Fig. (1.1)). In the 2ν decay the maximum of the two electrons sum energy distribution is located at about 1/3 of the endpoint energy. In the 0ν mode the two electrons carry the full available kinetic energy (the nuclear recoil energy is negligible) and the spectrum is therefore a single peak at the endpoint energy. In the Majoron decay mode the electron spectrum is again continuous, but the maximum is shifted at higher energy, as required by the three body light particle phase space.

Considering only the case of left-handed V-A weak current and light massive Majorana neutrinos, the differential decay rate for the DBD0ν transition can be written as

$$d\Gamma_{0\nu} = 2\pi \sum_{spin} R_{0\nu} \delta(\epsilon_1 + \epsilon_2 + E_f - M_i) \frac{d\vec{p}_1}{(2\pi)^3} \frac{d\vec{p}_2}{(2\pi)^3} \tag{1.32}$$

whiere $\epsilon_{1(2)}$ and $\vec{p}_{1(2)}$ are the total energies and momenta of the electrons and $E_f(M_i)$ is the energy of the final nuclear state. The quantity $R_{0\nu}$ is the reaction amplitude to be evaluated in the second order perturbation theory of the weak interactions.

The leptonic part of $R_{0\nu}$, involving the emission and reabsorption of the Majorana neutrino of mass m_j is

$$-i \int \frac{d^4q}{(2\pi)^4} e^{-iq(x-y)} \bar{e}(x) \gamma_\rho P_L \frac{q^\mu \gamma_\mu + m_j}{q^2 - m_j^2} P_L \gamma_\sigma e^c(y) \tag{1.33}$$

where $P_L = (1 - \gamma_5)/2$, $\bar{e}(x), e^c(y)$ are the electron creation operators, and q is the momentum transfer four-vector. Since γ_μ matrices anticommute with γ_5 this amplitude is proportional to m_j and the term with $q^\mu \gamma_\mu$ vanishes. The effect of integrating over the energy of the virtual neutrino dq^0 and successively over the momentum $d\vec{q}$ is the appearance of a neutrino potential, very weakly depending on m_j. For the ground state to ground state transition it is enough to consider s-wave outgoing electrons, and the non-relativistic approximation for the nucleons. The nuclear part of the amplitude then turns into a sum of the Gamow-Teller and Fermi nuclear matrix elements

$$| M_{0\nu} | \equiv M_{GT}0\nu - \frac{g_V^2}{g_A^2} M_F^{0\nu} \tag{1.34}$$

where $g_V(g_A)$ are the axial vector coupling constants.

Thus, in the approximation described above, the transition amplitude for a Majorana neutrino of mass m_j is simply a product of m_j and the nuclear matrix elements (1.34). However since an electron neutrino appears at each of the two vertices, the mixing matrix elements U_{ej} are required. The physical DBD0ν reaction amplitude contains the factor U_{ej}^2 and is proportional to the factor

$$< m_\nu > = |\sum_j m_j U_{ej}^2| \tag{1.35}$$

where the sum is only over the light neutrinos with $m_j < 10 MeV$. The quantity $< m_\nu >$ is the effective neutrino mass. Since U_{ej}^2 and not $|U_{ej}|^2$ appear in $< m_\nu >$, its value depends on the Majorana phases discussed above.

In order to obtain the decay rate, the reaction amplitude has to be squared, and multiplied by the corresponding phase space integral, proportional to

$$G^{0\nu} \sim \int F(Z, \epsilon_1)F(Z, \epsilon_2)p_1 p_2 \epsilon_1 \epsilon_2 \delta(E_0 - \epsilon_1 - \epsilon_2)d\epsilon_1 d\epsilon_2 \tag{1.36}$$

where E_0 is the available energy, $F(Z, \epsilon)$ is the usual Fermi function that describes the Coulomb effect on the outgoing electron.

Summarizing, if the DBD0ν decay is mediated by the exchange of a light massive Majorana neutrino, the half life can be expressed as:

$$[T_{1/2}^{0\nu}(0^+ \to 0^+)]^{-1} = G^{0\nu}(E_0, Z) \mid M_{GT}^{0\nu} - \frac{g_V^2}{g_A^2}M_F^{0\nu} \mid^2 < m_\nu >^2 \tag{1.37}$$

where $G^{0\nu}$ is the exactly calculable phase space integral, $< m_\nu >$ is the effective neutrino mass, $M_{GT}^{0\nu}$ and $M_F^{0\nu}$ are the nuclear matrix elements defined in eq. (1.34).

Thus, if an upper limit on the DBD0ν rate is experimentally established and the nuclear matrix elements are known, it is possible to deduce the corresponding upper limit on $< m_\nu >$. On the other hand, if DBD0ν is observed it is possible to deduce the appropriate value of $< m_\nu >$.

Clearly, a reliable value (or limit) for the physical quantity $< m_\nu >$ can be inferred from experimental data only if the nuclear matrix elements governing the DBD0ν are calculated correctly, i.e. the mechanism of nuclear transitions is well understood.

There are two well established approaches for the calculation of the DBD nuclear matrix elements, namely the shell model [9] and the Quasiparticle Random Phase Approximation (QRPA) [21, 10]. The two methods differ in the size of model space and the way the ground state correlations are taken into account. A list of values of $F_N \equiv G^{0\nu} \mid M_F^{0\nu} \mid^2$ calculated in the framework of different nuclear models are summarized in Tab. (1.2). Since large F_N imply stringent constrains in $< m_\nu >$, such a parameter is usually called Nuclear Factor of Merit.

In the case of the two-neutrino double beta decay, the half-lives are customarily expressed as $[T_{1/2}^{2\nu}(0^+ \to 0^+)^{-1} = G_{2\nu} \mid M_{GT}^{2\nu} \mid^2$, where $G_{2\nu}$ is an integrated kinematical factor [27] and $M_{GT}^{2\nu}$ the nuclear $\beta\beta$ Gamow Teller matrix element.

In the framework discussed above where the weak eigenstate neutrinos can be expressed as superpositions of the mass eigenstates neutrinos using the mixing matrix U_{li}, the electron neutrino is then the superposition

$$\nu_e = \sum_i^N U_{ei}\nu_i \tag{1.38}$$

and the effective neutrino mass takes the form of eq. (1.35) and more explicitly:

$$\mid < m_\nu > \mid \equiv \mid\mid U_{e1} \mid^2 m_1 + \mid U_{e2} \mid^2 m_2 e^{i\phi_2} + \mid U_{e3} \mid^2 m_3 e^{i\phi_3} \mid \tag{1.39}$$

where where $e^{i\phi_2}$ and $e^{i\phi_3}$ are the Majorana CP phases (± 1 for CP conservation) and $m_{1,2,3}$ are the mass eigenvalues and the elements $\mid U_{ei}^2 \mid$ are given by

$$\mid U_{e1}^2 \mid = cos^2\theta_{13}cos^2\theta_{12}, \quad \mid U_{e2}^2 \mid = cos^2\theta_{13}sin^2\theta_{12}, \quad \mid U_{e3}^2 \mid = sin^2\theta_{13} \tag{1.40}$$

Neutrino oscillation data are compatible with two types of neutrino mass spectra, as illustrated in Fig. (1.2)

1. *Normal Hierarchy* (NH) $m_1 < m_2 << m_3$

	Authors/Ref.	Method	$T_{1/2}(^{130}\text{Te})$ $(10^{23}\,\text{y})$	$F_N(^{130}\text{Te})$ $(10^{-13}\,\text{y}^{-1})$	$F_N(^{76}\text{Ge})$ $(10^{-13}\,\text{y}^{-1})$
QRPA	Staudt et al., 1992 [11]	pairing (Paris)	0.77-0.88	29-34	5.9-10
		pairing (Bonn)	0.9-1.1	24-29	4.5-8.9
	Pantis et al., 1996 [12]	no p-n pairing	8.64	3.0	0.73
		p-n pairing	21.1	1.24	0.14
	Vogel, 1986 [13]		6.6	3.96	0.19
	Civitarese, 1987 [14]		5.2	5.0	1.2
	Tomoda, 1991 [15]		5.2	5.03	1.2
	Barbero et al., 1999 [16]		3.36	7.77	0.84
	Simkovic, 1999 [17]	pn-RQRPA	14.5	1.79	0.62
	Suhonen et al., 1992 [18]		8.34	3.13	0.72
	Muto et al., 1989 [19]		4.89	5.34	1.1
	Stoica et al., 2001 [20]	large basis	10.7	2.44	0.65
		short basis	9.83	2.66	0.9
	Faessler et al., 1998 [21]		9.4	2.78	0.83
	Engel et al., 1989 [22]	generalized seniority	2.4	10.9	1.14
	Aunola et al., 1998 [23]	WS	4.56	5.72	0.9
		AWS	5.16	5.06	1.33
	Rodin et al., 2003 [24]		27.5	0.95	0.45
SM	Haxton et al., 1984 [25]	weak coupling	1.6	16.3	1.54
	Caurier et al., 1996 [9]	large basis	58	0.45	0.15
OEM	Hirsh et al., 1995 [26]		7.3	3.6	0.95

Table 1.2: $\beta\beta(0\nu)$ nuclear factors of merit F_N for ^{130}Te and ^{76}Ge according to different evaluation methods (QRPA: Quasi Random Phase Approximation, SM: Shell Model and OEM: Operator Expansion Method) and authors. The foreseen $\beta\beta(0\nu)$ half-lifetime for ^{130}Te ($|\langle m_\nu \rangle|$ =1 eV) is also reported.

$$\Delta m_{21}^2 \simeq \Delta m_{sol}^2; \quad \Delta m_{32}^2 \simeq \Delta m_{atm}^2$$

2. *Inverted Hierarchy* (IH) $m_3 << m_1 < m_2$

$$\Delta m_{21}^2 \simeq \Delta m_{sol}^2; \quad \Delta m_{32}^2 \simeq -\Delta m_{atm}^2$$

In all acases we lack any information about the absolute scale of the ν masses, i.e. the actual value of m_1.

For neutrino masses in the case of NH we have

$$m_2 \sim \sqrt{m_1^2 + \Delta m_{sol}^2}, \quad m_3 \sim \sqrt{m_1^2 + \Delta m_{atm}^2} \tag{1.41}$$

where we took into account the results from oscillation experiments $\Delta m_{sol}^2 << \Delta m_{atm}^2$. In the case of inverted spectrum we have

$$m_2 \simeq m_1 \simeq \sqrt{m_3^2 + \Delta m_{atm}^2}, \tag{1.42}$$

There is also a third possibility, called the Quasi Degenerate Hierarchy (QDH), in which the lightest neutrino mass is much larger than $\sqrt{\Delta m_{atm}^2}$. In this case we have $m_1 \simeq m_2 \simeq m_3$.

The values of $< m_\nu >$ depends on the neutrino mass spectrum [29]-[37].
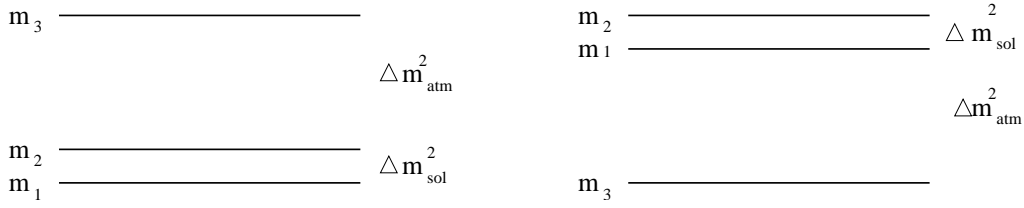
Figure 1.2: *Normal and inverted mass hierarchies schemes. Quasi-degenerate hierarchy corresponds to the case $m_1 >> \delta m_A T >> \delta m_S$.*

1. *Normal Hierarchy*

   In this case neutrino masses are known from neutrino oscillation data. We have

   $$m_1 << \sqrt{\Delta m_{sol}^2}, \quad m_2 \simeq \sqrt{\Delta m_{sol}^2}, \quad m_3 \simeq \sqrt{\Delta m_{atm}^2} \tag{1.43}$$

   The effective Majorana mass in this cases can be expressed as

   $$< m_\nu > \simeq | \cos^2\theta_{13}(\Delta m_{sol}^2 e^{2i\phi_2} \sin^2\theta_{sol}) + \sqrt{\Delta m_{atm}^2} e^{2i\phi_3} \sin^2\theta_{13}\sqrt{\Delta m_{atm}^2}) | \tag{1.44}$$

   From this expression we can also derive an upper and a lower bound for $< m_\nu >$:

   $$< m_\nu > \leq (\cos^2\theta_{13}\sin^2\theta_{sol}\sqrt{\Delta m_{sol}^2} + \sin^2\theta_{13}\sqrt{\Delta m_{atm}^2}) \tag{1.45}$$

   and

   $$< m_\nu > \geq | \cos^2\theta_{13}\sin^2\theta_{sol}\sqrt{\Delta m_{sol}^2} - \sin^2\theta_{13} | \tag{1.46}$$

2. *Inverted Hierarchy*

   In this case for neutrino masses we have

   $$m_3 << \sqrt{\Delta m_{atm}^2}, \quad m_1 \simeq \sqrt{\Delta m_{atm}^2},$$
   $$m_2 \simeq \sqrt{\Delta m_{atm}^2}(1 + \frac{\Delta m_{sol}^2}{2\Delta m_{atm}^2}) \simeq \sqrt{\Delta m_{atm}^2} \tag{1.47}$$

   The effective Majorana mass is given by

   $$< m_\nu > \simeq \sqrt{\Delta m_{atm}^2} | \sum_{i=1,2} U_{ei}^2 | \tag{1.48}$$

   Neglecting small ($< 5\%$) correction due to $| U_{e3} |^2$, for $< m_\nu >$ we obtain

   $$< m_\nu > \simeq \sqrt{\Delta m_{atm}^2} | \cos^2\theta_{13}(\cos^2\theta sol + e^{2i\phi_2}\sin^2\theta_{sol}) | \tag{1.49}$$

   where $\phi_{21} = \phi_2 - \phi_1$ is a Majorana CP-phase difference.

   Thus, in the case of HI the value of the $< m_\nu >$ can lay in the range (in the case of CP conservation)

   $$\cos2\theta_{sol}\sqrt{\Delta m_{atm}^2} \leq < m_\nu > \leq \sqrt{\Delta m_{atm}^2} \tag{1.50}$$
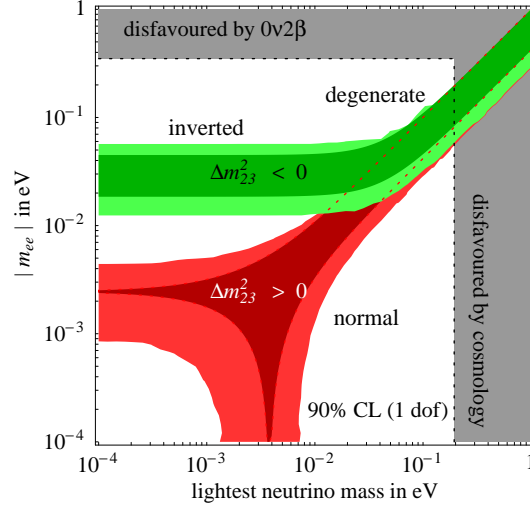
Figure 1.3: *The effective Majorana mass $\langle m_{ee} \rangle$ as a function of the lightest neutrino mass [31].*

3. *Quasi Degenerated Hierarchy*

   In this case the effective neutrino Majorana mass takes the form

$$< m_\nu > \simeq m_1 \mid \sum_{i=1}^{3} U_{ei}^2 \mid \tag{1.51}$$

By neglecting the small contributions of the parameter $\mid U_{e3} \mid^2$ we obtain

$$< m_\nu > \simeq m_1 \mid cos^2\theta_{13}(cos^2\theta sol + e^{2i\phi_2}sin^2\theta_{sol}) \mid \tag{1.52}$$

thus in the case of Quasi Degenerate Hierarchy the value of $< m_\nu >$ can lay in the range:

$$cos2\theta_{sol}m_1 \leq < m_\nu > \leq m_1 \tag{1.53}$$

From equations (1.45), (1.46), (1.50), (1.53) we can see that unless $< m_\nu >$ depends on the unknown phases α_i, the upper and lower limits for $< m_\nu >$ depend only on the absolute value of the mixing angles. Thus, if the search for DBD0ν is successful and the value of $< m_\nu >$ is determined, and at the same time the mixing angles $\mid U_{ei}^2 \mid$ and the mass square differences Δm_{ij}^2 are known from oscillation experiments, a range of absolute values of the neutrino masses can be deduced (see Fig. 1.3)[39]).

Naturally, if another constraint exists, for example a successful determination of the neutrino mass square $\sum_i \mid U_{ei}^2 \mid m_i^2$ in Beta Decay experiments, one can use the knowledge of $< m_\nu >$ to determine or constrain the phases α_i.

From equations (1.44) and (1.49) it is also possible to constrain the Majorana neutrino contribution to the cosmic microwave fluctuations $\Sigma \equiv \Sigma_j m_j$ [38]

$$2|\langle m_\nu \rangle| + \sqrt{|\langle m_\nu \rangle|^2 \pm \delta m_{AT}^2} \leq \Sigma \leq \frac{2|\langle m_\nu \rangle| + \sqrt{|\langle m_\nu \rangle|^2 \pm \delta m_{AT}^2 cos^2(2\theta_3)}}{|cos(2\theta_3)|} \tag{1.54}$$

where the plus sign is for NH and the minus sign is for IH. In the case $\delta m_{atm}^2 << \Sigma^2$ eq. (1.54) can be simplified

$$|\langle m_\nu \rangle| \leq \frac{\Sigma}{3} \leq 2|\langle m_\nu \rangle| \tag{1.55}$$

11

1.2 Different technical approaches to DBD0ν research

In order to measure double beta decays, three general approaches have been devised: geochemical, radiochemical, and direct counting measurements. In the geochemical experiments [42], isotopic anomalies in daughters concentrations of $\beta\beta$ decaying nuclei over geological time scales are investigated. They are inclusive $2\nu + 0\nu$ measurements, not distinguishing 2ν from 0ν modes. However, when $T_{1/2,exp.meas.}^{2\nu+0\nu(geoch.)} \ll T_{1/2,exp.bound}^{0\nu(direct)}$, most of the decay is through 2ν mode. The finite half-lives measured geochemically in the cases of ^{82}Se, ^{96}Zr, ^{128,130}Te, ^{238}U can be regarded as DBD2ν half-life values and at the same time as a bound for $T_{1/2}^{0\nu}$, since $T_{1/2}^{0\nu}$ cannot be shorter than $T_{1/2,geoch.}$.

Another way to search for double beta decay is through radiochemical experiments, by noticing that when the daughter nuclei of a double beta emitter are themselves radioactive, they can be accumulated, extracted and counted. If the daughter has a half-life much smaller than 10^9y and has no other long-lived parents, its presence can be only due to $\beta\beta$. Noticeable examples are that of $^{238}U \rightarrow {}^{238}Pu$ (88 y, α decay) and $^{244}Pu \rightarrow {}^{244}Cm$ (18 y, α decay) [46]. Also this technique measures the time for inclusive decays and therefore is not able to distinguish the different Double Beta Decay channels.

Most of the recent activity, however, refers to direct counting experiments, which measure the energy of the $\beta\beta$ emitted electrons and so the spectral shapes of the 2ν, 0ν, and $0\nu\chi$ modes of double beta decay. In spite of such characteristic imprints (a peak at the Q-value for DBD0ν and a continuum in the 2ν and $0\nu\chi$ case), the rarity of the processes under consideration makes their identification very difficult. In fact, double beta decays are very rare phenomena, with two-neutrino half-lives as large as 10^{18} y to 10^{25} y and with neutrinoless half-lives as long as 10^{25} y (and beyond), as the best lower limit stands by now. Such remotely probable signals have to be disentangled from a background due to natural radioactive decay chains, cosmogenic-induced activity, and man-made radioactivity, which deposit energy on the same region where the DBD decays do but at a faster rate. Consequently, the main task in DBD searches is to reduce the background by using the state-of-the-art ultra-low background techniques and, hopefully, identifying the signal. Some experimental devices track also the electrons (and other charged particles), measuring the energy, angular distribution, and topology of events. The tracking capabilities are useful to discriminate the DBD signal from the background.

The types of detectors currently used are:

- *Calorimeters:* the detector acts also as the DBD source [47]. Examples of calorimeters are Ge diodes, scintillators – CaF$_2$, CdWO$_4$ –, thermal detectors –TeO$_2$ –, Xe ionization chambers. These experiments measure the two-electron sum energy and partially discriminate background signal by pulse shape analysis (PSD). Notable examples are IGEX, Heidelberg-Moscow, Milano-Gran Sasso (MiDBD), CUORICINO and the proposed CUORE and Majorana.

- *Tracking detectors:* in the inhomogeneous (source$\neq$detector) type (Time Projection Chambers TPC, drift chambers, electronic detectors) the DBD source plane(s) is placed within the detector tracking volume, defining two –or more– detector sectors. Leading examples of tracking devices are the Irvine TPC's and the NEMO and ELEGANTS series.

- *Tracking calorimeters:* they are tracking devices where the tracking volume is also the DBD source, for example a Xenon TPC (CALTECH/PSI/Neuchatel) and the future EXO.

Well-known examples of DBD emitters measured in direct counting experiments are ^{48}Ca, ^{76}Ge, ^{96}Zr, ^{82}Se, ^{100}Mo, ^{116}Cd, ^{130}Te, ^{136}Xe, ^{150}Nd. Their phase space factor for the 2ν and 0ν decay modes are reported in Tab. (1.3). The strategies followed in the DBD searches are different.

Isotopo	$G_{2\nu}$	$G_{0\nu}$
^{76}Ge	$1.31 \cdot 10^{-19}$	$6.40 \cdot 10^{-15}$
^{82}Se	$4.35 \cdot 10^{-18}$	$2.82 \cdot 10^{-14}$
^{100}Mo	$9.43 \cdot 10^{-18}$	$4.58 \cdot 10^{-14}$
^{116}Cd	$8.00 \cdot 10^{-18}$	$4.95 \cdot 10^{-14}$
^{128}Te	$8.54 \cdot 10^{-22}$	$1.83 \cdot 10^{-15}$
^{130}Te	$4.80 \cdot 10^{-18}$	$4.44 \cdot 10^{-14}$
^{136}Xe	$4.86 \cdot 10^{-18}$	$4.73 \cdot 10^{-14}$
^{150}Nd	$1.19 \cdot 10^{-16}$	$2.10 \cdot 10^{-13}$
^{238}U	$6.80 \cdot 10^{-19}$	$1.55 \cdot 10^{-13}$
^{78}Kr$(\beta^+\beta^+)$	$3.90 \cdot 10^{-25}$	$1.45 \cdot 10^{-18}$

Table 1.3: *Phase space factor for some good candidates for $\beta\beta 2\nu$ and $\beta\beta 0\nu$*

Calorimeters of good energy resolution and almost 100% efficiency (e.g. Ge-detectors and tellurite bolometers) are well suited for $\beta\beta(0\nu)$ searches. They lack, obviously, the tracking capabilities to identify the background on an event-by-event basis but they have, in favour, that their sharp energy resolutions do not allow the leakage of too many counts from ordinary DBD2ν into the neutrinoless region. The identification capabilities of the various types of chambers make them well suited for DBD searches, but, on the other hand, their energy resolution is rather poor and the detection efficiency is only of a few percent. Furthermore, the ultimate irreducible background source in these devices when looking for $\beta\beta(0\nu)$ decay will be the standard DBD2ν decay contribution. The rejection of background provided by the tracking compensates, nevertheless, the figure of merit in $\beta\beta(0\nu)$ searches.

Modular calorimeters can have reasonable amounts of $\beta\beta$ emitters (Heidelberg/Moscow, IGEX, MiDBD and CUORICINO experiments) or large quantities (like CUORE, Majorana and GENIUS). Tracking detectors, instead, cannot accommodate large amounts of $\beta\beta$ emitters in the source plate. Recent versions of tracking devices have 10 kg and more (NEMO3). On the other hand, TPC devices are planning to reach one ton and more of Xenon (EXO).

The general strategy followed to perform a neutrinoless double beta decay experiment is simply dictated by a simple parameterization of expression of the half-life

$$T_{1/2}^{0\nu} \simeq ln2 \times \frac{N \cdot t}{S} \tag{1.56}$$

where N is the number of $\beta\beta$ emitter nuclei and S the number of recorded counts during time t (or the upper limit of double beta counts consistent with the observed background). When taking for S the maximum signal which could be hidden by background fluctuations one has the so-called detector *neutrinoless sensitivity* which for homogeneous (source=detector) devices, for which the background rate scales with the detector mass, reads

$$F_D = 4.17 \times 10^{26}(f/A)(Mt/B\Gamma)^{1/2}\varepsilon_\Gamma \text{ years} \tag{1.57}$$

where B is the background rate (c/(keV kg y)), M the mass of $\beta\beta$ emitter (kg), ε_Γ the detector efficiency in the energy interval Γ around Q$_{\beta\beta}$ (Γ = FWHM), t the running time measurement in years, f the isotopic abundance and A the mass number. According to eq. (1.57) we see that in order to obtain a powerful DBD0ν experiment it's necessary

- to work with a very large mass source;

- to have good energy resolution and high efficiency detectors;

- to suppress the background contribution performing the experiment in a low activity environment and eventually using event topology reconstruction;

- to have long measurements;

- to choose a nucleus with high isotopic abundance.

In addiction, as in DBD0ν experiments the searched parameter is the effective neutrino mass $< m_\nu >$, it is of fundamental importance to choose a nucleus with high nuclear factor of merit F_N.

1.3 Existing $0\nu\beta\beta$-decay data and future experiments

Neutrinoless double β decay, for practical reasons, is searched for in nuclei for which usual β decay is forbidden by the conservation of energy. There are several even-even nuclei of this type:

$$
\begin{aligned}
&^{76}\text{Ge}(Q = 2.039\text{MeV}), \quad ^{130}\text{Te}(Q = 2.528\text{MeV}), \quad ^{136}\text{Xe}(Q = 2.480\text{MeV}), \\
&^{100}\text{Mo}(Q = 3.034\text{MeV}), \quad ^{150}\text{Nd}(Q = 3.367\text{MeV}), \quad ^{150}\text{Nd}(Q = 3.367\text{MeV})
\end{aligned} \tag{1.58}
$$

and others. The Q-value of the transition, reported in the brackets, is a relevant parameter for DBD0ν of the $0\nu\beta\beta$-decay: the decay probability depends on Q and background contributions are generally lower at higher energies. Isotopes with large Q values ate therefore preferred.

Emitter	Experiment	$T^{0\nu}_{1/2} >$	C.L.%
^{48}Ca	ELEGANT VI	1.4×10^{22} y	90
^{76}Ge	MPIH/KIAE	1.9×10^{25} y	90
	IGEX	1.6×10^{25} y	90
^{82}Se	UCI	2.7×10^{22} y	68
	NEMO 3	4.7×10^{22} y	90
^{96}Zr	NEMO 2	1.3×10^{21} y	90
^{100}Mo	LBL/MHC/UNM	2.2×10^{22} y	68
	UCI	2.6×10^{21} y	90
	Osaka	5.5×10^{22} y	90
	NEMO 3	6×10^{22} y	90
^{116}Cd	Kiev	1.7×10^{23} y	90
	Osaka	2.9×10^{21} y	90
	NEMO 3	1.6×10^{22} y	90
^{130}Te	Milano	2.1×10^{23} y	90
	CUORICINO	1×10^{24} y	90
^{136}Xe	Caltech/UN/PSI	4.4×10^{23} y	90
^{136}Xe	Rome	1.2×10^{24} y	90
^{150}Nd	UCI	1.2×10^{21} y	90
	NEMO 3	1.4×10^{21} y	90

Table 1.4: *Limits on Neutrinoless Decay Modes*

The results of the main experiments on the search for DBD0ν are summarized in Tab. (1.4) and (1.5) . The most stringent upper bounds on the $< m_\nu >$ have been reached in Ge (IGEX

Experiment	$|\langle m_\nu \rangle| <$ (eV)
IGEX enrich. ^{76}Ge	$(0.33 \sim 1.35)$ (6.0kg)
H/M enrich. ^{76}Ge	$(0.35 \sim 1.05)$ (11kg)
CUORICINO nat. ^{130}Te	$(0.26 \sim 1.45)$ (40.7kg)
MiDBD nat. ^{130}Te	$(0.38 \sim 2.2)$ (6.8kg)

Table 1.5: *Current best constraints (upper limits) on* $|\langle m_\nu \rangle|$.

and Heidelberg-Moscow [40]) and CUORICINO [41] experiments. The detector (and source) of the Heidelberg-Moscow experiment [40] consists of 5 crystals of 86% enreached ^{76}Ge with a total active mass of about 11kg. The experiment operated in the Gran Sasso underground laboratory, under heavy shields for gamma and neutrono envronmental radioactivity. Extremely low background levels were achieved thanks to a careful selection of the setup materials and further improved by the use of Pulse Shape Discrimination (PSD) techniques, based on the identification of single site events. After the PSD cuts, in the DBD0ν region the background level is $\sim 0.06 \pm 0.02$ c/keV/kg/y. For the half-life the lower bound

$$T_{1/2}^{0\nu} \geq 1.9 \cdot 10^{25} \, y \quad (90\% \, \text{CL}) \tag{1.59}$$

has been found. Taking into account different calculations of the nuclear matrix element, from eq. (1.59) for the effective Majorana mass $< m_\nu >$ the following upper bounds

$$< m_\nu > \leq (0.3 - 1.2) \, \text{eV} \, . \tag{1.60}$$

were obtained. Part of the Heidelberg Moscow group claimed an evidence for the DBD0ν in 2001 [66] with a best fit for the neutrino Majorana mass at $< m_\nu >= 0.39$ eV. More recently a new article with added statistics was published [48]. The new analysis confirms the first claimed result giving a range for $< m_\nu >$ between 0.2 and 0.6 eV (99.73% C.L.) with the best value at 0.4 eV.

Possible confirmations of this result by other experiments would imply a degenerate neutrino spectrum. Because of the large uncertainties in the neutrino matrix elements it will be of fundamental importance to perform the research for DBD0ν for different isotopes.

A running experiment that will be able to test the HM result in a few years on a different isotope is CUORICINO. In the cryogenic experiment CUORICINO [41] TeO_2 crystals with a total mass 40.7 kg are employed. Details of this experiment will be reported later. For the half-life of ^{130}Te in this experiment the following lower bound

$$T_{1/2}^{0\nu} \geq 1 \cdot 10^{24} \, \text{years} \tag{1.61}$$

was reached recently. From eq. (1.61) for the effective Majorana mass the upper bounds

$$< m_\nu > \leq (0.26 - 1.45) \, \text{eV} \tag{1.62}$$

were obtained.

Many projects of new experiments on the search for the neutrinoless double β-decay of different nuclei are under research and development at present (see [43, 44, 45]).

The main goal of the future experiments is to reach a sensitivity on $< m_\nu >$ of the order of a few 10^{-2}eV or better. This goal can be accomplished by detectors with mass about 1 ton or more, which have a good energy resolution, low background and an efficient signature for $0\nu\beta\beta$ events (see eq. (1.57)).

The experiment CUORE [41] will be a continuation of the CUORICINO experiment. Cryogenic detector will consist of 988 Te O_2 crystals operated at a temperature 10 mK. The total mass of the detector will be about 750 kg. The expected resolution at $E_0 = 2.528$ MeV is 5 keV. For the half-life of ^{130}Te the value

$$T_{1/2}^{0\nu} \simeq 2.96 \cdot 10^{26} \text{ years} \qquad (1.63)$$

at 68% CL in 1 year is envisaged. This corresponds to the sensitivity

$$< m_\nu > \simeq (20 - 110) \text{ meV} \qquad (1.64)$$

In the EXO experiment [44] up to 10 tons of 60-80 % isotopically enriched ^{136}Xe are planned to be used. An important feature of this experiment is a laser tagging of Ba^+ ions, produced in the recombination of Ba^{++} ions from the decay ^{136}Xe $\rightarrow^{136}$ $Ba^{++} + e^- + e^-$. The detection of Ba^+ ions will provide large background reduction. The value

$$T_{1/2}^{0\nu} \simeq 1 \cdot 10^{28} \text{ years} \qquad (1.65)$$

is expected after improving the energy resolution and with an effective Ba^+ tagging. It corresponds to the sensitivity

$$< m_\nu > \simeq (1.3 - 3.7) \cdot 10^{-2} \text{ eV} \qquad (1.66)$$

The GENIUS experiment [48] will be a development of the Heidelberg-Moscow experiment. About 1 ton of 86 % enriched ^{76}Ge will be embedded in a large liquid nitrogen cryostat . The liquid nitrogen will provide effective shielding from the external background. For the half-life a value

$$T_{1/2}^{0\nu} \simeq 1 \cdot 10^{28} \text{ years} \qquad (1.67)$$

is expected upon the background reduction to a $6 \cdot 10^{-3}$ c/keV/kg/y in the DBD region. This value for the half-life corresponds to the sensitivity

$$< m_\nu > \simeq (1.3 - 5.0) \cdot 10^{-2} \text{ eV} \qquad (1.68)$$

In the MAJORANA experiment [45], which will be the continuation of the IGEX experiment [49], about 500 kg of 86 % enreached ^{76}Ge will be used. The main background is expected from the decay ^{68}Ge $\rightarrow^{68}$ Ga $+ e^+ + \nu_e$. It will be suppressed by the segmentation of the detector and effective pulse shape analysis of the signal. In the MAJORANA experiment the value

$$T_{1/2}^{0\nu} \simeq 4 \cdot 10^{27} \text{ years} \qquad (1.69)$$

is expected. It corresponds to the sensitivity

$$< m_\nu > \simeq (2.1 - 7.0) \cdot 10^{-2} \text{ eV}. \qquad (1.70)$$

1.4   Neutrino data

The status of the problem of neutrino mixing changed drastically during the last years: in the atmospheric neutrino Super-Kamiokande (SK) [50], solar neutrino SNO [51, 52] and reactor antineutrino KamLAND [53] experiments *model independent evidences of neutrino oscillations* were obtained. All neutrino oscillation data, except the data of the accelerator LSND experiment [54], can be coherently described in the framework if we assume the existence of three-neutrino mixing in vacuum as reported in eq. (1.18). The SK atmospheric neutrino data are best described in terms of two-neutrino

$\nu_\mu \to \nu_\tau$ oscillations. From the analysis of the experimental data the following best-fit values of the oscillation parameters were found [50]:

$$|\Delta m_{32}^2| = 2 \cdot 10^{-3} \mathrm{eV}^2, \quad \sin^2 2\theta_{23} = 1.0 \quad (\chi^2_{\min} = 170.8/170 \,\mathrm{d.o.f.}). \tag{1.71}$$

At the 90% C.L. one has:

$$1.3 \cdot 10^{-3} \leq |\Delta m_{32}^2| \leq 3.0 \cdot 10^{-3} \mathrm{eV}^2, \quad \sin^2 2\theta_{23} > 0.9. \tag{1.72}$$

The results of all solar neutrino experiments can be explained by $coherent \nu_e \to \nu_{\mu,\tau}$ transitions in matter (MSW effect). In the KamLAND experiment, $\bar{\nu}_e$ disappearance due to transitions $\bar{\nu}_e \to \bar{\nu}_{\mu,\tau}$ in vacuum was observed. From a global two-neutrino oscillation analysis of the solar and KamLAND data (performed under the assumption of CPT-invariance), the following best-fit values of the relevant oscillation parameters were obtained [52]:

$$\Delta m_{21}^2 = 7.1 \cdot 10^{-5} \mathrm{eV}^2, \quad \sin^2 \theta_{12} = 0.29. \tag{1.73}$$

In a similar 3-neutrino oscillation analysis of the solar neutrino, KamLAND and CHOOZ [55] data,performed in [56], it was found that at 90% C.L. one has:

$$\begin{array}{ll} 5.6 \cdot 10^{-5} \leq \Delta m_{21}^2 \leq 9.2 \cdot 10^{-5} \mathrm{eV}^2, \quad 0.23 \leq \sin^2 \theta_{12} \leq 0.38, \quad \text{for} \quad \sin^2 \theta_{13} = 0.0, \\ 6.1 \cdot 10^{-5} \leq \Delta m_{21}^2 \leq 8.5 \cdot 10^{-5} \mathrm{eV}^2, \quad 0.25 \leq \sin^2 \theta_{12} \leq 0.36, \quad \text{for} \quad \sin^2 \theta_{13} = 0.04, \end{array} \tag{1.74}$$

where θ_{13} is the mixing angle limited by the reactor CHOOZ and Palo Verde experiments [55, 57]. The negative results of the CHOOZ [55] and Palo Verde [57] experiments are very important for understanding the pattern of neutrino mixing and oscillations. In these experiments no disappearance of $\bar{\nu}_e$ was observed. From the 90% C.L. exclusion curve obtained from the analysis of the data of the CHOOZ experiment, the following bound can be derived

$$\sin^2 \theta_{13} < 5 \cdot 10^{-2} \tag{1.75}$$

The same result holds when a global 3-neutrino oscillation analysis of the solar, KamLAND and CHOOZ data with $|\Delta m_{32}^2|$ taken to lie in the interval eq. (1.72) is considered [56].

For what concerns the mass of the lightest neutrino mass eigenstate ν_1 (ν_3) we have only an upper bound. From the data of the tritium Mainz [58] and Troitsk [59] experiments it was found

$$m_1 \leq 2.2 \ \mathrm{eV} \tag{1.76}$$

In the future tritium experiment KATRIN [60] a sensitivity of $m_1 \simeq 0.25 \,\mathrm{eV}$ is expected.

An important information about the sum of the neutrino masses can be obtained from cosmological data. From the Wilkinson Microwave Anisotropy Probe (WMAP) and the 2 degree Field Galaxy Redshift Survey (2dFGRS) data it was found [61]

$$\sum_i m_i \leq 0.7 \ \mathrm{eV}. \tag{1.77}$$

A more conservative bound was obtained in [62] from the analysis of the latest Sloan Digital Sky Survey data and WMAP data. The best-fit value of $\sum_i m_i$ was found to be equal to zero. For the upper bound one obtains

$$\sum_i m_i \leq 1.7 \ \mathrm{eV}. \tag{1.78}$$

For the case of three massive neutrinos this bound implies

$$m_1 \leq 0.6 \text{ eV}. \tag{1.79}$$

Using the neutrino oscillation data one can predict the possible ranges of values of the effective Majorana mass. The prediction depends strongly on the character of the neutrino mass spectrum and on the value of the lightest neutrino mass (see [29]-[37]). It is possible to summarize the main results for the three possible types of neutrino mass spectrum as follows [63, 64].

1. *Normal hierarchy*:
   Using the 90% C.L. ranges (1.72) and (1.74) of the oscillation parameters and the CHOOZ bound (1.75) and from eq. (1.45), for the effective Majorana mass one finds [63, 30, 65]

$$< m_\nu > \lesssim 5.5 \cdot 10^{-3} \text{ eV} \tag{1.80}$$

   This bound is significantly smaller than the expected sensitivity of the future DBD0ν experiments. The observation of the DBD0ν in the next generation of experiments might exclude normal hierarchical neutrino mass spectrum.

2. *Inverted hierarchy*:
   From eq. (1.50) and using the 90% C.L. allowed values of the parameters (see eq. (1.72) and (1.74)) for the effective Majorana mass one finds [30, 65]:

$$10^{-2} \text{ eV} \lesssim < m_\nu > \lesssim 5.5 \cdot 10^{-2} \text{ eV} \tag{1.81}$$

   where the upper and lower bounds of eq. (1.50) correspond to the case of CP conservation and equal and opposite CP-parities for the neutrinos ν_1 and ν_2 respectively. Thus, if the neutrino mass spectrum is of the inverted hierarchical type and the massive neutrinos are Majorana particles, DBD0ν can be observed in the experiments of next generation.

   Assuming that the problem of nuclear matrix elements will be solved, we see that if the measured value of $< m_\nu >$ will be within the range given in eq. (1.50), it will be an indication in favor of inverted hierarchy of neutrino masses. The only unknown parameter, which enter into expression for the effective Majorana mass in the case of inverted hierarchy, is $\sin^2 \alpha$. Thus, the measurement of $< m_\nu >$ might allow, in principle, to obtain an information about Majorana CP phase difference α [29, 30]. It would require, however, a precise measurement of the DBD0ν half-time.

3. *Quasi degenerate hierarchy*
   Using the best fit value (1.73) we obtain

$$0.42 \ m_1 \leq |m_{\beta\beta}| \leq m_1. \tag{1.82}$$

   where m_1 is the mass eigenstate almost equal for all the eigenstates in the QDH scheme. Thus, a relatively large effective Majorana mass $|m_{\beta\beta}|$ (much larger than $\sqrt{\Delta m_{\text{atm}}^2} \simeq 4.5 \cdot 10^{-2}\text{eV}$) means that the neutrino mass spectrum is quasi degenerate. If $|m_{\beta\beta}| \gg \sqrt{\Delta m_{\text{atm}}^2} \simeq 4.5 \cdot 10^{-2}\text{eV}$ will be confirmed by other DBD0ν experiments, the explanation could be a degenerate neutrino mass spectrum. From (1.82) for m_1 we get the range

$$|m_{\beta\beta}| \leq m_1 \leq 2.38 \ |m_{\beta\beta}| \tag{1.83}$$

   From (1.52) it is obvious that if the common mass m_1 will be determined from β-decay measurements and/or cosmological data, nevertheless the evidence of the DBD0ν will allow to deduce a valuable information about Majorana CP phase difference via the accurate measurement of the $0\nu\beta\beta$ half-time.

Finally, by taking into account existing values of neutrino oscillation parameters we can take some general conclusions:

- If the DBD0ν will be not observed in the experiments of the next generation and

$$< m_\nu > \leq \quad \text{a few} \ 10^{-2} \ \text{eV},$$

  either massive neutrinos are Dirac particles or massive neutrinos are Majorana particles and normal neutrino mass hierarchy is realized in nature. The observation of the DBD0ν with

$$< m_\nu > \geq \ 4.5 \ 10^{-2} \ \text{eV}$$

  will exclude normal hierarchy of neutrino masses.

- If the DBD0ν will be observed and

$$0.42 \ \sqrt{\Delta m_{\text{atm}}^2} \ \leq \ < m_\nu > \ \leq \ \sqrt{\Delta m_{\text{atm}}^2},$$

  it will be an indication in favor of the inverted hierarchy of neutrino masses.

- If the DBD0ν will be observed in future experiments and

$$< m_\nu > \gg \ \sqrt{\Delta m_{\text{atm}}^2},$$

  the neutrino mass spectrum is quasi degenerate and a range for the common neutrino mass can be determined.

- If from the future tritium neutrino experiments or from future cosmological measurements the common neutrino mass will be determined, it will be possible to predict the value of effective Majorana neutrino mass:

$$0.42 \ m_1 \leq |m_{\beta\beta}| \leq m_1.$$

  A non-observation of the DBD0ν with effective Majorana mass $< m_\nu >$ in this range will mean that neutrinos are Dirac particles (or other mechanisms of the violation of the lepton number are involved).

Chapter 2

Low temperature detectors

Introduction

Conventional techniques for energy deposition measurements are based on the detection of the energy released in the form of ionization and excitation of the detector's atoms. Unfortunately the amount of energy lost in channels different from the detected ones is quite large. In particular, most of the energy is converted in phonon excitations of the lattice volume of the detector. This loss of energy, together with the high energy value necessary for an atom excitation or ionization (the elementary detected event), increase the statistical fluctuations of the number of elementary excitations, thus worsening the intrinsic energy resolution of such detecting techniques.

Thermal detectors on the other hand measure the portion of the deposited energy converted in phonons, through the corresponding temperature rise. As it will be shown later this guarantees a better intrinsic energy resolution.

The use of temperature detectors to study nuclear phenomena was first suggested by Simon [67] about 60 years ago. In 1949 Andrews detected for the first time alpha particles using superconductive bolometers [68]. The possibility to use thermal detector for many topics of research as solar neutrino spectroscopy, X ray spectroscopy, material contamination analysis, WIMPS detection and rare processes research was a strong motivation to the development of this technique.

Thermal detectors can be divided into two main categories:

- *composite detectors:* the detector consists of two separate parts, the absorber and the phonon sensor. To this category belong bolometer, for which the sensor measure the absorber temperature changes;

- *monolithic detectors:* absorber and sensor coincide.

Actually the best performances have been obtained with the first kind of detectors, to which this chapter will be devoted.

2.1   Principle of operation of bolometers

A bolometer consists of three main components (Fig.2.1):

Particle absorber : where the particles deposit their energy. Through the measure of its temperature rise it's possible to measure the released energy. The absorber material can be chosen quite freely, the only requirements being, in fact, reasonable thermal and mechanical properties. The absorber can therefore be easily built with materials containing any kind of unstable
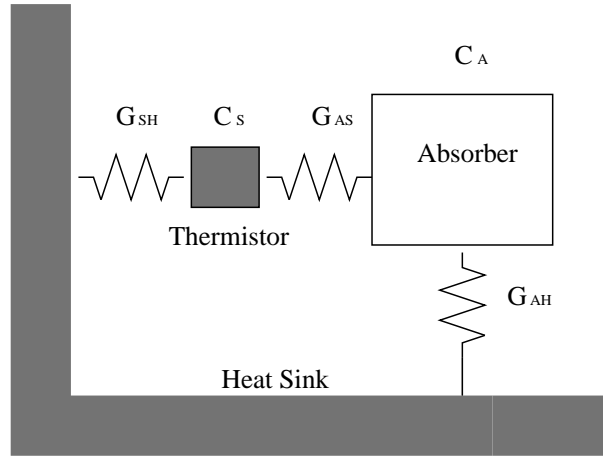
Figure 2.1: *Scheme of a bolometric detector.*

isotopes and many interesting searches are therefore possible (e.g. beta decay spectroscopy, neutrinoless double beta decay and dark matter). The absorber mass can range from few micrograms to few kilograms.

Temperature sensor : it is needed to measure the temperature rise induced by the particle interaction in the absorber. Different kind of thermometers exists, depending on the material and on the process through which the temperature signal is converted in an electric signal.

Thermal link : it mainly depends on the way the massive crystal is held to the structure (heat sink). Together with the system heat capacity it influences the time response of the device.

In a naive model we can assume the detector as a heat capacity C (absorber) in thermal connection with a heat sink (kept at temperature T_0) through a thermal conductance G (Fig.2.1).

If $T(t)$ is the temperature of the absorber as a function of time and we assume that $\Delta T \equiv |T(t) - T_0| \ll T_0$ for all times t, so that C and G can be treated as constants, then an instantaneous deposition of an energy ΔE in the absorber gives rise to a temperature pulse:

$$\Delta T = \frac{\Delta E}{C(T)} \tag{2.1}$$

whose time development is described by:

$$\Delta T(t) = \frac{\Delta E}{C} \exp(-\frac{t}{\tau}) \tag{2.2}$$

where the time constant $\tau = C(t)/G(t)$. As it can be easily seen from eq. (2.1) and eq. (2.2) the heat capacity is a crucial parameter for this kind of devices since the smaller it is the higher and faster are the signals.

2.2 Absorber

From eq. (2.1) and (2.2) it's easy measurable temperature variations are obtained with materials having a low heat capacity at the working temperature. This requirement is easily fulfilled by a wide choice of absorber materials working at very low temperature.

21

At low temperature the specific heat of a given crystal can be written as

$$c(T) = c_r(T) + c_e(T) + c_m(T) \tag{2.3}$$

where c_r is the lattice contribution and c_e the electronic contribution to the crystal specific heat and c_m is the magnetic contribution. The first term, that is the only contribution existing for dielectric and diamagnetic materials is proportional to T^3:

$$c_r(T) = \frac{12}{5}\pi^4 k_B N_A \left(\frac{T}{\Theta_D}\right)^3 \tag{2.4}$$

where k_B, N_A and Θ_D are the Boltzmann constant, the Avogadro number and the Debye temperature, that is specific for every different material. The correspondent heat capacity C(T) for $T < \Theta_D$ is proportional to the mass of the absorber and to $(T/\Theta_D)^3$.

The electronic contribution c_e depends on the conductive or superconductive nature of the material. For conductors c_e is proportional to T while for superconductors, at temperatures lower than the critical temperature, c_e decreases exponentially with temperature

The eventual magnetic nature of the material give rise to the last term, that is inversely proportional to T^2.

From these considerations it is clear that the best choice for a low temperature detector is based on dielectric and diamagnetic crystals or superconductive materials with critical temperature considerably higher than the working temperature.

In addition the dependence of the Debye temperature on the mass number A and on the material density ρ as $\Theta_D \propto A^{-\frac{1}{3}} \cdot \rho^{-\frac{1}{6}}$ suggests that low atomic mass number and density means a lower heat capacity, even if we have to keep in mind that a higher atomic number guarantees a higher detection efficiency for electrons and gammas.

2.2.1 Thermalization process

The energy released by a particle in the absorber goes through a long thermalization process. The deposited energy is downgraded via interaction with the nuclear and the electronic systems into out of equilibrium phonons [69]. This initial population successively decays via different processes in an equilibrium Bose-Einstein distribution of thermal phonons.

Nuclear channel: The energy released by the particle into the nuclear branch (E_N), via elastic scatterings, produce vibrational excitations, called phonons. For primary electromagnetic radiation the fraction of deposited energy that is released in this channel is negligible. It must be taken into account mainly dealing with alpha or heavier particles. Unfortunately only a fraction of the energy E_N is downgraded to phonons. Part of it may in fact be used to produce structural defects in the absorber. Owing to the low operating temperature these defects are stable and can constitute energy traps. The statistical fluctuation of the number of the produced defects can worsen the energy resolution.

Electronic channel: The energy released in the electronic channel (E_e) is usually spent to excite electron-hole (e-h) pairs. The incoming particle is slowed down in a few μm (heavy particles) or mm (electrons) from its interaction point and usually it stops in the crystal. Along its track it produces many e-h pairs, having at the beginning very high spatial density and energy. These charge carriers interact first with each other and spread very quickly in the crystal. As a quasi equilibrium situation is reached, they undergo their final degradation via direct interaction with the lattice site: these interactions produce phonons.

During this step undesirable processes could take place, indeed a fraction of the pair energy can leave the crystal or can be stored in stable or metastable states instead of being converted into crystal lattice excitations.

Let's consider now the phonon thermalization processes. The initially produced phonons are high energy and low momentum phonons, belonging to the optical brach. These primary phonons depart from the particle interaction region and decay in the longitudinal acoustic (LA) branch in a very short time ($10 \div 100$ ps). At this point the phonon dynamic is dominated by the an-harmonic decay $LA \to LA + TA$,where TA is the transversal acoustic branch. The rate of this decay channel is proportional to E^5. When the phonon energy is near to ~ 10 meV, the an-harmonic decay channel is less important and the phonon dynamics is dominated by the scattering on impurities. The conversions towards lower energies become a slow process with times of the order of ~ 0.1 sec.

After a certain number of decays the mean free path of the phonons becomes larger than crystal dimensions. In pure crystals this means that phonons propagates ballistically until they reach the crystal surface [70]. Phonons that are not absorbed by sensor will be reflected by surfaces and therefore they can undergo other decay processes leading finally to a complete thermalization.

Since fast (ballistic) and thermal phonons have separate development times, two kind of phonon sensor have been devised [72]:

- **ballistic phonon sensors:** used to detect phonons at the crystal surface interface and used for spatial event reconstruction [71];

- **thermal phonon sensors:** in which it is assumed a fast and complete thermalization of the phonons.

2.2.2 Intrinsic energy resolution

To evaluate the intrinsic resolution of a device we need to know the statistical fluctuation of the number of elementary events contributing to a signal. Every elementary event (atomic excitation or ionization for conventional detectors, phonons for thermal detectors) is associated to an activation energy called ϵ, that is the minimum amount of energy required to produce an elementary quantum. Because of the loss of energy in channels different from the detected one, the actual amount of energy necessary to generate a quantum is generally higher than ϵ and can change from event to event. We will refer to its average value as ϵ_A. So, for an energy release E, the number of generated elementary events will be

$$N = \frac{E}{\epsilon_a} \tag{2.5}$$

The intrinsic energy resolution is limited by the fluctuation in the number of the produced elementary excitation events. Assuming Poisson statistics we can evaluate this fluctuation as $\Delta N = \sqrt{N}$, that means a theoretical energy resolution (FWHM) of

$$\frac{\Delta E}{E} = 2.35 \frac{\Delta N}{N} = 2.35 \sqrt{\frac{F \epsilon_a}{E}} \tag{2.6}$$

where F is the Fano factor [73], introduced to take into account correlation effects (non statistical behavior) of the events [74]. As it can be see form eq. (2.6) the intrinsic resolution for conventional detectors is proportional to $\sqrt{E}$.

Just to understand quantitatively what eq. (2.6) means let's consider the energy activation for a Germanium Diode and for a thermal detector. For the first device ϵ_a is around 3 eV, although the

band energy gap is 0.7 eV. This difference is due to the big fraction of energy loss in other channels. Actually, since the whole released energy is finally converted to thermal phonons, their number does not fluctuate and we should expect an infinite resolution. Phonon fluctuation mechanism is however present and is related to the thermal link maintaining the dynamical thermal equilibrium with the heat sink.

For thermal detector somehow different considerations can be therefore taken into account. If we explicit the expression of E and ϵ_a for this device we obtain for the number of elementary events (thermal phonons with average energy $k_B T$) held in the detector at a given temperature T:

$$N \; = \; \frac{C(T) \cdot T}{k_B \cdot T} \; = \; \frac{C(T)}{k_B} \tag{2.7}$$

where C(T) is the heat capacity of the detector material. Assuming also in this case Poissonian statistic we can derive from eq. (2.7) and (2.6) the expression for the intrinsic resolution for thermal detectors:

$$\Delta E \; = \; \Delta N \cdot k_B T \; = \; \sqrt{\frac{C(T)}{k_B}} k_B T \; = \; \xi \sqrt{K_B C(T) T^2} \tag{2.8}$$

where ξ is a dimensionless factor of the order of 10, that accounts for details of the sensor, of the heat sink and for the temperature dependence C(T).

It should be stressed that, according to eq. 2.8, the resolution for bolometers is *independent* of E, with impressive "theoretical" expectations even in the case of a massive crystal: a TeO$_2$ crystal with a mass of 1 kg operating at 10 mK could measure energy depositions of the order of few MeV with a resolution of about 20 eV, more than two order of magnitudes better than conventional devices. It should be also stressed, however, that this "thermodynamic limit" doesn't take into account other sources of energy fluctuations (e.g. metastable electron-hole states or long-lived non thermal phonons) which participate to the energy deposition process and whose contributions to the energy resolution worsening should be therefore minimized.

2.3 Phonon sensor

As previously said for a bolometer, the phonon sensor is actually a temperature sensor (i.e. a thermometer), able to convert a temperature signal into an electrical signal. Using this device we can have a voltage measurement of the energy released by a particle in the absorber.

There is a big variety of thermometers. The most common used can be divided in two classes: semiconductor thermistors (STs) and transition edge sensors (TESs). For both type of thermometers the temperature rise is associated to a variation in the electric resistance of the device. The parameter used to characterize a thermistor is the logarithmic sensitivity A, defined as

$$A \; = \; \left| \frac{d \log R(T)}{d \log T} \right| \tag{2.9}$$

with values in the range $1 \div 10$ for STs and in the range $10^2 \div 10^3$ for TESs. This parameter is used to evaluate the effectiveness of a thermometer since it measures the device efficiency in converting a small temperature rise in a detectable electric signal.

2.3.1 Transition Edge Sensors

This device consist of a thin superconductive film, usually biased as to keep the working temperature within the superconductive transition range. There are two different techniques to work with TESs:
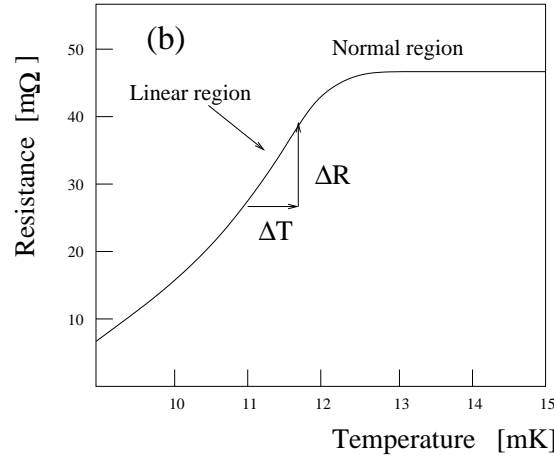
Figure 2.2: *Typical superconductive transition characteristic for TES.*

- linear technique (see Fig. 2.2(b))

- complete technique

In the first case the working temperature is chosen in the linear region of the transition curve. In this way the resistance variation ΔR will be proportional to the temperature variation ΔT. The disadvantage of this method is the narrow dynamic range, since it can't detect energy depositions leading to temperatures larger than the superconductive transition temperature.

In the second method the working temperature is chosen to lay below the linear region. In this case the dynamic range is wider but the response is no longer linear.

A complex technique was developed, based on the electrothermic feedback, to overcome the problem, leading to linear response with sufficiently large dynamic range.

Superconductive Transition Edge sensors are intrinsically fast and can be used to detect athermal phonons. also

2.3.2 Semiconductor thermistor

This phonon sensor device is quite slow. Semiconductor thermistors cannot in fact hold signal rates larger than some Hz. This limits their use to rare events measures.

STs are heavily doped high resistance semiconductors, with an impurity concentration slightly below the metal-insulator transition [75]. *Good* thermistors require a higly homogeneous doping concentration which is achieved, in the case of NTD (Neutron Transmutation Doped) thermistors, by means of thermal neutron irradiation throughout the entire volume [76]. The bombarding neutrons induce nuclear reactions on the various target isotopes, leading to the formation of n- and p- dopant. The compensation level K between donor and acceptor atoms can be controlled by changing the flux of the neutron irradiation, thus leading to different behavior of the sensor. For typical compensation levels in the range $0.23 \div 0.41$, the electrical conductivity of these heavily doped semiconductors at low temperature strongly depends on the temperature according to the *hopping* and *variable range hopping* (VRH) mechanisms [77]. In general the resistivity varies with temperature as

$$\rho = \rho_0 e^{\left(\frac{T_0}{T}\right)^\gamma} \tag{2.10}$$

where ρ_0, T_0 and γ depends on the doping concentration. In the case of VRH, the value of γ is 1/2.
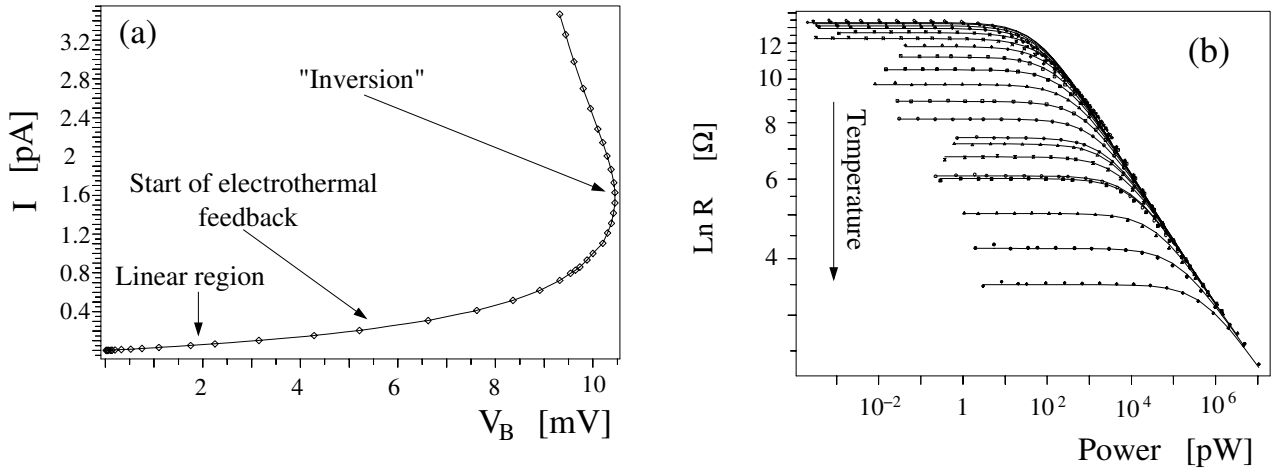
Figure 2.3: *Typical load curve for a thermistor at T= 8 mK) (a) and resistance-power curves for a thermistor at different base temperatures (b).*

The sensitivity parameter A for semiconductor thermistor thus takes the form:

$$A(T) = \left| \frac{d \ln R}{d \ln T} \right| = \gamma \left(\frac{T_0}{T} \right)^\gamma \quad \text{with } R(T) = \rho(T) \frac{l}{s} = R_0 \exp \left(\frac{T_0}{T} \right)^\gamma \tag{2.11}$$

where l and s are the distance between the contacts and the cross section of the thermistor, respectively. The value of the sensitivity is usually in the range $2 \div 10$.

The values of R_0, T_0 and γ must be experimentally measured for each thermistor (characterization process). The measure of the characteristic R(T) for each thermistor is performed thermally coupling the sensor to a low temperature heat sink using a high conductivity epoxy. The temperature T_B (base temperature) of the heat sink is then varied ($15 \div 50$ mK) while a steady current I (bias current) flows trough the thermistors and a voltage $V = IR$ appears across them. This produces a power dissipation which raises the temperature and acts back on the resistance, until an equilibrium is reached. This phenomenon makes the $V - I$ relation deviate from linearity. This characteristic behavior of bolometers is often referred to as "electrothermal feedback". The static resistance is simply the ratio V/I while the dynamic resistance is the tangent at the $V - I$ curve. By further increasing the bias current the dynamic resistance crosses the so called *inversion point* (where it vanishes) and becomes then negative. For semiconductor thermistors, a typical $V - I$ curve, usually referred to as *load curve*, is represented in Fig.2.3 (a). By a combined fit to a set of load curves at different base temperatures, all the thermistor parameters are evaluated (see Fig.2.3 (b))

2.4   Detector operation

Thanks to the strong dependence of the sensor's resistivity with the temperature (eq. 2.10) a thermal signal, due to an energy deposition in the absorber, can be converted into electric signal. This is accomplished by means of a bias circuit as shown in Fig. (2.4). where R_L are load resistors, V_T is the bias voltage and $V_B(T)$ is the electric signal across the bolometer. The current across the sensor dissipates a power P which increases its temperature acting back on the resistance $R(T)$. This is the electrothermical feedback effect described above.
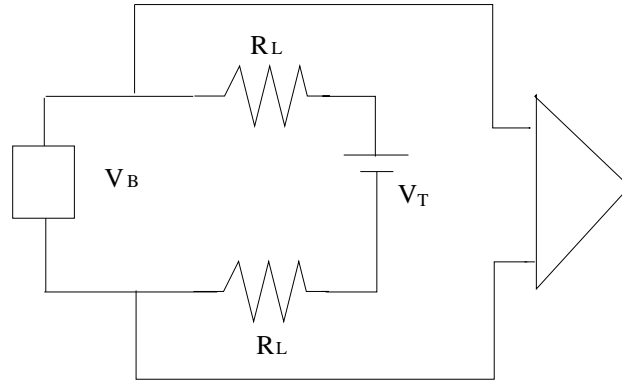
Figure 2.4: *electric scheme of the bolometer bias circuit.*

2.4.1 Voltage signal amplitude

Considering the circuit in Fig. (2.4) and eq. (2.9), we can derive the relation between the maximum potential drop across the thermistor (V_B), the thermistor parameters and the deposited energy:

$$\Delta V_b = \frac{R_{Load}R_B}{(R_{Load} + R_B)^2} \, V_{Tot} A \frac{\Delta T_b}{T_b} \approx \frac{E}{CT_b} A\sqrt{P}\sqrt{R_B}, \tag{2.12}$$

where E is the deposited energy, T_b and ΔT_b are the operating temperature and the temperature increase of the bolometer, A is the thermistor sensitivity, C is the heat capacity of the absorber and P is the electrical power dissipated on the thermistor by the Joule effect. This expression vanishes both in the limit $P \rightarrow 0$ and $P \rightarrow \infty$. When the thermistor is operated as a detector sensor, a steady current I flows through it and, in a steady condition, its electrical and thermal parameters are described by a point on the detector $V - I$ curve (working point). The optimization of the working point is an important task and must be performed experimentally for each detector. The *optimum point* is chosen by maximizing the signal/noise ratio. Since the electronic sources of noise decrease with the resistance of the bolometer the best *working point* corresponds to a bias voltage slightly higher than the one corresponding to the bias V_T for which the amplitude of the voltage pulse ΔV_B has its maximum value (see Fig. (2.5)).

The experimental determination of the optimum point can be accomplished by means of a fixed resistance (*heater*) directly glued onto the crystal through which it is possible to dissipate a known joule power into the crystal in a manner equivalent to a particle energy deposit. A typical bolometer response as a function of detector bias is shown in Fig.2.5.

The use of the *heater* also plays a fundamental role in the stabilization of the bolometer response which changes with the temperature of the heat sink [78].

2.4.2 Noise sources

The main noise sources limiting the resolution for thermal detectors can be classified in two main categories:

- **intrinsic noise:** this is an unavoidable source of noise, strictly dependent on the physical characteristics of the absorber and of the sensor. It gives the reachable theoretical limit for the energy resolution.
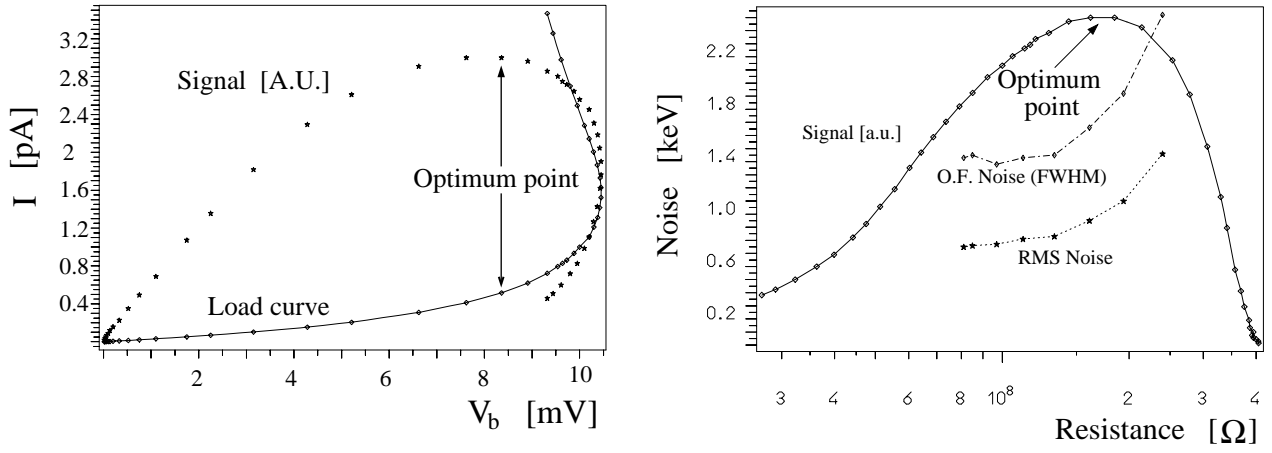
Figure 2.5: left panel: *evaluation of the* optimum point *of a bolometer;* right panel*: evaluation of operation point which maximizes the signal/noise ratio.*

- **extrinsic noise:** it accounts for all the noise sources due to the experimental set-up, as the cryogenic system and the electronic read-out system. In this category can be also included other sources of noise, as electromagnetic interferences and mechanical microphonic noise. This noise actually dominates the energy resolution of low temperature experiments.

In this chapter only a description of the intrinsic noise will be given, leaving the analysis of the extrinsic sources for the chapter devoted to the detector details.

Johnson noise

From the electric point of view and using a naive model the thermistor can be considered a resistor. It constitutes therefore a source of Johnson noise. The power spectrum noise for a resistance $R \simeq 150\ M\Omega$ working at a temperature $T_B \simeq 12\ mK$ is:

$$\sqrt{e_n^2(\omega)} \;=\; \sqrt{4kTR_B} \simeq 10^{-8} \frac{V}{\sqrt{Hz}} \tag{2.13}$$

thus meaning an rms value of about 30 eV, one order of magnitude lower than the usually observed noise value.

In a more realistic model, that takes into account the elettrothermic feedback effect, the thermistor should be considered a complex impedance. This implies that its noise power spectrum depends on the frequency. In any case the value given in eq. (2.13) gives a good estimation for an upper limit of the actual value.

Thermodynamic noise

As previously said the number of phonons exchanged between the thermistor and the heat sink is subject to statistical fluctuation. This fact limits the intrinsic energy resolution, according to eq. (2.8) and corresponds to and rms value of 20÷100 eV. As can be seen from this equation the only parameter depending on the details of the detector is ξ. With a proper optimization work it can be reduced to values of the order of unity, lowering in this way the intrinsic limit of the detector resolution.

Chapter 3

TeO2 bolometric experiments for DBD0ν research

Introduction

After some years of research and development the Milano group started in 1989 a series of bolometric experiments in the Gran Sasso Laboratory (LNGS) to search for the DBD0ν of ^{130}Te

The preliminary experiment was performed with 73 g and 334 g single TeO$_2$ crystals, reaching a limit on $T_{1/2}^{0\nu}$ of ^{130}Te of 2.1×10^{22} years (90% CL).

The second step was an array of 4 detectors, 340 g each, to study the feasibility of a large massive experiment made by identical bolometers. The cumulative limit obtained on $T_1^{0\nu}/2$ of ^{130}Te was 2.39×10^{22} years (90% CL) [79].

At the end of September 1997, a new array consisting of 20 TeO$_2$ 340 g crystals was operated in the LNGS [80, 81]. The new achieved limit on $T_{1/2}^{0\nu}$ of ^{130}Te was 9.5×10^{22} years (90% CL). This experiment, named MiDBD, constitutes the first step towards the next generation experiment CUORE.

The knowledge acquired in terms of detector performance optimization and background reduction was delivered to the realization of a second large mass bolometric experiment, CUORICINO, a 62 TeO$_2$ array for a total mass of 41.7 kg. This experiment is placed in the hall A of the LNGS, in the same dilution refrigerator previously hosting the MiDBD array, and is presently collecting data. CUORICINO is a self-consistent experiment but at the same time it is a test facility intended to verify the technical feasibility of CUORE (Cryogenic Underground Observatory for Rare Events).

The CUORE experiment, already approved, will be the final step of this series of experiments, and is designed to reach the sensitivity to explore the Almost Degenerate and Inverted Hierarchy hypothesis of the neutrino mass spectrum. It will consist of a tightly closed structure of 988 TeO$_2$ 760 g crystals, for a global mass around 800 kg. These experiments are hosted in the underground laboratory of Gran Sasso. The mountain in fact constitutes a 3500 m.w.e. shield against cosmic radiation.

3.1 Which absorber for a bolometric experiment

As it was said in chapter 2, the bolometric technique offers a wide choice of DBD candidates (as, for instance, ^{48}Ca, ^{76}Ge, ^{82}Se, ^{100}Mo, ^{116}Cd, ^{130}Te and ^{150}Nd), the only requirements being that the candidate nucleus be part of a compound which can be grown in the form of a crystal with good thermal and mechanical properties.
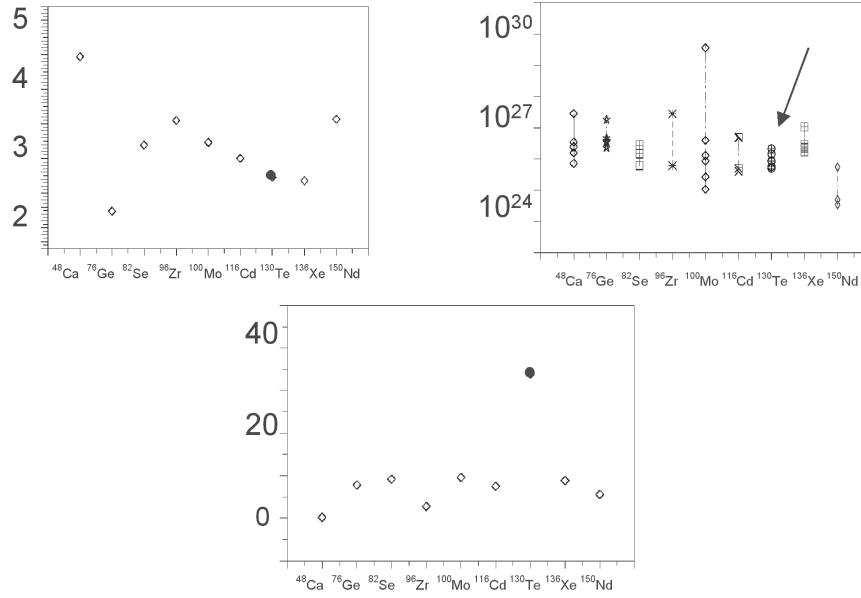
Figure 3.1: *Comparison between the transition energy (a), the half-life for DBD0ν given $< m_\nu >$=0.1 eV (b) and the natural isotopic abundances (c) for the different DBD candidates.*

There are however some features that can be taken into account to choose the best nuclide.

- **Q-value:** the phase space of the transition $G^{0\nu}$ is proportional to Q^5, where Q is the energy transition of the decay. This means that the higher is Q, the bigger is the probability for the decay to occur. In Fig. (3.1)a a comparison of the transition energy for the various DBD candidates is reported. The DBD Q-value for ^{130}Te is 2528.8 ± 1.3 keV and is reasonably high. The Q-value is also important with respect to the natural radioactivity background. The Q-value of ^{130}Te happens to be between the peak and the Compton edge of the 2615 keV line of ^{208}Tl , which leaves a clean window to look for the signal.

- **Nuclear dynamics:** As it was illustrated in chapter 1 (see eq. (1.37)), the lifetime for DBD0ν is inversely proportional to the factor of merit $F_N \equiv G^{0\nu} \mid M_F^{0\nu} \mid^2$. The matrix elements $\mid M_F^{0\nu} \mid^2$ are dominated by the nuclear dynamics and differ from one nuclide to another. As it can be seen from Tab. (1.2) it is apparent that, no matter the nuclear model it is used to compute the neutrinoless DBD matrix elements, the nuclear factor of merit of ^{130}Te are a factor 5-10 more favorable than those of ^{76}Ge (the emitter for which the best DBD0ν half-life limits have been achieved so far). This translates into a factor 2 to 3 better as far as the $\mid < m_\nu > \mid$ is concerned. A comparison between the calculated DBD0ν half-life (given $\mid < m_\nu > \mid$ of 0.1 eV) for the various DBD candidates is reported in Fig. (3.1)(b).

- **Isotopic Abundance:** As it can be seen from eq. (1.57) this parameter plays an important role in determining the sensitivity of a DBD experiment. Isotopic enrichment is not always practically feasible and is often very expensive. From this point of view the isotope ^{130}Te is an optimum choice since its isotopic content in natural tellurium is 33.87%. A comparison between the natural isotopic abundances of the different DBD candidates is shown in Fig. (3.1)(c).

Taking into account the previous considerations we can conclude that ^{130}Te is an excellent candidate for DBD0ν research with a bolometric technique.

30

The chosen compound to make the absorber is tellurium oxide TeO_2. This choice instead of natural tellurium was taken since the crystals grown with pure Te evidenced poor mechanical properties and a predisposition to break after a few thermal cycles. In addition the Debye Temperature Θ_D of TeO_2 is higher than that of pure tellurium, this implying a lower heat capacity and thus a higher pulse amplitude for a given working temperature. TeO_2 crystals showed also a good intrinsic radiopurity (less than 1pg/g in ^{232}Th and ^{238}U), a fundamental requirement to study rare events as DBD0ν.

The Milano group has tested also other isotopes and compounds. This is the case of as $^{48}CaF_2$, an excellent candidate due to the large transition energy of ^{48}Ca and the good thermal properties of calcium fluoride crystals. The very low natural abundance of ^{48}Ca makes on the other hand this choice very expensive, since it requires a strong enrichment. Other tested compounds are $^{100}MoPbO_4$, $^{116}CdWO_4$ and $^{150}NdF_2$. The first, despite the good thermal response faces the problem of an excessive counting rate due to the presence of ^{210}Pb. $^{116}CdWO_4$ is an excellent scintillator (this providing an additional tool for background suppression), but presents the same problem of low natural isotopic abundance as $^{48}CaF_2$. Recent tests on $^{150}NdF_2$ crystals showed a considerable difficulty to cool down to low temperatures these crystals.

Taking into account all these considerations we see that the choice of the isotope ^{130}Te in the form of TeO_2 crystals for DBD0ν research is the only presently available with moderate costs and good features for a rare event research.

As presented in the introduction of this chapter different size TeO_2 crystals have been used in the various series of bolometric experiments performed by the Milano group: 73 g and 334 g crystals for the first tests, 3x3x6 cm^3 detectors of 340 g each for the first large mass experiment MiDBD, and finally 5x5x5 cm^3 TeO_2 crystals with a mass of 790 g each in CUORICINO and CUORE. The found similar behavior for the different size detectors with respect to signal rise and decay time, pulse height and energy resolution gives indications that the increased size of the crystals doesn't affect the performances. Also bigger size crystals of 6x6x6 cm^3 have been tested, leading to good results but some R&D would be required for their optimization. This dimension seems to be the present growing limit for TeO_2 crystals.

3.2 The sensor

As described in section (2.3.2) the sensor is the fundamental device to convert the temperature rise due to an energy deposition in the absorber into an electric signal. The sensors used in MiDBD and in CUORICINO, and that are going to be used in CUORE are Neutron Transmutation Doped Germanium thermistors, operated in the Variable Range Hopping (VRH) conduction regime with a Coulomb gap [82, 83, 84]. The resistance behavior of these devices as a function of T follows the relation:

$$R = R_0 \exp(T_0/T)^{\gamma}; \qquad \gamma = 1/2. \tag{3.1}$$

(see the analogous behavior for the resistivity in equation (2.10)). The VRH regime occurs in Ge when it is "doped" close to the Metal to Insulator Transition, which is $\sim 6\times10^{16}$ atoms / cm^3. This is achieved by exposing a Ge sample to thermal neutron radiation in a nuclear reactor. One of the most significant parameters characterizing the thermal response is the sensitivity A, already introduced in chapter 2 and defined in equation (2.9). The value of this parameter depends on the neutron irradiation dose.

Even if other simpler Ge doping methods exist (i.e. melt doping), they usually cannot achieve the necessary uniformity and the only technique available for producing such uniform doping is NTD. In typical applications, the neutron absorption probability for a 3 mm thick wafer of Ge is small, on the order of 3 %, leading to a very homogenous, uniform absorption process. The most important

aspect of this process is that ^{70}Ge transmutes into Ga, an acceptor, and ^{74}Ge transmutes into As, a donor, the primary active dopants in NTD Ge. In this process, one places the Ge in a nuclear reactor where the following reactions take place:

$$^{70}Ge\ (21\%) + n\ \rightarrow\ ^{71}Ge\ (\sigma_T = 3.43 \pm 0.17b,\ \sigma_R = 1.5b)$$
$$^{71}Ge\ \rightarrow\ ^{71}Ga\ (t_{1/2} = 11.4day) \qquad Acceptor \tag{3.2}$$

$$^{74}Ge\ (36\%) + n\ \rightarrow\ ^{75}Ge\ (\sigma_T = 0.51 \pm 0.08b,\ \sigma_R = 1.0 \pm 0.2b)$$
$$^{75}Ge\ \rightarrow\ ^{75}As\ (t_{1/2} = 83min) \qquad Donor \tag{3.3}$$

$$^{76}Ge\ (7.4\%) + n\ \rightarrow\ ^{77}Ge\ (\sigma_T = 0.16 \pm 0.014b,\ \sigma_R = 2.0 \pm 0.35b)$$
$$^{77}Ge\ \rightarrow\ ^{77}Se\ (t_{1/2} = 38.8hr) \qquad Double\,Donor \tag{3.4}$$
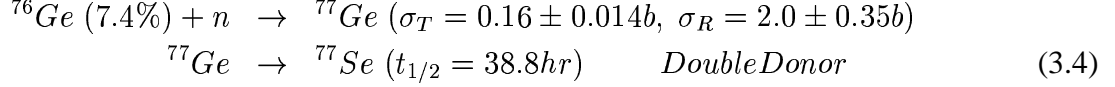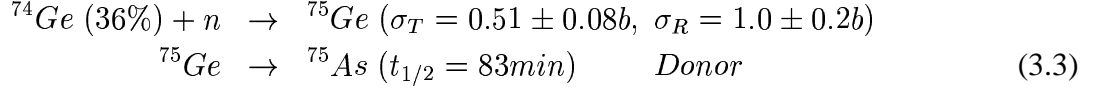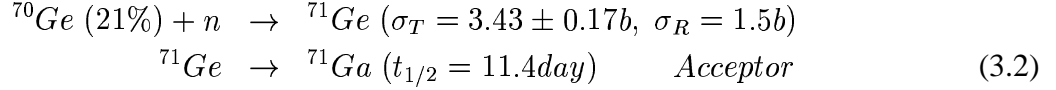
where σ_T and σ_R refer to the thermal and epithermal neutron capture cross sections, respectively.

Since the doping level of the Ge needs to be on the order of 1×10^{17} atoms/cm^3, a very high flux reactor is necessary. Even more important is the stability of the neutron flux and its energy distribution.

The significant quantity involved in thermistor performance is the net dopant concentration which is equal to the concentration of Ga atoms minus the concentration of As atoms minus twice the concentration of Se atoms. Unfortunately, to measure the thermal performance of the thermistor, one needs to wait for the decay of the activation product ^{71}Ge (11.4 day), which requires approximately one year. Previous measurements carried out in the Gran Sasso Laboratory [85] have shown that the residual activity of the NTD thermistors becomes fully tolerable in an experiment with thermal detectors already a few months after irradiation. Following the radioactive decay period, the NTD germanium is first heat treated to repair the crystal structure then cut into 3×3×1 mm^3 strips. The thermistors then need to be characterized at low temperatures, following the procedure described in section (2.3.2).

3.3 The single module

Once characterized the NTD germanium thermistors are glued to the TeO$_2$ crystal by 9 spots of Araldit rapid epoxy, of 0.4 to 0.7 mm deposited on the crystal surface by means of an array of pins. The height of each spot is 50 μm. This procedure was found to be reasonably reliable and reproducible in the MiDBD experiment [81, 86]. The heat conductance of the epoxy spots was measured in Milan and the phenomenological relation for its temperature dependence was found to be $\sim$2.6 $\times 10^{-4}$ (T[K])^3 watts per degree kelvin per spot.

Silicon chips with a heavily doped meander structure and a resistance between 50 to 100 kΩ are also glued on to each crystal. They are used as Joule heaters to inject a uniform energy in the crystal in order to monitor the thermal gain and correct its variations off-line to stabilize the response of the bolometers. This topic will be discussed in more details later on. The signal is read by means of two 50 μm diameter gold wires, ball bonded to metalized surfaces on the thermistor and thermally coupled to the crystals copper frames. This copper structure constitutes the heat sink, being in thermal contact with the coldest point of the dilution refrigerator (the mixing chamber).

The TeO$_2$ crystals holder structure is crucial to detector performance, and must fulfill a number of sometimes contradictory criteria:
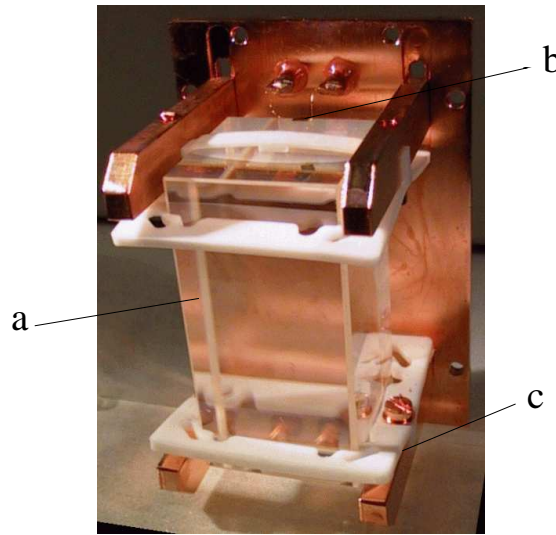
Figure 3.2: *The single module used in the first run of MiDBD. It's possible to see the crystal (a), the thermistor with the gold wires (b), the copper frame and the PTFE pieces (c).*

1. the crystals must be rigidly secured to the frame to prevent power dissipation by friction caused by unavoidable vibrations, that can prevent the crystal from reaching the required temperature and can produce low frequency noise;

2. the thermal conductance to the heat sink (copper frame) must be low enough to delay the re-cooling of the crystal, following a heat pulse, so that the pulse decay time (re-cooling time) is much longer than the rise time;

3. the heat conductance must be high enough to guarantee efficient cooling (this is in constrast with the previous requirement);

4. the frame must compensate for the differences in thermal expansion coefficients of the various materials used;

5. and finally, only materials selected for low radioactivity can be used.

The materials used for the holding structure of the crystals are copper and PTFE; they can both be obtained with very low levels of radioactivity. Copper has a thermal conductivity and specific heat high enough to be an ideal heat bath, and has excellent mechanical properties.

PTFE is used between the copper frame and the crystals. It has low heat conductance and low heat leak [87]. It compensates for the differences between coefficients of thermal expansion of copper and of TeO_2 . In Fig. (3.2) an example of a single module used in the first run of the MiDBD experiment is shown.

3.4 Detector structure

The single detector module is inserted in a modular structure that can differ from one experiment to another, since the R&D so far performed by the Milano group, lead to some modifications of the original design, in order to optimize the detector performances with respect to thermal response and to background reduction. The details of the different structures used in the MiDBD and CUORI-CINO experiment, and the one designed for CUORE will be discussed in this section.
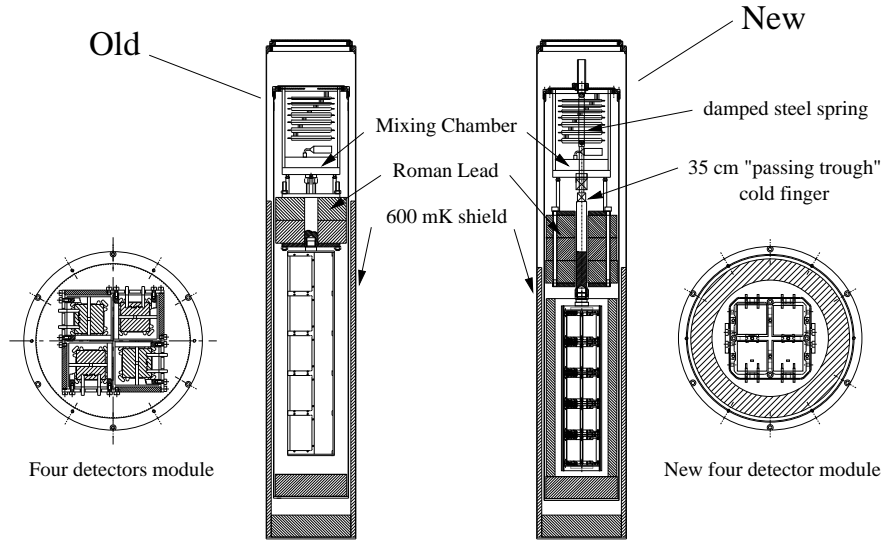
Figure 3.3: *Scheme of the MiDBD detectors: first run (a), second run (b).*

Figure 3.4: *4 crystal module of MiDBD-II.*

3.4.1 MiDBD

The MiDBD experiment built up in 1997, consisted of a of 20 crystals of TeO_2 of $3\times3\times6$ cm^3 each (340 g), for a total mass of 6.8 kg. It was operated in the Hall A dilution refrigerator until December 2001. Sixteen MiDBD crystals were made of natural TeO_2. Of the remaining four, two were isotopically enriched at 82.3 % in ^{128}Te and other two at 75.0 % in ^{130}Te.

The elementary module was the single module detector shown in Fig. (3.2). All the 20 single modules were arranged in a 5 planes tower-like structure, completely enclosed in a copper box. The detector tower was mounted inside the inner vacuum chamber (IVC) of the dilution refrigerator and thermally liked through a cold finger to the coldest point of the dilution refrigerator, at a temperature of about 10 mK.

The tower was shielded with an internal Roman lead layer of 1 cm minimum thickness. Additional layers of 10 cm Roman lead were placed above and below the tower, in order to shield the detectors against the unavoidable radioactive contaminations due to some fundamental components of the cryogenic system. A scheme of the MiDBD setup is shown in Fig. (3.3)a.

The big R&D effort devoted to improve both the knowledge and the reduction of the background sources and the performance of the new detector mounting system proposed for CUORICINO and CUORE, lead in 2001 to a second run (MiDBD-II) in which the following improvements have been

implemented:

- all crystals have been thoroughly lapped with previously tested low radioactivity powder to reduce the surface contamination introduced by the original production process in China. All these operations and the final mounting of the tower were carried out in a clean room;

- the copper mounting structure elements were subject to dedicated etching process aiming to reduce radioactive contaminants;

- the amount of teflon used in every single detector module was reduced;

- a more compact 4 crystal module assembling of the crystals has been adopted (see Fig. (3.4)). This allowed the addition of an internal Roman lead shield of 2 cm minimum thickness and of a layer of 5 cm above the tower;

- a spring suspension system to reduce mechanical vibrations;

- an external PET neutron shield was added.

A scheme of the new detector setup is shown in Fig. (3.3)b.

3.4.2 CUORICINO

The CUORICINO detector is a tower-like structure made by eleven planes of 4-crystal modules (5x5x5 cm^3 crystals) and two additional planes of 9-crystal modules (3x3x6 cm^3 crystals)(see Fig. 3.5). The 18 small size crystals were taken from the MiDBD experiment. CUORICINO contains therefore 44 TeO$_2$ crystals of 790 g mass and 18 TeO$_2$ crystals of 330 g mass. The total TeO$_2$ mass in CUORICINO is 40.7 kg. All the crystals are made of natural tellurium but the 4 isotopically enriched crystals previously used in MiDBD.

Particular care was devoted to selection and cleaning of the materials used for the construction of the CUORICINO array. The crystals were grown from pre-tested low radioactivity materials by the Shangay Instituts of Ceramics in China and shipped to Italy where they were surface treated with specially selected low contamination powders. The mechanical structure of the array was made exclusively in OFHC copper and in teflon, both previously measured to verify the extremely low radioactive content. All the copper and teflon parts of the mounting structure were separately treated with acids to remove any possible surface contamination. The array was assembled in an underground clean room in a N$_2$ atmosphere to avoid Rn contamination. The tower just after assembly completion and the details of the two different used modules are shown In Fig. 3.5.

The tower is covered with copper plates and mounted in the same 1000 μW helium liquifier used for the MiDBD experiment. Due to the bigger dimension of the CUORICINO tower with respect to MiDBD, two of the cryostat thermal shields had to be replaced. To avoid vibrations from the overall facility to reach the detectors the tower is mechanically decoupled from the cryostat through a steel spring. The array is surrounded by a ~ 1 cm thick roman lead shield (Fig. 3.5) to avoid radioactivity coming from the cryostat. For the same purpose two roman lead discs, 7.5 cm and 10 cm thick, are positioned just below and above the tower respectively. The amount of internal roman lead shield is less than the one used in the MiDBD experiment (1 cm in CUORICINO vs. 3 cm in the previous experiment) due to the bigger dimension of the CUORICINO tower.
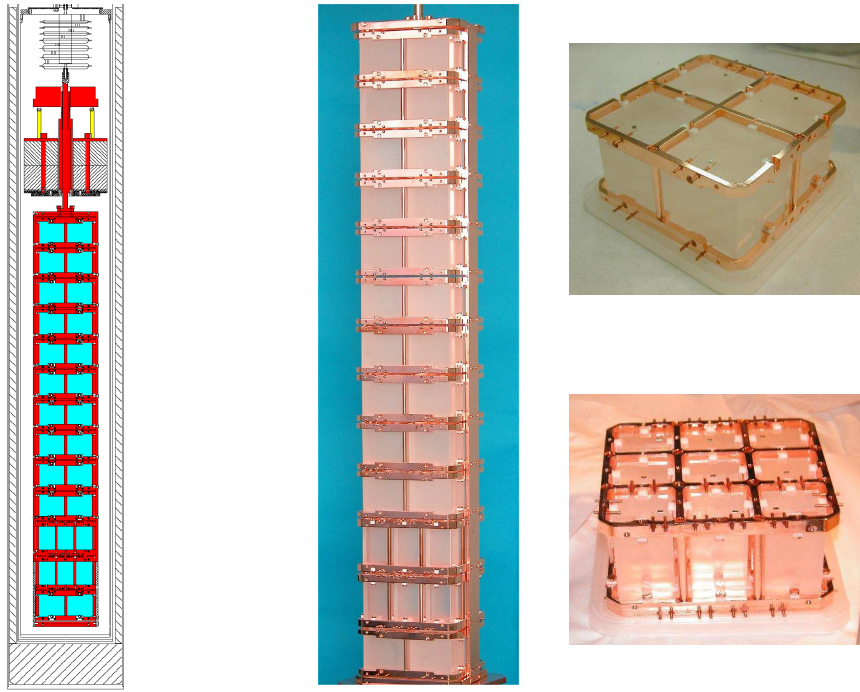
Figure 3.5: *The CUORICINO detector: scheme of the tower and internal roman lead shields (left), the 13 planes tower (centre), the 4 crystal module (top right) and the 9 crystal module (bottom right).*

3.4.3 CUORE

The last design of the CUORE detector consists of an array of 988 TeO_2 $5\times5\times5$ cm^3 bolometers, arranged in a cylindrical configuration of 19 towers of 52 crystals each (Fig. 3.6).

The structure of each four-detector module is shown in Fig. 3.7. The four crystals are held between two copper frames joined by copper columns, as in the MiDBD-II and CUORICINO module. PTFE pieces are inserted between the copper and TeO_2 , as a heat impedance and to clamp the crystals.

The four detectors are mechanically coupled; some of the PTFE blocks and springs act simultaneously on two crystals. The good performances of CUORICINO detectors, having a similar 4 crystal module structure, clearly demonstrate that the CUORE technology is viable.

The CUORICINO detector presently taking data at LNGS consists of one of the 40 detector towers with the exception of the two planes containing the $3\times3\times6$ cm^3 crystals discussed earlier. Each of the 25 CUORE towers will be suspended independently from a large square copper plate, thermally connected to the mixing chamber of a dilution refrigerator (DR). In this manner CUORICINO is actually a test for the CUORE array.

The array will be suspended from the mixing chamber by a vertical spring to decouple the detector from the vibrations of the dilution refrigerator.

3.5   Cryogenic setups

Bolometric detectors, as described in chapter 2, require a low working temperature. For this reason all the performed TeO_2 experiments and the R&D activities needed a cryogenic setup, able to reach temperatures around 10 mK.
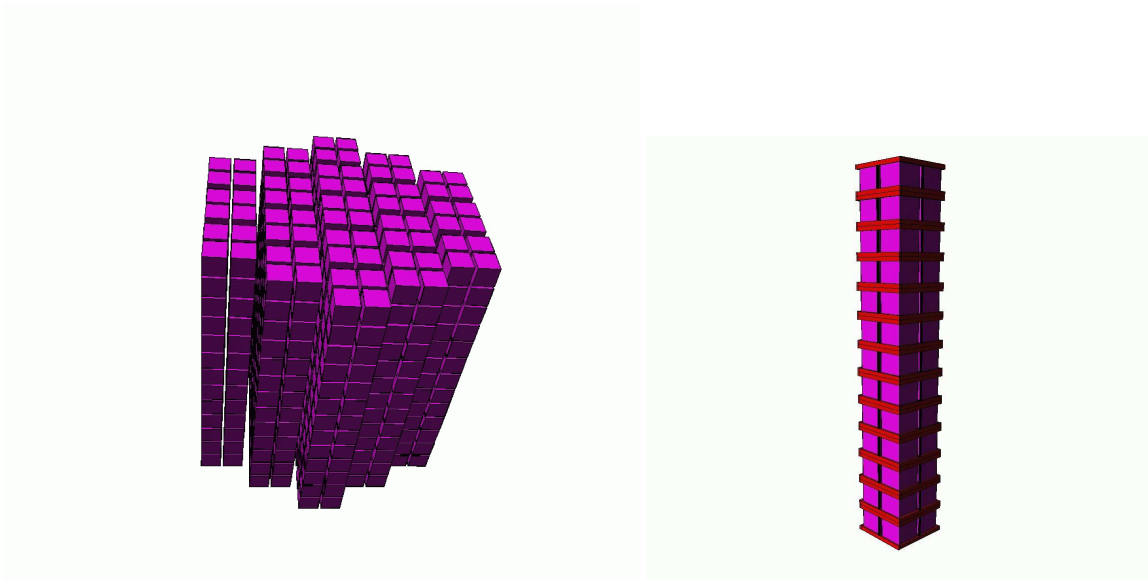
Figure 3.6: *The CUORE detector (left), one of the 25 towers (right).*
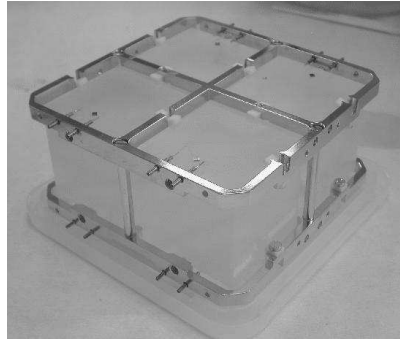
Figure 3.7: *A four detector module.*

Two cryogenic setups were installed in the eighties at LNGS by the Milano group. The first, used in the past for the MiDBD experiment (Hall A) is now hosting the CUORICINO detector. The second (Hall C) has been dedicated to the research and development activities for CUORICINO and CUORE. A completely new cryogenic system will be realized for CUORE in the hall A of LNGS.

3.5.1 MiDBD and CUORICINO

The two existing cryogenic setups consist of dilution refrigerators having powers of 1000 μW (hall A cryostat) and 200 μW at 100 mK (hall C cryostat). They are both equipped with a dedicated Helium liquefier, providing a substantial recovery of the Helium and preventing Helium contamination of the tunnel atmosphere, and are housed inside Faraday cages to suppress electromagnetic interference (see Fig. (3.8)). A much larger experimental volume is available in the Hall A cryogenic setup.

All the materials used for construction of MiDBD and CUORICINO were analyzed to determine their radioactive contamination levels. These measurements were carried out by means of two large Ge detectors installed in the Gran Sasso underground Low Radioactivity Laboratory. The level of the radon contamination in the air of the Laboratory is continuously monitored. Both dilution
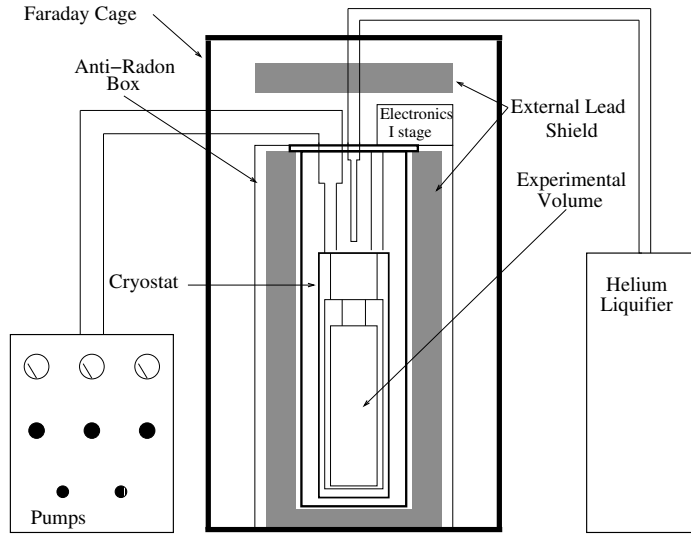
Figure 3.8: *Scheme of the cryogenic setup.*

refrigerators are equipped with heavy shields against environmental radioactivity. In particular, the Hall A dilution refrigerator is shielded with two layers of lead of 10 cm minimum thickness each. The outer layer is of commercial low radioactivity lead, while the internal one is made with special lead with a ^{210}Pb contamination of 16 ± 4 Bq/kg. The external lead shields are surrounded by an air-tight box flushed with fresh nitrogen from a dedicated evaporator to avoid radon contamination of the gas close to the cryostat. In order to shield the detectors against the unavoidable radioactive contamination of some fundamental components of the dilution refrigerator thick layers of Roman lead are placed inside the cryostat just around the detectors. A borated polyethylene neutron shield (10 cm) was added in 2001 to the hall A cryostat.

3.5.2 CUORE

The CUORE bolometers will operate at temperatures between 7 and 10 mK. This will require an extremely powerful dilution refrigerator (DR). The CUORE detector will be cooled by a He^3/He^4 refrigerator with a cooling power of 3 mW at 120 mK. Refrigerators with the required characteristics are technically feasible. One example is the DRS-3000 DR model constructed by the Kamerling Onnes Laboratory in Leiden. The unit is shown in Fig. 3.9, inserted in the dewar. One important design feature is the 50 mm diameter clear access to the mixing chamber to allow a rod, suspended from an external structure, to suspend the detector array to minimize vibrations from direct connection to the mixing chamber. The temperature of the rod will be controlled in stages along its length by flexible thermal contacts to avoid vibrations.

The dewar housing the DR will have a jacket of liquid nitrogen (LN) to avoid the need of superinsulation which is not free of radioactivity. Liquefiers will provide constant liquid levels for the two baths over long periods of operation. Besides housing the CUORE detector, the dewar will be able to support an effective system of roman lead shields maintained at the low temperature close to the detectors (Fig.3.9).
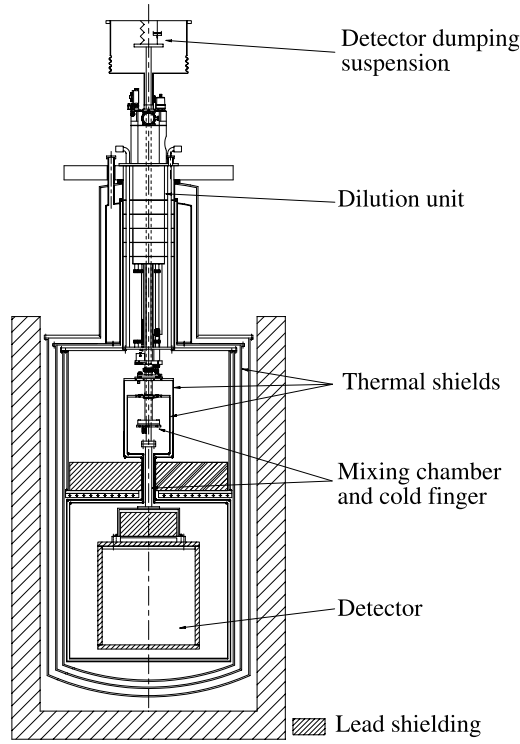
Figure 3.9: *CUORE cryostat and shielding.*

Shielding requirements

Double-beta decay experiments, as well as dark matter searches and searches for rare events in general, require deep underground locations and ultra low radioactive environments. This latter requirement is usually accomplished by placing severe constraints on the selection of the materials used and by the realization of proper shielding surrounding the detectors. When complicated structures like dilution refrigerators are used, the problem of their shielding and construction using only low radioactive contamination materials is complex. Moreover, since in MiDBD and CUORICINO a non negligible contribution to the background rate in the $\beta\beta(0\nu)$ region was recognized as originating from environmental radioactivity, and radioactive contaminations of the cryostat structure , the design of effective shields (specially those directly surrounding the detector) is crucial to reach the sensitivity goal of CUORE.

Part of the bulk lead shielding will be placed inside of the cryostat, and part outside (Fig. 3.9). This will shield the detector from environmental radioactivity and from radioactive contaminations of the dewar structure, also reducing the total amount of lead required. A 4π layer of ultra-low background lead will constitute 3 cm thick walls of the cubic structure of the array. This layer will be Roman lead whose ^{210}Pb activity was measured to be less than 4 mBq/kg [80]. As for CUORICINO, the dilution refrigerator will be constructed from materials specially selected for low levels of radioactivity . Nevertheless, these levels might be higher than can be tolerated by the sensitivity requirements. The main goal of the inner lead shield will be therefore of cancelling their dangerous contributions to the CUORE background level.

The top of the detector array will be protected by two Pb layers of $\sim$1 m diameter and 10 cm thickness each, with a 10 cm diameter central bore to accommodate the copper cold finger that supports the detector and the narrow neck of two radiation shields of the refrigerator that are at temperatures of 50 mK and 600 mK. The layer close to the detector will be made of high quality
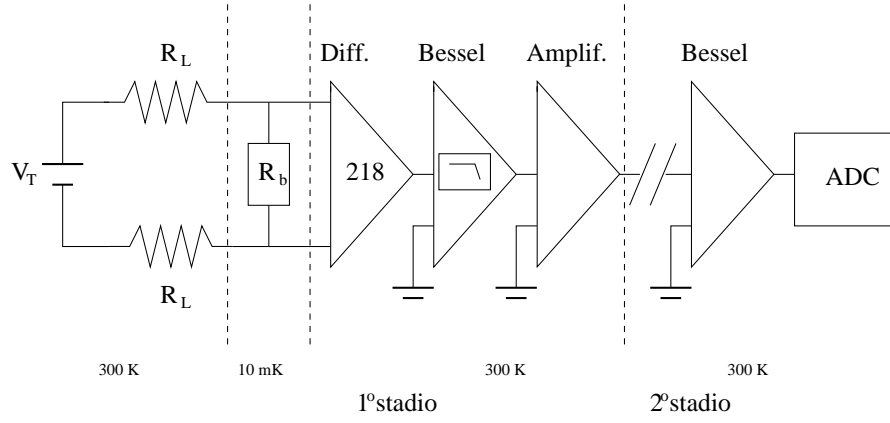
Figure 3.10: *Scheme of the electrical read-out set-up.*

lead with an activity of 16 Bq/kg of ^{210}Pb. The upper layer will be made of modern lead with an activity of ^{210}Pb of 150 Bq/kg. Another layer of lead, 17 cm thick, and with a dimaeter of $\sim$40 cm will be placed directly on the top face of the detector. It will be constructed from low activity lead of 16 Bq/kg of ^{210}Pb. This configuration is designed so that the minimum path to the detector from the IVC and the dilution unit is 20 cm of lead. Finally, outside the dewar, there will be two 10 cm thicknesses of lead, 16 Bq/kg of ^{210}Pb for the inner layer, and 150 Bq/kg for the outer layer. The lead shield will be surrounded with a 10 cm thick box of borated polyethylene that will also function as an hermetically sealed enclosure to exclude radon. It will be flushed constantly with dry nitrogen.

The entire dewar, detector, and shield will be enclosed in a Faraday cage to exclude electromagnetic disturbances that also constitute a source of background, albeit at low energies, important to dark matter and solar axion searches. The addition of a muon veto surrounding the entire structure will be also considered.

3.6   Electronics and DAQ

The electrical read-out configuration of a bolometric system is shown in Fig. (3.10). The main stages of the system are:

- **Detector biasing:** the thermistor is symmetrically polarized by means of 2 load resistors R_L. In this way a differential signal is read, thus avoiding common noise. The value of R_L must be greater than the thermistor impedance at the working temperature in order to have constant current bias and high signals. At $T \simeq 10\ mK$ the thermistors behave like a resistance of the order of 1÷100 MΩ; the load resistors are then chosen with values of the order of GΩ. The Johnson noise for these high resistance values is no longer negligible and has an rms value of about 300 eV for load resistors working at 300 K.

- **First differential stage:** it consists of a first differential preamplifier with gain G = 218 (which contributes to the reduction of the common noise), an antialising bessel filter (that cuts frequencies above 12 Hz) and a programmable gain stage. This first stage can operate at room temperature, as in Fig.((3.10)), or cooled down to 120 K. The cold electronics has the purpose of reducing the series and parallel preamplifier noise, which in fact decreases with temperature, and on the other hand, to reduce microphonic noise, a noise source quite important for low energy signals, as for instance for Dark Matter searches.

- **Second stage:** an additional amplifier stage is set before the signal is transmitted to the ADC.

After the second stage the signal is sent simultaneously to the Analog to Digital Converter (ADC) and to the trigger that commands the ADC. If the pulse amplitude is higher than the trigger threshold (that is indipendently set for each detector) the signal is digitalized and transmitted to a PC-VXI that works as a memory of the system and makes a pre-analysis, thus permitting to check real time the measure state. The ADC parameters depend on the pulse characteristic, but usually a voltage range of 0 - 10 V and 16 bits are used, thus meaning a resolution in the amplitude sampling of 0.15 mV. In Mi-DBD the sample time was 2 ms with a total number of pulses of 1024, while for CUORICINO the signal is sampled every 8 sec for a 512 total samplings.

3.6.1 Extrinsic noise

In sections (2.4.2) we have introduced the noise sources due to the intrinsic properties of bolometric detectors. The electronic read-out, as it has been just described, introduces sources of extrinsic noise:

- **Johnson noise:** as previously said, for $G\Omega$ load resistors this noise source has a value around 300 eV, not negligible for experimental resolutions in the range $1\div8$ keV FWHM. This source of noise can be reduced working with load resistors at low temperature, since the noise power spectrum is proportional to the temperature.

- **Preamplifier noise:** The noise associated to the preamplifier stage is of three types: *series* due to the JFET resistance having a value around 9 eV, *series 1/f* that amounts to 15 eV, and the *parallel shot noise*, that for a room working temperature is around 130 eV rms. The usual experimental resolutions for energies close to the DBD0ν signal energy is of $\sim$7keV FWHM, thus meaning that these noise sources doesn't affect so much the actual value. At low energy, where the resolution is of the order of 1 keV FWHM they are no longer negligible.

- **Microphonic noise:** it is due to the variation of the static electric charge of the read-out wires and can be reduced working with a low temperature first differential stage, which allows shorter wires. It contributes with high frequency components and can worsen the low energy threshold.

Other sources of extrinsic noise can rise from electromagnetic radiation, leading to spike signals and fast variations of the detector working point.

The most dangerous source of noise is due to thermodinamic fluctuations of the system and to heat powers rising from mechanical vibrations. These sources have low frequencies that can be partially corrected via a hardware stabilization system (introduced in the second run of CUORICINO) and an off-line stabilization procedure.

3.7 Off-line analysis

The main goal of the off-line analysis is the extraction of the relevant physics informations from the large amount of raw data recorded by the DAQ system. This task includes both the raw detector pulse analysis (e.g. amplitude evaluation, noise rejection, gain instability and linearity correction) aiming at producing reliable n-ple's (a proper number of parameters fully describing each bolometric pulse) and energy spectra, and the following multi-dimensional analysis aiming at obtaining the sought physics results (e.g. $\beta\beta(0\nu)$ or DM interactions). The identification of the various background sources is also an important goal of the second-level analysis, and is the main topic of this PHD

thesis work. This chapter will be devoted to the first level analysis, leaving for chapter 5 a detailed description of the second level analysis.

3.7.1 First-level analysis

As described in a previous section, when the output voltage of a given detector exceeds the trigger threshold, the acquisition system records a number of converted signal samples. The acquired time window (~few sec) must fully contain the pulse development in order to allow an accurate description of its waveform. The existence of a pre-trigger interval just prior to the production of the pulse ("baseline") guarantees that a small fraction of the number of acquired samples can be used to measure the DC level of the detector (which is directly connected to the detector temperature).

The fact that for each triggered pulse an entire waveform is sampled and recorded gives a lot of useful informations, as it will be shown in this section.

The following are important goals for the (first-level or *pulse*) analysis (FLA):

1. maximization of the signal to noise ratio for the best estimate of the pulse amplitude. This is accomplished by means of the optimum filter (OF) technique [88];

2. correction of the effects of system instabilities that change the response function of the detectors (gain "stabilization");

3. rejection of the spurious triggered pulses by means of pulse shape analysis;

4. identification and rejection of radioactive background pulses by means of coincidence analysis.

The Optimum filter

The OF technique is frequently used with bolometers to evaluate the amplitude of a signal with a superimposed stochastic noise. This algorithm has proven to provide the best estimate of the pulse amplitude under general conditions. Relative to a simple *maximum–minimum* algorithm, this technique allows the evaluation of the signal amplitude with much higher efficiency resulting in an effective improvement of the detector energy resolution. The following information is needed to implement the OF technique: the detector response function (i.e. the shape of the expected signal in a zero noise condition) $S(\omega)$ and the noise power spectrum $N(\omega)$. Once these are known, the OF transfer function is easily obtained and used as a digital filter for the acquired pulses. The role of the OF transfer function is to weight the frequency components of the signal in order to suppress those frequencies that are highly influenced by noise and has the expression:

$$H(\omega) \;=\; K \frac{S^*(\omega)}{N(\omega)} e^{-i\omega t_M} \tag{3.5}$$

where K is an arbitrary constant and t_M the time at which the filtered signal is maximum. The amplitude of the pulse is then evaluated by integrating eq. (3.5) or evaluating the amplitude of optimally filtered pulses in the time domain. filtered pulses.

The noise power spectrum $N(\omega)$ is usually obtained from a hundred of baseline signals randomly acquired before every measurement by averaging the square module of their discrete Fourier transforms. The shape of of the detector response function is evaluated by averaging over a large number of acquired pulses, accurately selected as to reject spurious signals.
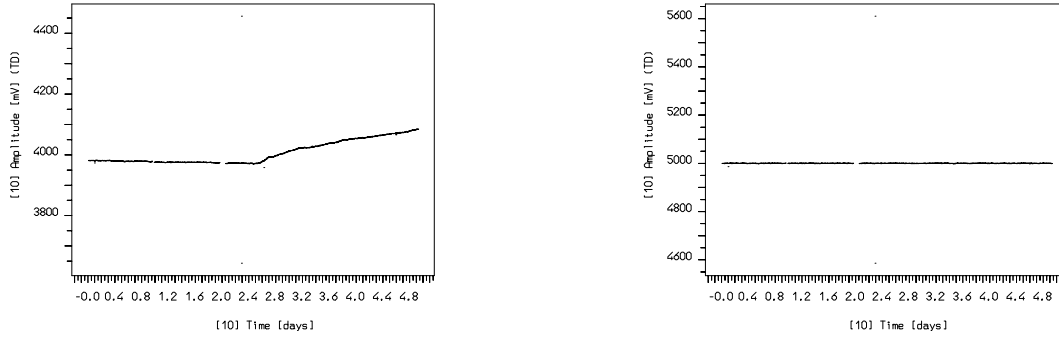
Figure 3.11: *Heater amplitude vs baseline before (a) and after (b) the stabilization procedure.*

The nuple construction

In processing the data off-line, the following parameters are evaluated and recorded to disk for each digitized pulse (*n-ple*):

1. the *channel number* i.e., the number of ADC channel that exceeded the trigger threshold;

2. the *absolute time* at which the pulse occurred with a precision of 0.1 msec;

3. the *OF amplitude* i.e. the amplitude of the optimally filtered signals

4. the *baseline*, obtained by averaging a proper number of samples from the pre-trigger interval. Since the detectors are DC coupled, it provides a direct measurement of the detector temperature at the creation of the signal;

5. the signal *rise* and *decay times*;

6. the *pulse shape parameters*, obtained by comparing the acquired pulse with the expected response function of the bolometer after OF or adaptive filters. A further powerful technique is based on the use of artificial neural networks (ANN);

7. the *pile-up fraction*. The Wiener-filter algorithm is implemented [89] in order to recognize and successively reject double events. When two signals are found to occur in the same acquisition temporal window their amplitudes and their temporal distance are evaluated. These two parameters are very important in order to study the coincidence events due to radioactive cascades.

Instability correction

The next First Level Analysis step is the gain instability correction. The OF amplitudes are corrected to reduce or cancel the effects of system instabilities responsible for the variation of the ratio between the energy E deposited into a given crystal and the amplitude Δ V of the corresponding electrical pulse. These variations induce a worsening of the detector energy resolutions since signals referring to the same energy released in the crystal lead to different detector responses, thus broadening the correspondent peak in the energy spectrum.
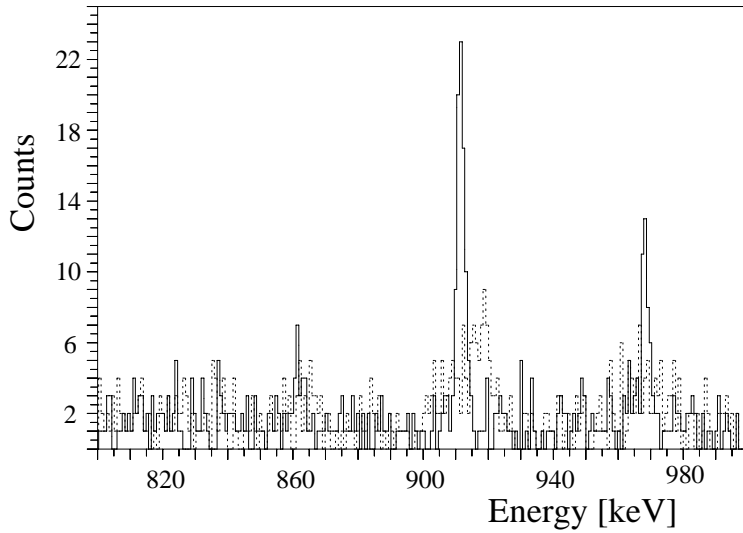
Figure 3.12: *Comparison between a calibration spectrum before (dashed line) and after (continuous line) the stabilizzation procedure.*

According to equation (2.12) of our very naive detector model there are three instabilities that can modify the ratio Δ V/E (where V=V$_b$*G is the output voltage given by the product of the bolometer voltage V$_b$ and the electronics gain G):

- a variation in the electronic gain G;

- a variation in the bias V$_{Tot}$;

- a variation in the temperature T$_b$ of the crystal.

The electronic system is designed to guarantee a stability of G and V$_{Tot}$ within 0.1% . It is however, much more difficult to maintain stability within 0.1% of the detector temperature on long time scales. At a temperature of 10 mK this would require maintaining the temperature of all the crystals to an accuracy of 2 μ K for a period of several days. Usually thermal instabilities are correlated with intrinsic instabilities of the cryogenic set-up, mainly due to variations of liquid bath levels that determine small changes in the flow rate of the $^3He - ^4He$ mixture in the refrigerator. The problem can be minimized by directly stabilizing the main cryogenic parameters as much as possible, but often this is a difficult task and not completely solving the problem.

To overcome this problem, and as already mentioned in previous sections, a silicon resistor glued to each crystal is used as a heater to produce a reference pulse in the detector. It is connected to a high precision programmable pulser that produces a fast voltage pulse every few minutes dissipating the same amount of energy (E$_{ref}$) into the crystal each time. These voltage pulses mimic pulses produced in the crystal by particle interactions and are used to measure the value of the ratio Δ V/E. Any variation of the amplitude of the reference pulse is due to variations of the ΔV/E ratio. The OF amplitude of the reference pulse is therefore used to measure, every few minutes, the actual value of Δ V/E while the baseline of the reference pulse provides the contemporary measurement of the value of T. A fit is then used to obtain the values of Δ V/E as a function of temperature. Therefore, in this step of the off-line analysis, the OF amplitude of each pulse is corrected according to the given value of Δ V/E(T[t]) for the detector temperature at which the pulse has been generated. The effectiveness of this technique has been proven in the MiDBD experiment, where a typical temperature fluctuation

over a day ranged from a few tenths to ~100 μK . After correction, these fluctuations were reduced to less than 1 μ K [78] (see Fig. (3.11) and Fig. (3.12)).

Noise rejection

Pulse shape analysis is very useful in rejecting spurious signals produced by microphonics and electronic noise. A confidence level is determined for each pulse shape parameter and for the rise and decay time of each pulse. Signals falling within these intervals are defined as "true" (or physical) pulses, while signals having one or more of their parameters outside of the relevant interval are rejected as noise. While the efficiency in the identification of true pulses is equal to one, not all the spurious pulses are rejected by the use of one pulse shape parameter. The use of more than one pulse shape parameter results in better reliability of the rejection technique.

Linearization

The linearization of the detector response is critically important for energy calibration. The final step in data processing is the conversion of the OF amplitudes into energy values. The naive bolometer model previously used assumes linearity; however, several parameters depend on the crystal temperature, rendering the corresponding equation non-linear. Accordingly, the relation between Δ V and E is periodically obtained by the use of radioactive calibration sources (two simmetric point-like sources of ^{238}U and ^{232}Th in MiDBD and two wire sources of ^{232}Th in CUORICINO). Couples of points $(\Delta V, E)$ are than measured for several gamma lines. The obtained data must then be fit, by means of a minimization procedure, to the thermal model previously described, but taking into consideration the fact that the bolometer resistance and the crystal heat capacity are temperature dependent. This will provide the calibration function of E as a function of ΔV, that will then be used to convert the OF amplitudes into energy values. An alternative fit procedure is based on a polynomial or a power law fit. The latter was found to give the best results in CUORICINO.

A problem we are always facing in linearizing the detector response concerns the alpha region calibration. The use of ^{238}U and ^{232}Th sources in fact limits the calibration points to values lower than 2615 keV line of ^{208}Tl . The extrapolation to higher energies doesn't give optimal linearization for the alpha lines observed in the background measurements. This implies further manipulation of the collected background spectra in order to calibrate the alpha region by means of the alpha lines due to natural radioactivity.

In the second RUN of CUORICINO a new ^{56}Co calibration source was introduced, in order to have gamma lines up to 3.4 MeV.

Multiple events analysis

The analysis of the multiplicity of the events permits both to reject events that left energy in more than one single crystal (they should be very inlikely DBD0ν events) and to study the background sources as it will be described in more details in chapter 5.

Events depositing their energy in more than one crystal can be usually ascribed to high energy gamma rays, whose probability of escaping the rest of the array after the first interaction is small. These high energy photons can derive from environmental radioactivity or from contaminations within the structure of the array. Also high and intermediate energy neutrons have a significant probability of depositing energy in more than one crystal. Another source of multiple events can be surface contaminations of the crystals and of the materials directly facing the detectors. Alpha

particles emitted near the material surfaces have in fact a not negligible probability of escaping and they can consequently hint a nearby detector.

In the final stage of off-line analysis these coincidence events can be identified by analysing the various registered pulse parameters, as detector number, signal time, pulse energy, and pile-up parameters. Signals occurring almost at the same time in two or more faced detectors are in fact evaluated as coincident. By analyzing the energy released in the detectors and the number and position of the hinted crystals is possible to try to find out the source that originated such events.

While in MiDBD and CUORICINO only a little fraction of the detector surfaces are faced to other crystals, thus limiting the efficiency of the anticoincidence cut, the tightly closed structure of CUORE will guarantee a stronger reduction of the background.

Chapter 4

Radioactivity sources for TeO$_2$ bolometric experiments

Introduction

As it can be seen from eq. (1.57) the sensitivity of a DBD experiment can be strongly limited by the background counting rate in the region of interest. In fact in such experiments, spurious counts due to environmental radioactivity, cosmic rays, neutrons, airborne activity (Rn) and intrinsic contamination of the detector and of the experimental parts, can obscure the signal counts of interest. Background reduction is therefore a fundamental task to face when performing a low counting rate experiment, as the DBD experiments.

The background sources that need to be taken into account can be divided two main components:

- **External sources:** a not negligible contribution to the background can arise from interactions due to particles originating from outside the detector set-up, such as photons and neutrons from the Gran Sasso rock or muons and muon induced particles. Photons originate from natural radioactivity of the rock, mainly consisting of ^{238}U , ^{232}Th and ^{40}K , while muons have mainly a cosmogenic origin. Neutrons can both have a cosmogenic origin or be produced by (α,n) reactions occurring in the Gran Sasso rock. The flux of cosmogenic muons and neutrons is strongly reduced by the natural shielding provided by the 1500 m of dolomitic rock (3500 mwe) of the Gran Sasso mountain.

- **Internal sources:** another important source of background arises from intrinsic radioactive contaminations of the materials used to build up the experimental setup. The omnipresence of primordial radionuclides in ores and other raw materials results in a wide range of contamination in the final product. With just few exceptions, the main radioimpurities are usually ^{40}K , ^{232}Th and ^{238}U . The cosmogenic activation, produced by cosmic rays in the detector materials above ground (during fabrication and transportation), is also a non negligible source of internal background. Another unavoidable background source we cannot neglect in performing our DBD experiments with TeO$_2$ detectors is the DBD2ν of the ^{130}Te occuring in the crystals bulk.

In this chapter the main sources of background affecting the sensitivity of a bolometric experiment such as MiDBD, CUORICINO and the future CUORE will be illustrated.

4.1 External background

The Gran Sasso rock constitutes at the same time a fundamental shielding for Cosmic Radiation (CR) and a source of natural radioactivity.

4.1.1 Cosmic Rays

Primary cosmic ray particles (about 87% protons, 11% alpha particles, 1% heavier nuclei with $4 < Z < 26$, 1% high energy electrons, neutrons and neutrinos) hit the earth atmosphere at a rate of about $1000 \ m^{-2}s^{-1}$ [90]. Their interaction with atmospheric atoms generates a large variety of elementary particles, called secondary cosmic rays. These particles are mainly neutrons, electrons, neutrinos, protons, muons, and pions. The total intensity of these secondaries reaches a maximum at about 13.7 km altitude and then falls off gradually with the strongest decline for the nucleons. At the sea level the relative intensity of charged pions : protons : electrons : neutrons : muons is about 1 : 13 : 240 : 480 : 1420 with $1.34 \cdot 10^{-5} cm^{-2}s^{-1}$ for charged pions [91, 92].

While electrons and protons are stopped by the Gran Sasso mountain shield, muons and neutrons fluxes are only attenuated. High energy neutrons are thermalized by a mean lenght of about 200 $g \cdot cm^{-2}$ [93], mainly via inelastic scattering. Muons, on the other hand, loose their energy in standard rock on a much longer scale (about 2 $kg \cdot cm^{-2}$ near sea level) by ionization, pair production, bremsstralung and nuclear interactions [94]. The interaction of muons with the rock and with the detector shields can produce tertiary neutrons via fission processes, (α,n) reactions and negative muon capture. Photonuclear reactions and photo fission of real and virtual photons associated with fast muons in high Z materials can also lead to neutron production. The depth of the LNGS (3500 mwe) reduces the muon flux down to $\sim 2 \times 10^{-8} cm^{-2}s^{-1}$ with a mean energy of $\overline{E}_\mu = 200 GeV$ [95]. In the case of external neutrons (from the rocks, from fission processes, from (α,n) reactions from ^{238}U and ^{232}Th contaminations of the rock itself, as well as neutrons originated by muons in the walls of the underground site), the environmental neutron flux has been measured in LNGS. The result is of $\sim 1 \times 10^{-6}$ cm^{-2}s^{-1} for the thermal component, $\sim 2 \times 10^{-6}$ cm^{-2}s^{-1} for the epithermal and $\sim 2 \times 10^{-7}$ cm^{-2}s^{-1} for energies over 2.5 MeV ([96]) . They are fairly well moderated by the polyethylene and eventually absorbed or captured.

4.1.2 Environmental radioactivity

Radionuclides in our environment are of three general types:

- *primordial:* originated from the nucleosynthesis. Primordial radioisotopes have lifetimes as long as the earth's life ($4.5 \times 10^9 y$) and can belong to the natural decay chains of ^{238}U , ^{232}Th (see Fig. (4.1) and Fig. (4.2)) and ^{235}U or be single isotopes as ^{40}K and ^{87}Rb.

- *cosmogenic:* this radioactivity source is induced by the interaction of the CR with terrestrial atmosphere and matter. Examples of cosmogenic isotopes are ^{3}H and ^{14}C.

- *antropogenic:* originated from man nuclear activities.

Of all the known isotopes only a few are stable and can be plotted as A (mass number) vs. Z (number of protons) as shown in Fig. (4.3). All the unstable isotopes go through nuclear decays in order to reach a more stable configuration. There are three main decay channels: alpha, beta and gamma decay.
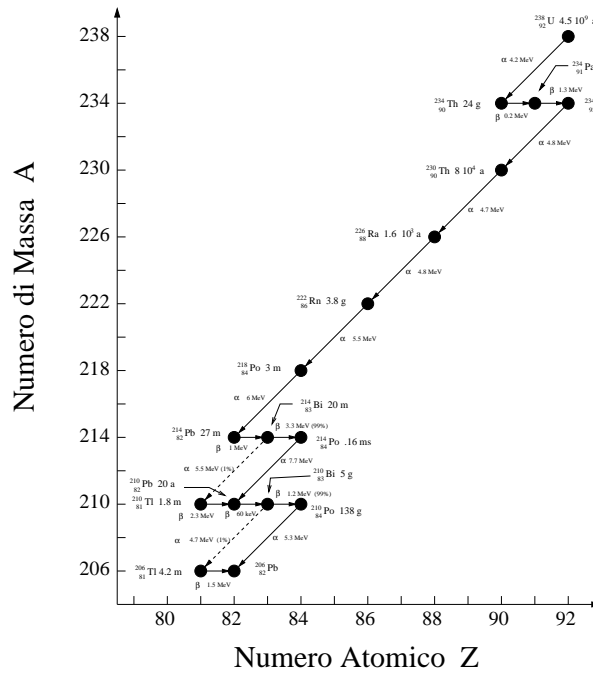
Figure 4.1: ^{238}U chain.

Alpha decay

Many heavy nuclei are energetically unstable against the spontaneous emission of an alpha particle:

$$(A, Z) \rightarrow (A - 4, Z - 2) + \alpha \tag{4.1}$$

The alpha particles appear in one or more energy groups which are monoenergetic. For each distinct transition between initial and final nucleus a fixed energy difference or Q-value characterizes the decay. This energy is shared between the alpha particle and the nuclear recoil in a unique way, so that each alpha particle appears with the same energy given approximatively by $Q(A - 4)/A$. Most alpha particle energies are in the range 4 and 6 MeV.

Alpha particles and the corresponding nuclear recoils loose energy rapidly in materials and stop in few microns. If the decaying nucleus is on a very thin layer near the surface of the material, the alpha particle (or the corresponding nuclear recoil) can be emitted from the surface and hit a faced material, with a continuum energy spectrum that extends down to low energies. For this reason surface contaminations of the materials facing a bolometric detector can be a very dangerous source of background.

Beta decay

The beta decay can be of two different types depending on the position of the unstable nucleus with respect to the stability plot (Fig. (4.3))

β^- **decay** A nucleus laying above the curve of Fig. (4.3) likely decays transforming a neutron in a proton and consequently emitting an electron and an antineutrino:

$$(A, Z) \rightarrow (A, Z + 1) + e^- + \bar{\nu}_e \tag{4.2}$$

49
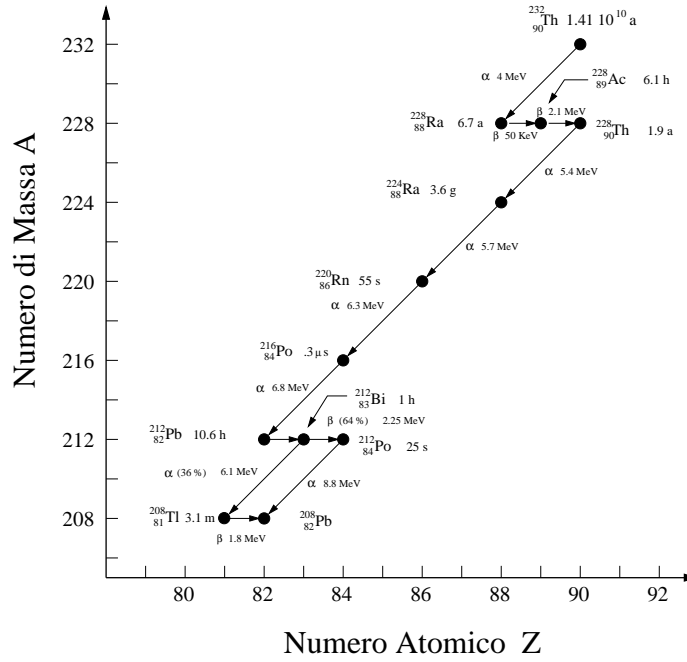
Figure 4.2: ^{232}Th chain.

The Q-value of the reaction, correspondent to the mass difference between the parent and the daughter atoms, is converted in neutrino and electron kinetic energy. The electron energy spectrum corresponds therefore to a continuous plot, that can vary from zero to the Q-value. Since the end-point corresponds to the Q-value but the neutrino mass, the meaasurement of beta decays can give informations about the neutrino mass (see chapter 1).

β^+ **decay** A nucleus laying below the curve of Fig. (4.3) likely decays transforming a proton in a neutron and consequently emitting an positron and a neutrino:

$$(A, Z) \to (A, Z - 1) + e^+ + \nu_e \tag{4.3}$$

The emitted positrons usually lose their energy very rapidly in the material and at the end of their path recombine with an electron then giving rise to a couple of 511 keV photons, emitted in opposite directions.

Electron capture A nucleus with a proton excess can reach the stability capturing an electron from an internal shell, thus converting a proton in a neutron:

$$(A, Z) + e^- \to (A, Z - 1) + \bar{\nu}_e \tag{4.4}$$

All of the energy is practically carried out by the neutrino.

Gamma decay

Gamma radiation is emitted by excited nuclei in their transition to lower-lying nuclear levels. This can happen for instance when beta or alpha decays occur on excited states of a nucleus:

$$(A, Z)^* \to (A, Z) + \gamma \tag{4.5}$$

50
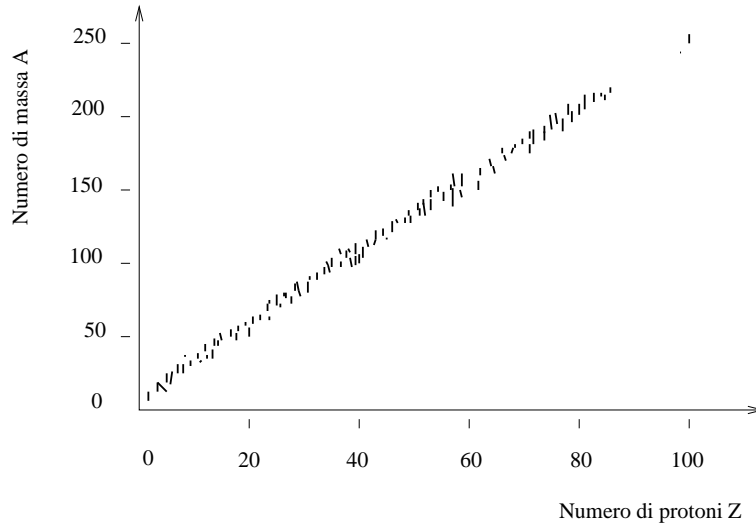
Figure 4.3: *Plot of the stable isotopes*

The energy of the generated photons varies in the range 50 keV ÷ 3 MeV, the maximum energy associated to a natural gamma ray being 2615 keV for the ^{208}Tl decay. There exists also higher energy gamma emissions, as for instance the line at 3.2 MeV for ^{214}Bi, but their branching ratio is negligible. While the beta decay is a relatively slow process, nuclear disexcitations occur with times of the order of psec. Therefore gamma rays are characterized by the lifetime of the parent nucleus and by the level structure of the daughter. Nuclear states have very precise energies (i.e. their intrinsic width is very small) therefore gamma rays are monoenergetic particles, with a spectral line very narrow as respect to the usual experimental resolution.

Nuclear excited states can decay to the ground state also via the emission of an electron, likely from the K shell. The vacancy created by the emission of this internal electron is then filled by external electrons with a consequent emission of X rays or Auger electrons.

The field of gamma radiation against which we have to shield our detectors is almost exclusively constituted by photons from the uranium and thorium series and ^{40}K decay. The measured components of the gamma ray flux from natural radioactivity in the LNGS laboratory [95] are presented in Tab. (4.1)

Isotope	Energy [keV]	Flux [$m^{-2}d^{-1}$]
^{40}K	1460	3.8×10^7
^{214}Pb	295.2	0.8×10^7
^{214}Pb	352	1.8×10^7
^{214}Bi	609.3	2.9×10^7
^{214}Bi	1120.3	1.4×10^7
^{214}Bi	1764.5	1.7×10^7
^{208}Tl	2614.5	1.35×10^7

Table 4.1: *Measured gamma ray flux in the LNGS [95]*

These radioactivity levels, measured in the LNGS environment, derive from the natural activity of the rocks and of the concrete, that is estimated to be:

$$\leq 5.1 \text{ Bq·kg}^{-1} \quad \text{for } ^{40}\text{K}$$
$$\leq 0.25 \text{ Bq·kg}^{-1} \quad \text{for } ^{214}\text{Bi}$$
$$\leq 5.1 \text{ Bq·kg}^{-1} \quad \text{for } ^{238}\text{U}$$

Secular equilibrium in the decay series (activity of all the daughter nuclides equal to the activity of the chain parent) is rarely met in most surface and near surface geological environments, since nuclides of the chain are subject to migration due to either physical or chemical processes [97]. In particular radon, an inert gas that is an intermediate member of all three decay series, may escape from the rock and diffuse in the interstitial air or in the underground water. Its longer living progeny ^{210}Pb is readily attached to aerosols and finally deposited on the surface by washout and by dry deposition. Surface ^{210}Pb contaminations, accumulated over relatively long periods, may disturb experiments sensitive to alpha particles, as thermal detectors. For this reason all the mounting procedures of MiDBD and CUORICICINO detectors have been performed in clean rooms and the detectors have always been kept in a nitrogen flushed atmosphere. The presence of radon in the experimental environment must be avoided also for the gamma rays originated by its progenies decays. The last gamma active nucleus for ^{222}Rn chain is ^{214}Bi (neglecting the 0.107% abundance of the 803.3 keV line of ^{206}Pb). The gamma activity of the radon family dies consequently out with a half life of 26.8 min (^{214}Pb). The best protection of a detection system against radon consists thus in maintaining the experimental setup in a small overpressure of a radioclean gas (i.e. Na) environment. In the Gran Sasso underground Laboratory the measured radon activity is of about 30 Bq/m^3 [98]. MiDBD and CUORICINO are therefore hosted in a plexiglass box, where evaporated nitrogen is fluxed to avoid the influx of radon.

4.2   Internal background

Bolometric experiments, as already underlined, are detectors sensitive in the whole volume and to any kind of energy deposition. This means that both gamma rays and heavy particles (as for instance alphas or nuclear recoils) generate a background signal undistinguishable from the searched electron signal of the DBD0ν decay. The materials used to build up a DBD experiment must therefore be severely checked for their contamination levels. The radioactivity arising from them is in fact a dangerous source of background, limiting in an unrecoverable way the sensitivity of the experiment.

In this section we are going to illustrate the main background sources for the experiments with TeO$_2$ bolometers performed by the Milano group, and on which this thesis work has been developed. The possible radioactive sources have to be looked for in the various components of the setup described in chapter 3.

Lead shields   A very limited number of materials are suited for the reduction of environmental gamma rays. Ideally, the material should have high atomic number and low intrinsic activity. Lead is a good shielding material, due to its high atomic number and reasonable cost and mechanical properties. Further advantages are: low neutron cross section and a favorable low interaction probability with cosmic rays, including the production of radionuclides by activation. Unfortunately its intrinsic radioactivity is mostly not negligible.

The nature and origin of lead contaminations has been studied by many authors [99] [103]. The consistent overall result is that only ^{210}Pb with its daughter nuclides ^{210}Bi and ^{210}Po is responsible for the intrinsic radioactivity of lead. The very soft beta (16.5 and 63 keV) and gamma (46.5 keV) radiation of ^{210}Pb hardly escapes self absorption, but energetic beta rays of ^{210}Bi induced bremsstrahlung can give rise to a continuum up to 1.16 MeV.

	^{238}U	^{226}Ra	^{214}Bi	^{232}Th	^{228}Ac	^{208}Tl	^{40}K
Au wires	<0.99	<1.58	<.34	<0.33	<.29	<.37	1.3±0.2
Cu screws	<18.4	<11.0	<7.3	<13.6	<14.0	<14.0	18.3
TeO$_2$	11.5±1.7	30.5±4.6	1.7±0.2	3.4±0.5	2.4±0.36	1.7±0.2	6.6±0.9
tin	42.3±6.1	45.1±6.2	39.0±5.8	18.4±2.7	18.4±2.7	18.4±2.7	<65
gold wires	<340	<1580	<340	<290	<290	<370	1300(?)
Epoxy	<8.2	<8.2	<6.8	<2.7	<2.7	<6	<47

Table 4.2: *Radioactive contamination measurements for CUORICINO materials. All values are in mBq/kg.*

Today certified lead with specific ^{210}Pb activities of less than 100 Bq·kg^{-1}, 50 Bq·kg^{-1}and 5 Bq·kg^{-1}is commercially available. An alternative is old lead produced several half-lives of ^{210}Pb ago. An exceptionally large load of antique Roman lead was discovered in 1991 [104]. Its specific activity in ^{210}Pb was measured by the Milano group with a bolometric technique and found to be less than 4 mBq·kg^{-1}[105]. This is the lowest ^{210}Pb contamination in lead ever reported.

Since lead with low ^{210}Pb concentration is normally more expensive, a shell-like construction with decreasing ^{210}Pb content towards the detector would be more economic. As described in chapter 3 the MiDBD and CUORICINO experiments (and also the future CUORE) are provided with two external, 10 cm thick, lead layers, the most external made by commercial lead with and activity of 150 Bq·kg^{-1} and the most internal by a special lead with a contamination in ^{210}Pb of 16 ± 4 Bq·kg^{-1}. Inside the cryostat, roman lead shields with an activity less than 4 mBq·kg^{-1} are placed.

A part from ^{210}Pb and its progenies, no U and Th contaminations have been found so far for commercial lead. The most relevant upper limits measured for ^{226}Ra and ^{208}Tl are 0.25 and 0.29 [106] or 0.33 and 0.67 mBq·kg^{-1} [107]. A ^{40}K contamination of about 0.3 mBq·kg^{-1} was measured by neutron activation analysis in the in commercial Johnson & Matthely lead. For the Roman lead used in MiDBD and CUORICINO limits of 100 μBq·kg^{-1}, 185 μBq·kg^{-1} and 1.3 mBq·kg^{-1} have been measured respectively for ^{232}Th , ^{238}U and ^{40}K contaminations.

Cryostat   The ^{3}He/^{4}He dilution refrigerator is a non negligible source of radioactivity. It is mainly constituted by copper and steel components. The radioactivity arising from the dilution unit parts in MiDBD and CUORICINO is reduced by means of 10 cm of Roman lead placed just above the detector tower. In CUORE the amount of lead shield above the tower will be increased as described in section (3.5.2). The Cu thermal shields surrounding the array are a more dangerous source of radioactivity since the 4π roman lead shield around the detector is thin (1 cm in MiDBD-I and CUORICINO and 3 cm in MiDBD-II and CUORE).

For what concerns Cu, there are indications that very low limits for the bulk contaminations of the U and Th chains can be reached in specially selected productions. This low activity copper, with measured limits of 20μBq/Kg for ^{232}Th and ^{238}U and of 80 μBq/Kg for ^{40}K , was used in CUORICINO for the mounting structure of the detectors. As regards the other copper parts of the CUORICINO setup, as for instance the copper shields, a number of samples have been measured and it was found that the Oxigen Free High Conductivity Cu is definitely better than the standard electrolytic Cu. The measured limits for this copper are around 100 mBq·kg^{-1} for ^{238}U and ^{232}Th and 20 mBq·kg^{-1} for ^{40}K .

Mounting structure   The mounting structure of MiDBD, CUORICINO and CUORE, as described in section (3.4.2) and (3.4.3), consists in copper, PTFE parts and smaller masses as epoxy glue, gold

signal wires, electrical pins, thermistors and heaters.

The radioactive contamination of this components contributes to the measured background both with gamma and alpha interactions. The alpha particles emitted in the decay of a nucleus on the surface of a material faced to the crystals can in fact reach the detector. The energy of the particle will be lost along all the travel from the decay point to the detector and will generate therefore a continuous background that ranges from zero to the alpha total energy. Another important source of radioactivity for the detector components derives from cosmogenic activation. The most dangerous activated isotope is ^{60}Co, whose activity is characterized by a beta decay via the emission of a cascade of two gamma rays with energies of 1173 and 1333 keV respectively. The production of this isotope is particularly dangerous in copper which will have to be stored underground immediately after production. From these considerations it's easy to understand that both bulk and surface contaminations of the materials faced to the detectors must be carefully maintained under control.

The frames hanging the crystals of CUORICINO are made with the low activity copper quoted above, whose measured limits for bulk contamination are of about 20 μBq/kg for ^{238}U and ^{232}Th and 81 μBq/kg for ^{40}K . Direct measurements for the copper surface contaminations are under progress with the ICPMS technique.

Another important material in the detector structure is PTFE. The spacers holding the detector in the right position are made with this material and therefore the radioactive contaminations of PTFE can be very dangerous for the background level of the detector. For organic materials there are two different problems: first it is necessary to have very low levels of intrinsic radioactivity, second it is crucial to control the exposure of these materials to air radioactive pollution (typically Radon). In general the radioactivity of organic compounds like PTFE, Nylon etc can be very low, as demonstrated by the Borexino collaboration [108]. Concerning the diffusion of Radon it is necessary to maintain the selected materials in a very clean environment and, to minimize the possible radioactive contamination present in the volume next to the surface, the external part must be mechanically removed before the realization of the spacers.

The other materials involved in the detector construction are characterized by very small masses. Also in this case however, a good radiopurity level is required in order to avoid any possible dangerous contribution to the background level. In that sense, the selection of the epoxy glue (connection between chips and crystals), of the gold signals wires (electrical connections), of the electrical pins, etc. must be carefully controlled. The indications obtained from our previous tests, show very good levels for epoxies while are non conclusive for gold wires and pins (Tab. 4.2). All these components will be measured again to improve their contamination limits; alternative approaches (e.g. neutron activation) will also be considered.

Crystals   The TeO$_2$ absorbers constitute themself a source of background. In addition to the unavoidable background due to the DBD2ν of ^{130}Te , also volume bulk and surface radioactive contaminations of the crystals must be taken into account. These contamination sources must be known and reduced as possible to avoid dangerous contributions to the measured background.

TeO$_2$ is a molecule composed of only two atomic species: Te and O. The first material to be chosen is obviously Te. The analyzed metallic Te for the CUORICINO production showed limits below the sensitivity of the HPGe detectors installed at LNGS (apart from the well known contamination in ^{210}Pb). TeO$_2$ powders were also measured at the LNGS low activity underground laboratory. Contamination values are reported in Tab. (4.2). The presence of ^{210}Po can be ascribed either to a genuine ^{210}Po contamination or to ^{210}Pb . A critical point is the large quantity of water (few liters per kg) used to "clean" the TeO$_2$ powder just after their production and before the growth procedure. This operation can be of course very dangerous because of the possible presence of radioactive con-

	^{238}U chain				^{232}Th chain			
	^{234}Pa	^{226}Ra	^{214}Pb	^{214}Bi	^{228}Ac	^{212}Pb	^{212}Bi	^{208}Tl
Al_2O_3-I	3.8	24.8	11.7	8.2	6.4	5.2	4.6	3.2
CeO_2	14.3	<4	0.8	0.6	44	82	63	50
Al_2O_3-7μ	<34	11.8		2.2	2.5	2.3		2.3
Al_2O_3-.7μ	<60	14.7		1.6	3.2	1.6		1.7

Table 4.3: *Contamination levels measured for the powders used in MiDBD-I (Al_2O_3-I, CeO_2), in MiDBD-II (Al_2O_3-7μ, Al_2O_3-.7μ) and in CUORICINO (Al_2O_3-7μ) for the crystal surface treatment.*

taminations in the water that can be transferred to the powder. The impact of these contaminations could explain the higher contamination observed in the TeO_2 powders with respect to the starting Te metal. The growing procedure usually reduces the contamination levels of the final crystal with respect to the bare material. However it is usually difficult to quantify the actual reduction in the produced crystals.

The grown crystals must be stored underground as soon as possible, to avoid a long period of exposure to CR. The radionuclei produced by the activation of tellurium are mostly tellurium isotopes (A=121,123,125,127) as well as ^{124}Sb, ^{125}Sb, ^{60}Co and tritium, these last three being of more concern because of their long half-life (^{125}Sb: beta decay of 2.7 years, end-point energy of 767 keV, ^{60}Co: beta decay of 5.27 years end-point energy 2823 keV and ^{3}H: beta decay of 12.3 years, end-point energy of 18 keV).

The last critical point in the preparation of the crystals is the surface treatment made in order to assure a good contact between crystals and semiconductor chips (thermistors and silicon resistances). The crystals used in MiDBD-I, once grown and cut, were polished in two steps: in the first step alumina powder (Al_2O_3) have been used, in the second step the crystals have been polished with CeO_2. Thanks to this second step a better optical quality of the surface is obtained. Samples of powders used by the Shanghai Institute of Ceramics (SICCAS), which has produced the crystals, were requested and analyzed by means of Ge spectroscopy. The obtained results are reported in Tab. (4.3) and show rather large contaminations, that could be responsible of surface contaminations of the crystals.

The data obtained with MiDBD showed that a relevant contribution to the background in the double beta decay region could be identified with the presence of surface contaminations on the crystals. In MiDBD-II the $3\times3\times6$ cm^3 crystals have been therefore treated, in order to remove from the surfaces a thin layer of TeO_2 material. This operation was realized in a clean room at LNGS with powders that were previously tested as having low radioactivity levels. The lapping procedure was divided in two steps: during the first step about 40÷70 μm was removed using 7 μm AlO_2 powders with low contamination levels. During the second step an almost optical finishing of the surface was achieved using a 0.7 μm AlO_2 powder, that showed a radioactive contamination few orders of magnitude lower with respect to the powders used in MiDBD-I (Tab. 4.3).

The crystals used in CUORICINO have been required to the factory after only a first polishing step, performed with a 7 μm specially selected Al_2O_3 powder (Tab. 4.3), that was also used for a second polishing step performed in Como by people of the CUORE collaboration.

Alternative approaches are in principle possible (e.g. surface acid attack, ion beam sputtering, etc.); the careful test of these methodologies and the development of powerful diagnostic techniques will be considered in the early CUORE R&D phase.

Chapter 5

Background analysis method

Introduction

The disentangling of the background sources of a DBD experiment is fundamental to improve its sensitivity. MiDBD was a first and important step from which we begun to systematically study the radioactive contaminations of our setup dangerous for the DBD research. Thanks to sophisticated analysis procedures and with the support of Montecarlo simulations we have developed a powerful method to investigate the radioactive sources responsible of the measured background.

Since that an intense R&D activity both in material selection and surface cleaning procedure optimization has been carried out. A second run of the MiDBD experiment and the following CUORICINO have been built up taking advantage of these results.

The analysis of the new collected background measurements can give us important indications to understand if the in order to make CUORE a competitive experiment in the search of DBD0ν.

A detailed description of the developed analysis method will be given in this chapter.

5.1 Background spectra

In MiDBD and CUORICINO the data are collected by means of short partial measurements (one or two days) that are successively summed and analyzed. Once the first level analysis is performed (see section (3.7)) the stabilized and linearized n-uple can be used to generate single channel spectra and to perform a coincidence analysis. The multiplicity parameter that characterizes every single event (see section 3.7) is in fact very useful to identify the origin of a detected pulse:

- *Events with multiplicity larger than 2* are more likely due to Compton scattering gammas originating from the environmental radioactivity or from the experimental structure contaminations. Also high and intermediate energy neutrons can deposit energy in more than one detector.

- *Doubles* are events that deposit their energy in only two crystals. A fraction of these signals can be originated by gamma rays that stop after the interaction with the second detector or that escape from it and interact with the detector mounting structure. In addition also the fraction of alpha decays occurring on a crystal surface faced to another crystal can give a 2 multiplicity event.

  A typical coincidence plot (scatter plot) is shown in Fig. (5.1). This kind of plot is obtained quoting on one axis the energy released by the detected event in one crystal, and on the other
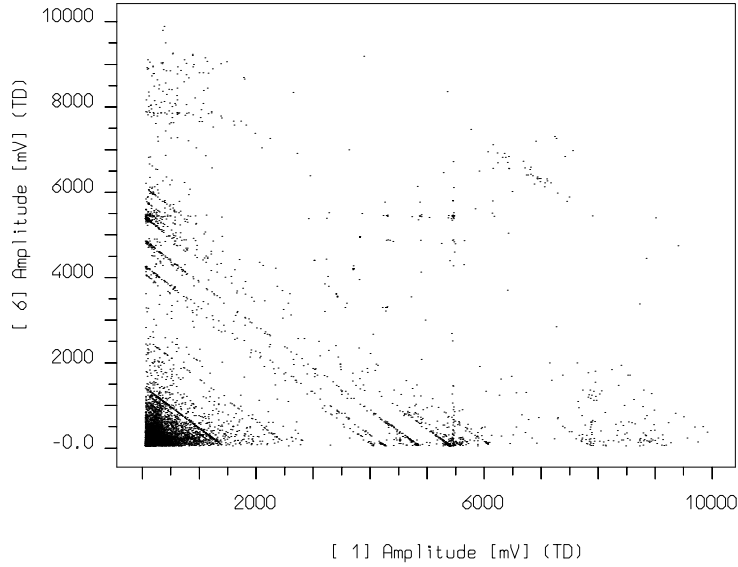
Figure 5.1: *Scatter plot of coincident events between all possible MiDBD detector pairs.*

axis the corresponding energy released in a faced crystal. The selection of all the coincident events detected in all the crystals originates such a plot. Straight lines with a negative slope equal to -1 are clearly visible in this plot, as expected for monochromatic events with multiplicity 2. These lines are easily described by the equation $E_A + E_B = E_{trans.}$.

- *Single site events* correspond to events originated and absorbed by the crystal itself (like a bulk alpha decay or a DBD decay), but can also arise from alpha particles generated by decays occurring on the surface of an inert material, that hints a facing crystal or from alpha decays, occurring on a crystal surface, whose escaping products are absorbed by inert materials. Also gamma rays completely absorbed by a detector or escaping from the detector active mass after one interaction originate anticoincidence events.

The analysis of scatter plots, coincidence and anticoincidence spectra is the first and fundamental step to disentangle the different background sources.

5.2 Montecarlo simulations

Many processes, real physical processes or imaginary ones, can be idealized as a sequence of choices. If it is possible to approximate each choice by some probability function, then one can establish a model which simulate the process. The most common is the Montecarlo method. According to this model many events are generated, each event being the result of a particular sequence of choices. These events are then counted, classified and distributed according to criteria as if they were real events. One can then make comparison with existing real data, or predictions of what should be the outcome of a given real experiment, provided that the established model simulates nature sufficiently well.

In this PHD thesis work the Montecarlo method has been used to generate events of known origin (a chosen radioactive contamination with a chosen localization in the experimental apparatus), in order to study the origin of the background measured in our bolometric experiments, by comparing

these simulated events with the measured data. A code based on the Geant4 package was developed for this purpose.

5.2.1 MonteCarlo method

The type of choice of a variable in the Montecarlo method is a random choice, according to the chosen probability function of that variable. Although the probability function may be modified or parameterized by previous choices, the value of the variable must not be predictable a priori. To satisfy this characteristic the probability interval is compared with a uniform random number distribution. It is assumed that we have available a source variable R which generates random numbers {r}, uniformly distributed over a unit interval, i.e.

$$Pr[R \leq r] = r \quad , \quad 0 \leq r \leq 1. \tag{5.1}$$

We require to generate values {x} of a random variable X with given cumulative distribution F(x), i.e.

$$Pr[X \leq x] = F(x) \quad , \quad 0 \leq F \leq 1. \tag{5.2}$$

and a probability density distribution $f(x) = F'(x)$ (for differentiable F(x)). If we now consider a transformation from r to x, r=h(x), with h monotonically increasing, and in particular we choose h(x)=F(x) i.e.

$$r = F(x) \tag{5.3}$$

or equivalently, for invertible F(x),

$$x = F^{-1}(r) \tag{5.4}$$

we can make a sampling of the random variable x, distributed according to (5.2), by simply making a uniform sampling of the random variable r in the interval [0,1] and then evaluating x from eq. (5.4).

5.2.2 The Geant4 package

Geant4 [110] is one of the first successful attempt to re-design a a big package of High Energy Physics (HEP) software for the next generation experiments using an Object-Oriented environment. A variety of requirements also came from heavy ion physics, CP violation physics, cosmic ray physics, astrophysics, space science and medical application.

Geant4 has many types of geometrical descriptions, in order to have the flexibility to simulate the most complicated and realistic geometries. Everyting is open to the user:

- Choice of physics processes/models;

- Choice of GUI/Visualization/persistency/histogramming technologies

In Geant4 a large variety of physics processes are covered:

- Standard EM processes;

- Low energy EM processes;

- Hadronic processes;

- Photon/lepton-hadron processes;

- Optical photon processes;

58
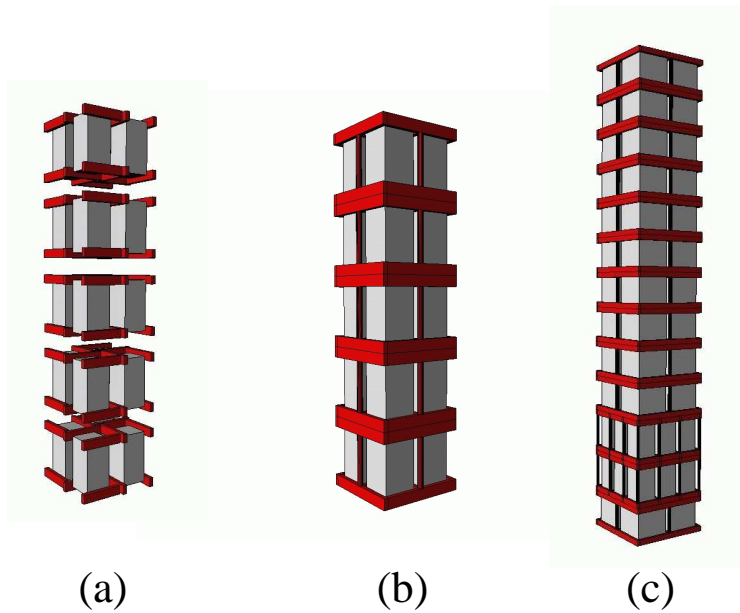
Figure 5.2: *Simulated detector arrays for MiDBD-I (a), MiDBD-II (b) and CUORICINO(c).*

- Decay processes;

- Shower parameterization;

- Event biasing technique.

The package provides sets of alternative physics models, so that the user can freely choose appropriate models according to the type of needed application.

Thanks to its geometrical and physical variety and flexibility Geant4 is not only for HEP but goes well beyond that. It has been found to be very useful also for the simulation of the physics and the geometry of DBD bolometric experiments, that belong to the field of low energy physics.

5.3 Simulated geometries

The Geant4 package has been used to write a C++ code, able to simulate the entire structure of the experiments MiDBD-I, MiDBD-II, CUORICINO and CUORE. The experimental elements included in the code are:

- Borated PET shield (in MiDBD-II, CUORICINO and CUORE);

- External lead shield;

- The entire set of copper thermal shields of the cryostat (Main Bath, Outer Vacuum Chamber, radiation, Inner Vacuum Chamber, 600 mK, 50 mK shields);

- Roman lead internal shields;

- Copper plates entirely surrounding the detector tower (Copper Box);

- Copper bars that hold the copper structure;

Figure 5.3: *Details of the simulated 4 crystal module (left) and of the 9 crystal module (right) of CUORI-CINO.*

(a)　　　　　　　　　(b)
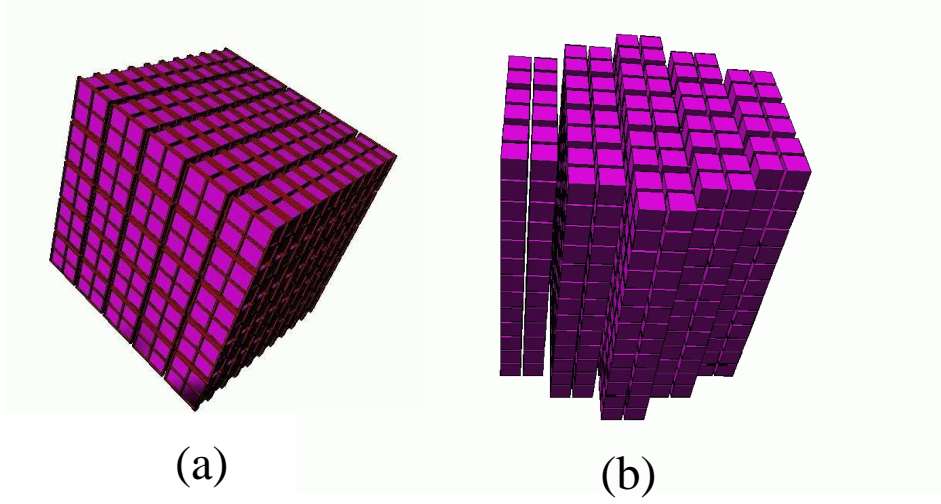
Figure 5.4: *Cubical (a) and cylindrical (b) structures for the CUORE array.*

- Copper frames that host the crystals;

- TeO$_2$ crystals;

- All the small parts as Cu screws, Cu pins, Teflon parts, NTD thermistors, gold wires.

In Fig. (5.2) the three different tower array for MiDBD-I (a), MiDBD-II (b) and CUORICINO (c) are shown. In Fig. (5.3) details of the 4 crystal module (left) and of the 9 crystal module (right) of CUORICINO are illustrated. The crystals, the copper holding structure, the copper screws, the NTD thermistors and the gold wires can be seen. For the CUORE detector both cubical and cylindrical arrays have been simulated (see Fig. (5.4)), in order to chose the best structure in term of anticoincidence background reduction.

5.4   Simulated contaminations

As previously quoted the Geant4 package can account for a large variety of decay processes (alpha, gamma, beta, X decays, Internal Conversions, Electron Captures, etc.) and particle propagations

(Nuclear recoils, electron, gamma, heavy hadrons propagations, etc.). As illustrated in chapter (4) the main sources for the background observed in our experiments are due to external gammas, neutrons and muons and to internal contaminations of the experimental setup. The main contributions from internal radioactivity arise from ^{238}U , ^{232}Th chains, usually in secular equilibrium, and from single isotopes as for instance ^{210}Pb , ^{40}K and ^{60}Co. Also the unavoidable contribution due to the DBD2ν of ^{130}Te must be taken into account.

For radioactive chains or radioactive isotopes, alpha, beta and gamma/X ray emission need therefore to be simulated, according to their branching ratios and taking into account the time structure of the decay chains. This is obtained by means of the gendec code [111], that generates the processes occurring in a given decay with the correct time structure and the proper branching ratios.

With this tool we can use the Geant4 based code to simulate decay processes occurring in the bulk and on the surfaces of the various parts of the simulated experimental setup, in order to disentangle the sources responsible of measured background by comparing the simulated data with the experimental ones. The main information we want to extrapolate are:

- the localization of the contaminations actually dominating the measured background;

- the origin of the different contributions in the DBD region;

- the radioactive contamination level of the materials used in our experiments;

- the value of the background in the DBD region expected for CUORE when using for its computation the level of purity of the materials presently at our disposal;

On the bases of the obtained results we can find out the best strategy to be adopted in the R&D that must be performed for CUORE (material selection, surface cleaning, etc.). A program of measurements of determine the contamination level of the materials available for the construction of CUORE is necessary. The most appropriate and feasible technique to make the measurement of bulk contaminations is with underground germanium detectors, which we can access at the LNGS. As regards surfface contamination measurements the best and more sensitive technique found so far is ICPMS, provided by a facility located at the Ispra laboratories.

All these informations can be obtained by the comparison between experimental and simulated data. The Montecarlo code is in fact used to simulate the different background sources:

- LNGS environmental radioactivity;

- experimental setup radioactivity.

5.4.1 Environmental radioactivity

To take into account the sources due to environmental radioactivity we have simulated:

- high energy gamma rays from thorium and uranium chains uniformly distributed on a spherical surface surrounding the whole experimental volume and with decay rates normalized to the fluxes measured in the LNGS environment;

- neutrons with energies in the range $10 \div 10^9$ meV have been isotropically generated from outside the most external shield (external lead shield for MiDBD-I and Borated PET shield for MiDD-II and CUORICINO) with decay rates normalized to the fluxes measured in the LNGS environment;
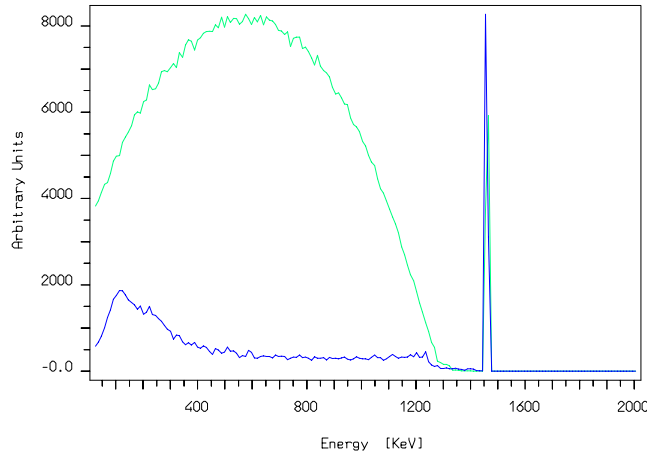
Figure 5.5: *Comparison between ^{40}K bulk contaminations in the crystals (green) and in the copper box (blue) bulk.*

- muons: a dedicated study based on the FLUKA package has been developed by our collaborators of the Saragoza University on the neutron production by muons in the external lead shielding of CUORICINO and CUORE. In a second step the spectrum obtained for the neutrons produced by muon interactions in the lead shieldings will be considered as a new source of radioactivity for the experiment and will be used as an input for the Geant4 code to evaluate the contribution to the background arising from muon induced neutrons.

5.4.2 Experimental setup radioactivity

We have simulated three different kind of sources for the radioactivity originated by contaminations of the experimental setup: bulk, surface and cosmogenic contaminations.

Bulk contaminations

Bulk contaminations of ^{238}U , ^{232}Th , ^{210}Pb , ^{40}K have been simulated in almost all the experimental elements. The shape of the energy spectrum generated by a particular contamination can vary considerably depending on the localization. In Fig. (5.5) the comparison between the energy spectra summed over all the detectors for ^{40}K contaminations in the crystals and in the copper box is shown. Normalizing the two spectra on the ^{40}K line at 1460 keV, the continuum for bulk contaminations in the crystals is considerably higher than the continuum for contaminations in the copper box. This is due to the contribution from the electrons of the beta decay, that in the second case loose their energy before reaching the detectors.

If we compare the spectra due to contaminations of ^{238}U or ^{232}Th in the bulk of the different copper shields (see Fig. (5.6)), we can notice that the relative intensity of the gamma lines belonging to a specific radioactive chain changes from one spectrum to another, and in particular that more is external the contaminated element and less the low energy gamma lines are visible in the spectrum. This happens because the low energy gamma rays originated from objects far away from the detectors don't have enough energy to reach them. The presence of low energy gamma lines in the background spectrum can therefore be ascribed to contaminations of elements located near to the
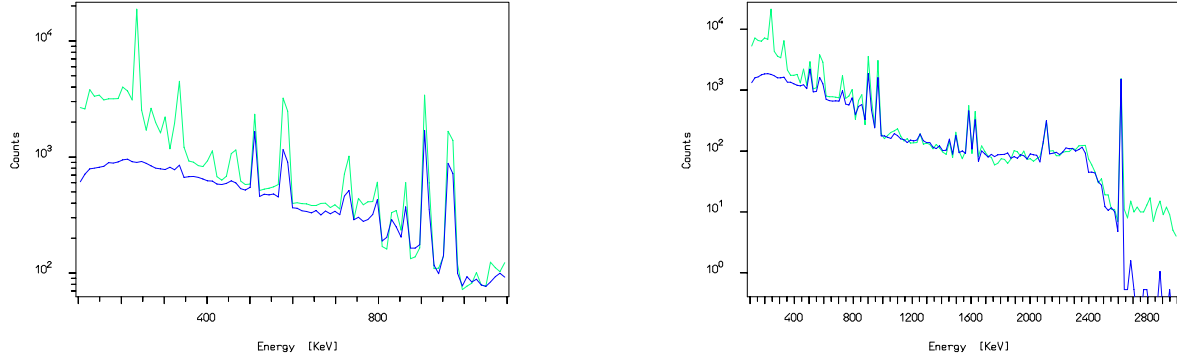
Figure 5.6: *Comparison between ^{232}Th bulk contaminations in the copper box (green), in the 600 mK copper shield (blue): gamma region (left); low energy region (right).*
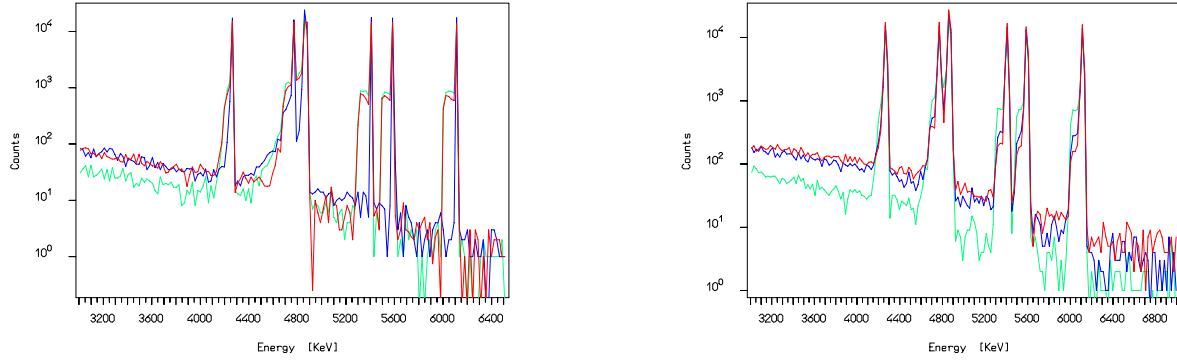
Figure 5.7: *Left: comparison between ^{238}U 1 μ depth surface contaminations in the crystals for different density profiles: uniform in 1 μm depth (green), on a thin surface located at 1 μm depth (blue), exponential density with attenuation lenght at 1 μm depth (red). Right: Comparison between ^{238}U surface contaminations in the crystals for different depths: 1μ (red), 3μ (blue), 5μ (green).*

crystals (bulk or surface contaminations).

Bulk contaminations of all the copper parts of the mounting structures (copper box and copper bars) produce similar spectral shapes. For this reason the spectra relative to the Cu Box bulk contaminations have been considered representative for the whole mounting structure, subject to normalization to the total mass.

The unavoidable background due to the DBD2ν of ^{130}Te in the crystals bulk has also been simulated, using the present upper limits.

Surface contaminations

Surface contaminations contribute to background in a remarkable way only when they are localized on the crystal or on the experimental elements directly facing them. Contaminations on surfaces not faced to the detectors give rise in fact to a contribution analogous and indistinguishable from the corresponding bulk contaminations. For this reason contaminations on these surfaces have not been considered for our simulations.

As for the bulk case we have simulated contaminations of ^{238}U , ^{232}Th and ^{210}Pb and ^{40}K. In addition we have also considered the possibility of secular equilibrium break in the ^{238}U chain.

Crystal surface contaminations   The shape of Montecarlo spectra and scatter plots obtained for contaminations simulated on the crystal surfaces strongly depends on the depth and on the density profile chosen for the simulation. Depths ranging from 0.1 μm to 10 μm for three different density profiles have been considered:

- uniform contamination within a surface layer of chosen thickness;

- uniform contamination on a surface located inside the material at chosen depth from the boundary;

- exponential density profile with a chosen decay lenght.

In Fig. (5.7 left) the comparison between the spectra obtained for simulations with the three considered density profiles for contamination of ^{238}U on the crystal surface at a depth of 1μm is shown. As it can be seen from this plot for the second kind of density profile a sharper shape of the peaks is obtained. This is due to the fact that for contaminations distributed on a surface located inside the material the probability that the nuclear recoil escapes from the crystal is lower than for contaminations distributed nearby the surface boundaries.

In Fig. (5.7 right) the comparison between the spectra due to ^{238}U surface contamination at three different depths (1,3 and 5 μm) for a exponential density profile is shown. The peaks corresponding to the full transition energy of the alpha decays for the ^{238}U chain are clearly visible. As it can be seen from this plot, the shape of the peaks strongly depends on the assumed depth: for contaminations distributed in a very thin surface layer a structure similar to a second peak appears on the left of the main peak, due to the escape of the nuclear recoil from the crystal surface. More deep is the contamination and more smooth and weak becomes this second peak.

As it is shown in Fig. (5.8) also the scatter plot varies considerably depending on the contamination depth. For depths of the order of 0.1 μm (Fig. 5.8(left)) the events on the scatter plot are more concentrated near the borders. This picture corresponds to alpha decays so near to the crystal surface that the emitted alpha particle completely releases its energy in the faced crystal. At the same time the corresponding nuclear recoil is scattered back and absorbed in the original crystal. The situation in which the nuclear recoil escapes and the alpha particle is scattered back is also possible. The scatter plot shown in Fig. (5.8)(right) corresponds to crystal surface contaminations with a depth of 5 μm. In this case the alpha particle (or the nuclear recoil) looses part of its energy in the original crystal, this generating a more uniform distribution of the detected event on a straight line corresponding to $E_A + E_B = Q$.

Copper surface contaminations   Surface contaminations of the copper in ^{238}U , ^{232}Th , ^{210}Pb , ^{40}K are assumed. Also in this case the possibility of secular equilibrium breaks in the ^{238}U chain is taken into account.

As it was done for the crystals, also for the copper elements we have considered different contamination density profiles and contamination depths. The shape of the simulated spectra varies considerably depending on these parameters. In Fig. (5.9)(left) the comparison between the spectra obtained for ^{238}U contaminations of the copper box surfaces at .2 μm, 1μm and 5μm depth is shown. For contaminations at depths less than 1 μm the alpha particle can escape from the copper surface and hits the detector. Structures at the energy of the alpha particle emitted in each alpha decay of the ^{238}U chain are clearly visible ("external peaks"). These peaks don't have a gaussian symmetric
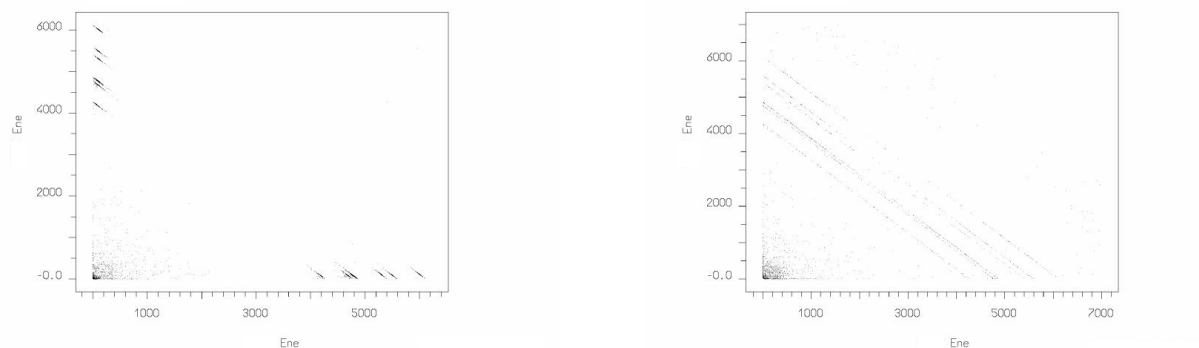
Figure 5.8: *Scatter plot for ^{238}U contamination on the crystals surface for (left) .1µm and (right) 5 µm depth.*
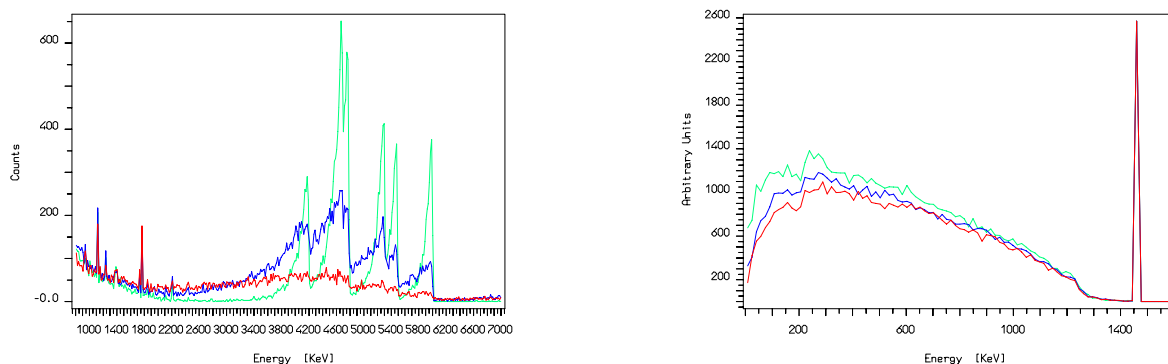
Figure 5.9: *Comparison between the spectra obtained for ^{238}U (left) and ^{40}K (right) contaminations of the copper box surface at 0.2 µm (green), 1µm (blue) and 5µm (red) depth.*

shape, but show an apparent energy tail, extending to low energies and due to the energy lost by the particle before reaching the detector. For deeper contaminations the probability that the alpha particle reaches the detector with the full energy decreases very quickly and for contaminations deeper than 5 µm the generated spectrum above 3 MeV is a continuum.

The observation of the "external peaks" in the background spectrum would be an indication of contaminations of the copper surfaces, distributed over a very thin layer. On the contrary the lack of these peaks would indicate a deeper contamination. A remarkable feature of the spectra originated by copper surface contaminations is the high contribution to the continuum between 3 and 4 MeV.

^{40}K contaminations of the copper box surfaces on the other hand don't seem to vary in an appreciable way with respect to the chosen contamination depth (see Fig. (5.9)right).

An exponential density profile was chosen for both crystals and copper surface contaminations. This choice is based on the consideration that the most natural deposition of impurities on surfaces should follow this density profile.

65
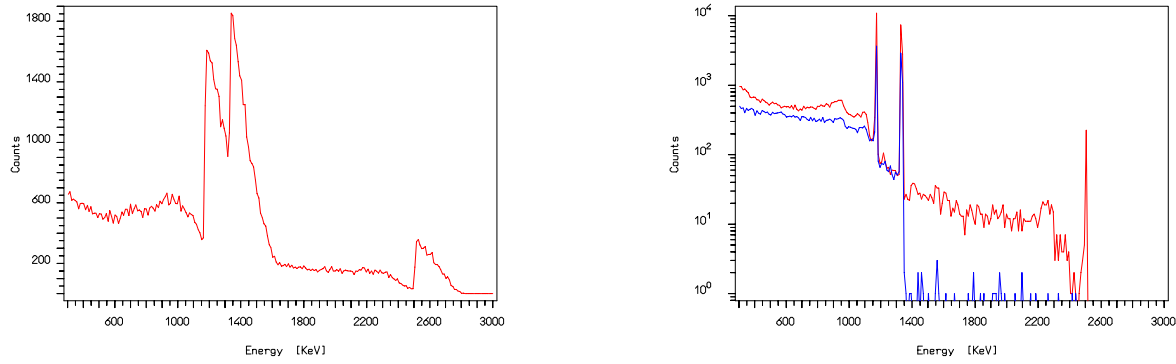
Figure 5.10: *Left: Montecarlo spectrum for ^{60}Co contamination in the crystals bulk. Right: compar ison between Montecarlo spectra for ^{60}Co contaminations in the copper box (red) and in the 50mK shield (blue) bulk.*

Cosmogenic contaminations

Cosmogenic activation of tellurium and copper has been also taken into account for our simulation of the background sources.

In order to evaluate the type and the amount of radio-nuclei produced by cosmic ray activation of tellurium and copper above ground we have used a code (COSMO) based on computed cross sections [109].

As said in section (4.2) the radio-nuclei produced by cosmic rays in tellurium are mostly tellurium isotopes (A=121,123,125,127) as well as ^{124}Sb, ^{125}Sb, ^{60}Co and tritium, the last three being of more concern because of their long half-life. ^{60}Co is the most dangerous activated radionuclide with respect to the DBD0ν research, for the high Q-value of its beta decay (2823keV). Bulk ^{60}Co contaminations of the crystals have therefore been taken seriously into account. A typical spectrum for this contamination is shown in Fig. 5.10 (left). The beta decay of ^{60}Co can occur on excited levels with the emission of two gamma rays of 1173 keV and 1332 keV energy respectively. The probability of single escape of these gamma rays is responsible for the two beta decay shapes visible in the spectrum with endpoints at 1650.9 keV and 1491.9 keV respectively. The double gamma escape is also possible but it is out of the range of the shown plot.

Also in the case of copper the most dangerous radionucleus produced by cosmic ray activation is ^{60}Co. Bulk contaminations of the copper parts of MiDBD, CUORICINO and CUORE in ^{60}Co have therefore been considered. In Fig. 5.10(right) the Montecarlo spectra generated from bulk ^{60}Co contaminations of the copper box and of the 50 mK copper shield are shown. In this case the electron emitted in the beta decay doesn't reach the detectors and the observed spectra correspond to the gamma interaction of the 1173 keV and 1332 keV photons. The two photoelectric peaks and the sum peak are visible in the spectrum of a contamination in the copper box (green). The probability that both the emitted gamma reach the detector in the case of far away contaminations (i.e. in the 50 mK shield (Fig. (5.10 right))(blue)) is negligible. As it can be seen from these plots, the contribution to the background in the DBD0ν region due to ^{60}Co contamination of copper is negligible.

An intermediate situation (sum gamma peak with a small contribution also from the beta decay) holds for experimental parts almost in contact with the detectors (i.e. Cu Frames).

66
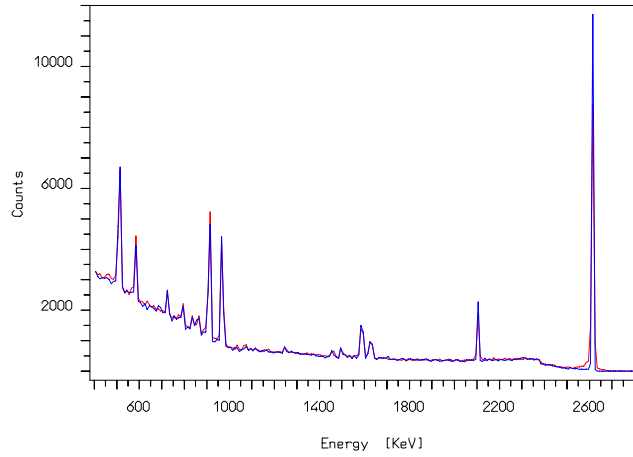
Figure 5.11: *Comparison between calibration spectrum (red) and simulated calibration spectrum (blue).*

5.5 Background study

To verify the reliability of our Montecarlo simulations we have performed a comparison between a calibration spectrum, obtained in the first run of CUORICINO with a ^{232}Th wire source placed between the OVC shield and the External Lead Shield, and the corresponding Montecarlo spectrum. This comparison is shown in Fig. (5.11). The excellent agreement between the measured calibration spectrum and the simulated spectrum (verified also evaluating the correspondence between the relative intensities of the observed lines and of the lines visible in the MC spectrum) gives positive indications of the ability of our Montecarlo simulations to reproduce the real experimental situation.

Once verified the reliability of our Montecarlo simulations, a background analysis method has been developed in order to disentangle the different sources responsible of the background measured with MiDBD-I, MiDBD-II and CUORICINO. This method is based both on data analysis tools and Montecarlo simulations and takes into account the history of each setup element and of each modification to the setup structure.

A MINUIT based code (mc2exp) has been developed in order to find the best linear combination of input Montecarlo spectra that gives the best agreement with the experimental spectrum. This code can be used also limiting the analysis to a chosen energy range in order to better disentangle the contribution of the different contaminations to the various energy regions. Limits or values for the normalization of the input Montecarlo spectra can also be fixed by the user, according to preliminary evaluations of their expected contribution to the measured background.

Main goal of this procedure is to reproduce the anticoincidence background spectrum by means of the Montecarlo simulated spectra. This is performed in three main steps:

1. reproducing alpha peaks;

2. reproducing the continuous background observed above 3 MeV;

3. reproducing the gamma region.

Figure 5.12: *Comparison between Montecarlo and CUORICINO anticoincidence (top) and coincidence (bottom) spectra in the case of TeO$_2$ crystal surface contaminations ($\lambda \sim 1\mu m$).*

Alpha peaks

The energy region above 4 MeV is analyzed in this first step. The anticoincidence background spectrum in this region is dominated by alpha interactions that give origin to peaks. Only contaminations located nearby the detectors (bulk and surface contaminations in ^{238}U , ^{232}Th , ^{210}Pb of the crystals and of the detector components and mounting structure) can therefore contribute to the background in this region.

The shape of the peaks (gaussian symmetric shape or low energy tail, secondary peaks, etc.) and the peaks position (full transition energy or alpha energy) are useful informations in a preliminary evaluation of the best Montecarlo simulations which better reproduce the observed alpha peaks. In fact, as previously said the localization (bulk or surface of crystals or mounting structure elements), the density profile and the depth of the contamination give rise to spectra with alpha peaks with different shapes.

In addition the analysis of coincidence spectra and scatter plots can be used to evaluate the presence and the nature of surface contaminations of the crystals.

After preliminary considerations made by means of these tools, the most probable sources of the alpha peaks are identified and given as input to the mc2exp code. The minimization procedure finds for each of the input Montecarlo spectra, the best normalization for which the linear combination of the normalized spectra minimizes the difference from the experimental one. The contaminations responsible for the alpha peaks are therefore localized and quantified (Fig. 5.12).

A direct check of the reliability of the obtained result is given by the comparison between the measured coincidence spectrum and the corresponding linear combination of the Montecarlo coincidence spectra with the just found normalization values. A good reproduction of the background spectrum for the events involving two detectors (multiplicity 2) is a further check of the goodness of the obtained result.

A resonable statistics, together with a good resolution and calibration of the background spectrum in the alpha region are necessary requirements, in order to identify with good precision the

observed alpha peaks (full energy or alpha energy peak position, etc.). A high efficiency on coincidences is also fundamental to separate the contributions due to crystal surface contaminations from other surfaces contributions.

3-4 MeV range

The energy region between 3 and 4 MeV is a region where no known γ nor α lines from natural and cosmogenic radioactivity are present. The main source for the background in this region is due to alpha decays occurring on the surfaces of the crystals and of the other elements facing them. The contribution arising from crystal surface contaminations can be derived by a comparison between coincidence and anticoincidence background spectra. Only contaminations located on that part of the crystal surfaces (S^{act}) directly facing other detectors can contribute to coincidence events with energies above 3 MeV. On the other hand, the decay occurring in the fraction of crystal surface (S^{inert}) which faces inert materials (e.g. copper mounting structure) contribute to the anticoincidence background spectrum. From the coincidence spectrum we can obtain the rate R_D in the 3-4 MeV region due to contaminations on S^{act}. By simply considering the geometric evaluation of the ratio S^{inert}/S^{act} (average Monte Carlo evaluation) we can obtain from R_D the expected crystal surface contribution to the anticoincidence spectrum in the 3-4 MeV region. Now it is possible to subtract the crystal contribution to the anticoincidence spectrum in order to obtain the residual contribution due to inactive surfaces.

Possible sources for the background in this region are surface contamination of the copper faced to the detectors (mounting structure and copper box) and contamination of other components close to the detectors (such as the Teflon spacers placed between the copper frame and the crystals, the NTD thermistors, the Si heaters). Also neutrons and muon induced neutrons have been taken into account.

The spectra relative to the possible sources of the background in the 3-4 MeV region are given as input to mc2exp together with the normalized spectra obtained in the first analysis step, in order to reproduce the background region above 3 MeV (Fig. 5.13). The result obtained give us the localization and the entity of the contaminations responsible for the background in the high energy region of the measured spectrum.

Unfortunately no direct check is available. Some indications come from the analysis of the low energy gamma peaks in the spectrum; a high statistics in the collected background data is necessary. Other independent radioactivity measurements must be performed to make a cross check of the obtained results and to evaluate the surface contaminations of the experimental materials faced to the detectors.

Gamma region

The ingredients used to identify the contaminations responsible of the background in the alpha region refer to impurities localized in the detectors themselves or in experimental parts directly facing them. The contribution of these sources to the gamma region should account for most of the low energy gamma lines belonging to the ^{238}U and ^{232}Th chains. Other contribution to the gamma lines of this chains should arise from bulk impurities of ^{238}U and ^{232}Th of all the experimental parts. ^{40}K and ^{60}Co contaminations of copper and TeO$_2$ are needed to account for the observed gamma lines relative to these isotopes. Bulk impurities of ^{210}Pb and the DBD2ν of ^{130}Te are also considered as possible sources for the continuous background in the gamma region.

The spectrum obtained by combining the normalized Montecarlo spectra, relative to the background sources identified in the first and second step of the analysis procedure, is given as input to
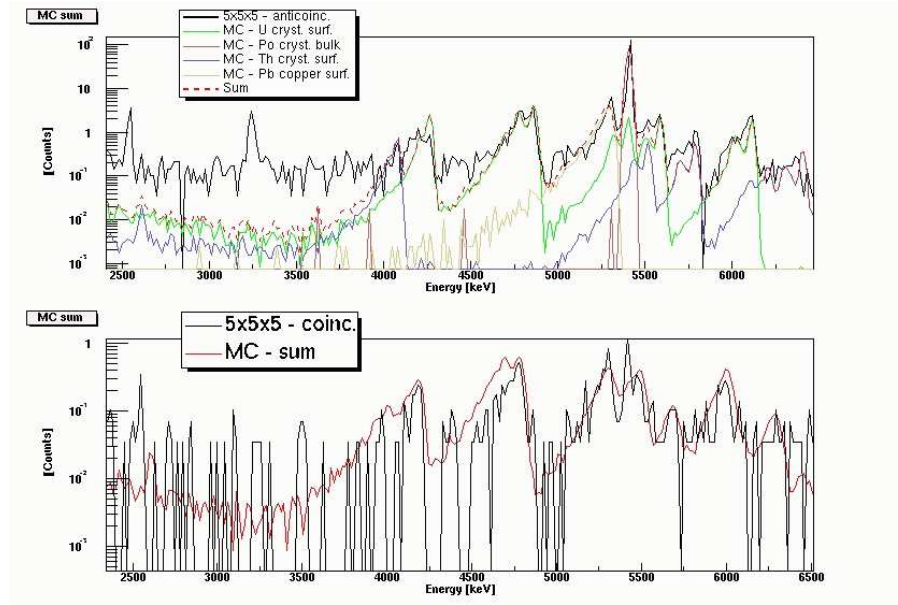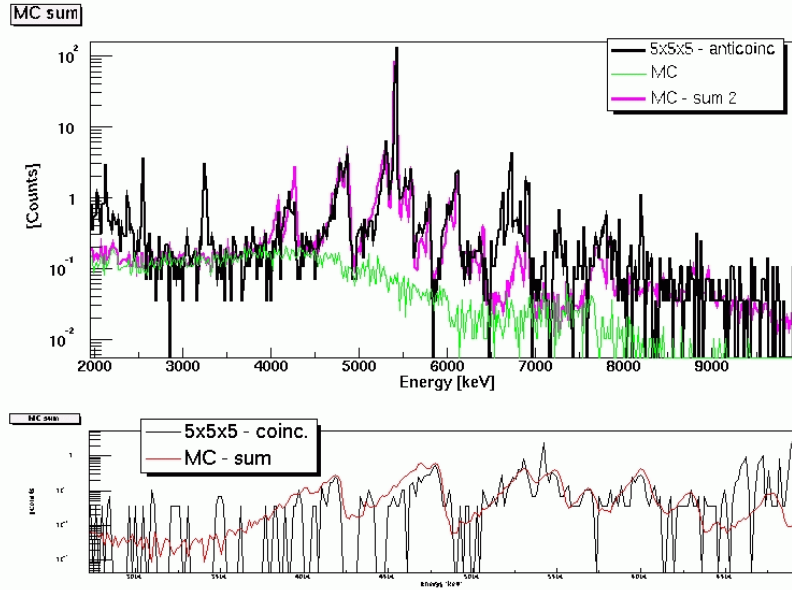
Figure 5.13: *Comparison between Montecarlo and CUORICINO anticoincidence (top) and coincidence (bottom) spectra in the case of TeO$_2$ crystal surface contaminations ($\lambda \sim 1\mu m$) + copper surface contamination in ^{238}U/^{232}Th ($\lambda \sim 5\mu m$).*

the minimization procedure, together with the simulated spectra relative to the possible radioactive sources for the gamma region. The experimental spectrum is then fitted in the full energy range, in order to localize and quantify the radioactive sources that can account for our measured background.

5.6 A more conservative approach

The analysis method presented in section (5.5) has got some limitations. Unfortunately the not perfect calibration of the background spectrum in the alpha region, together with an energy resolution not always good enough to separate alpha peaks with very similar energies makes the identification of the sources responsible for the observed alpha peaks quite difficult. In particular the most critical parameter in this phase is represented by the contamination depth, from which the peaks shape and the continuum contribution strongly depend.

This fact also influences the fit of the region between 3 and 4 MeV. Different depths for the surface contaminations responsible for the alpha peaks mean in fact different low energy tails, or, in other words, different contributions in the 3-4 MeV energy range. At the same time the spectra relative to contaminations deeper than 5 μm of the surfaces faced to the crystals, assume almost indistinguishable shapes in this region in spite of the choice of the contaminant impurities (^{238}U , ^{232}Th , ^{238}U broken chain,^{210}Pb).

At the same time the choice of the surface impurities strongly influences the contribution given to the gamma region, mainly to low energy gamma lines and continuum. The contribution ascribed to the sources responsible for the region between 0 and 3 MeV can therefore change.

These considerations make us aware of the fact that the quantifications of the identified background sources obtained with this technique must be taken as general indication, but cannot be considered reliable measurements for the contamination levels of our materials. Independent radioactivity bulk and surface measurements are therefore fundamental to evaluate the impurity level

70

of our experimental setup. On the other hand, this background analysis method, even if model dependent, is very useful in giving indications of the sources responsible of the measured background and can therefore address our efforts in background study and reduction.

A more conservative approach enable us to obtain the 90%C.L. upper limits for the contamination levels of the used materials. This value is obtained by maximizing the contribution to the background due to each of the Montecarlo spectra (one for every simulated isotope or chain in every single experimental element) compatibly with the measured background spectrum. The obtained limits are very conservative since correspond to the maximal contribution that can be ascribed to a specific contamination.

The knowledge of the background and of the contamination level of the materials used so far in MiDBD and CUORICINO are of fundamental importance for the optimization of the CUORE detector with respect to background reduction. More details will be given in chapter (7).

Chapter 6

MiDBD background analysis

Introduction

The MiDBD experiment, carried out in Hall A of LNGS by the Milano group between the years 1997 and 2001, was only the last of a series of experiments on DBD0ν of ^{130}Te, based on the bolometric technique. In fact, the improvements in the detector performance obtained over years of measurements with devices of constantly increasing size, led to a large mass, low background experiment whose results finally demonstrated the competitiveness of the low temperature calorimeters.

The big effort carried out in the R&D with respect to detector optimization and background reduction, made us decide to perform in 2001 a second run (MiDBD-II), in which the MiDBD tower was completely rebuilt with a structure very similar to CUORICINO. All the surfaces of the TeO$_2$ crystals and of the mounting structure were subject to a dedicated etching process aiming to reduce radioactive contaminants (see section (4.2)). In this occasion, due to the more compact structure of the tower, an enlargement of the internal roman lead shields was possible. An external borated PET neutron shield was added in June 2001.

The available data have been analyzed in order to extract the most relevant information, concerning both the physical processes (single and double beta decays) and the background origin.

6.1   Data and detector performances

The MiDBD data collection was divided in sets of about 15-20 days. At the beginning and at the end of each data set the detector was calibrated with an exposure, lasting about 3 days, to a mixed U and Th source placed at the two opposite sides of the 20 crystal tower, just in contact with the external cryostat thermal shields.

The excellent reproducibility of the MiDBD detectors is shown in Fig. (6.1) where the total calibration spectrum, obtained by summing the spectra of the 20 detectors, is presented. The overall energy resolutions in the total calibration and background spectra for MiDBD-I and MiDBD-II are reported in Tab. (6.1).

In Tab. (6.2) the single detector response and resolution, evaluated in the calibration spectrum at the 2615 keV ^{208}Tl line, are reported for both MiDBD-I and MiDBD-II. The distributions obtained in the two runs with respect to pulse height and energy resolution (2615 keV line) are compared in Fig. (6.2).

As it can be seen in Tab. (6.2) in MiDBD-II some detectors are missing. In the second run we had in fact to face three main problems:
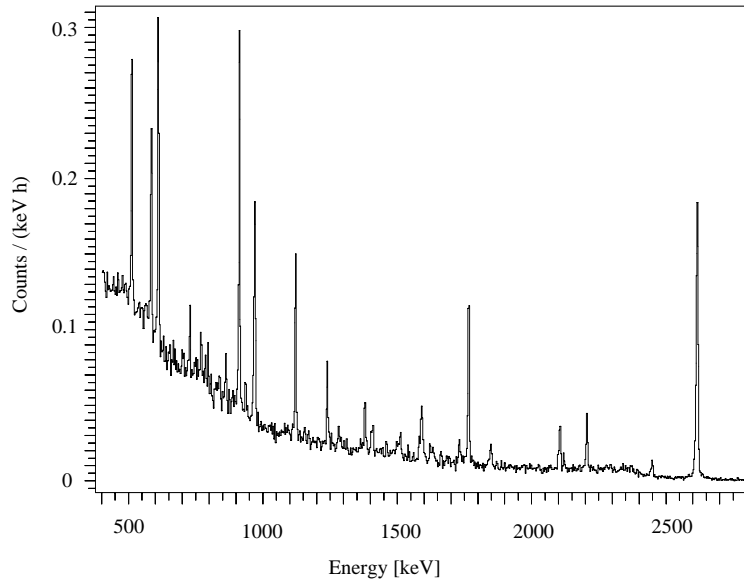
Figure 6.1: *U+Th calibration, sum spectrum of the 20 detectors.*

Calibration				
E_γ [keV]	583	911	1460	2615
FWHM [keV] (MiDBD-I)	3.6	4.3	5.9	8.1
FWHM [keV] (MiDBD-II)	3.9	5.7	6.8	8.7
Background				
E_γ [keV]	583	911	1460	2615
FWHM [keV] (MiDBD-I)	4.2	5.1	6.7	9.3
FWHM [keV] (MiDBD-I)	4.0		9.7	15

Table 6.1: *FWHM resolutions (keV) in calibration spectrum (top) and in the 80000 hours×crystal (MiDBD-I) and 11000 hours×crystal (MiDBD-II) background spectra for MiDBD-I and MiDBD-II*

- 1 detectors could not be read-out, because of the breakage of its signal wires and 4 detectors could not be used because of the disconnection of the silicon heater;

- the breakage of four heater connections caused the impossibility to stabilize the corresponding detectors. They could not therefore be used to increase the statistics;

- some detectors had too high noise to acquire their signal.

Due to the high number of not working detectors and to the short measuring time, the statistics of MiDBD-II was limited and the coincidence analysis technique was therefore less efficient.

6.2   DBD results

The two MiDBD runs totalled ∼31,508 (MiDBD-I) and ∼5,690 (MiDBD-II) kg×hours of effective running time, respectively. Sum spectra were obtained both with no anticoincidence cut and by operating each detector in anticoincidence with all the others ("anticoincidence cut").

MiDBD-I			MiDBD-II		
Cryst.	Ampl. (μV/MeV*kg)	FWHM (2615keV) (keV)	Cryst.	Ampl. (μV/MeV*kg)	FWHM (2615keV) (keV)
F	163	7.4	F	178	7.2
16	91	4.5	16	41	-
130 -1	40	21.1	O	134	11
0	148	12.4	11	149	12.4
11	108	7.5	130-1	141	20.0
6	116	6.5	2	174	8.0
H	125	10.7	8	137	7.7
128 - 1	32	15.9	E	141	8.8
14	191	6.7	4	129	8.1
I	180	5.4	128-2	181	10.6
2	192	9.1	B	185	11.7
5	133	7.7	5	204	6.9
130 - 2	65	10	9	186	6.5
9	112	9.8	13	141	8.1
13	80	7.2	130-2	145	11.6
4	131	8.7	6	178	-
8	174	6.1	H	0	-
128 - 2	102	10.4	14	0	-
E	75	6.7	I	0	-
15	162	5.8	128-1	92	15.0

Table 6.2: *Detector performances in MiDBD-I and MiDBD-II*

The sum of the spectra obtained in anticoincidence in the two runs in the region above 2 MeV is shown in Fig. (6.3). It corresponds to $\sim$3.56 kg $\times$year of TeO$_2$ and to $\sim$0.98 kg $\times$year of ^{130}Te . The clear peaks corresponding to the lines at 2104 keV (single escape of the 2615 keV ^{208}Tl line), at 2204 keV (^{214}Bi) and at 2615 keV (^{208}Tl), confirm the reproducibility of the array during both runs.

No peak appeared in the region of DBD0ν of ^{130}Te, where the rates were of 0.59 $\pm$ 0.06 and 0.33 $\pm$ 0.11 counts/keV/kg/y respectively for MiDBD-I and MiDBD-II, when operated in anticoincidence. Also, no peak appeared at the energies corresponding to DBD0ν of ^{130}Te to excited levels of ^{130}Xe, nor at the energy of 867 keV corresponding to DBD0ν of ^{128}Te.

Fit parameters and 90 % C.L. limits for the various decay processes (Tab. 6.3) were evaluated with a maximum likelihood procedure [112], applied to the total (MiDBD-I and MiDBD-II) anticoincidence spectrum. Assuming a Poisson statistics for the binned data the fit procedure was formulated in terms of the likelihood chisquare (χ^2_L):

$$\chi^2_L = 2 \sum_i (y_i - n_i + n_i ln(n_i/y_i)) \tag{6.1}$$
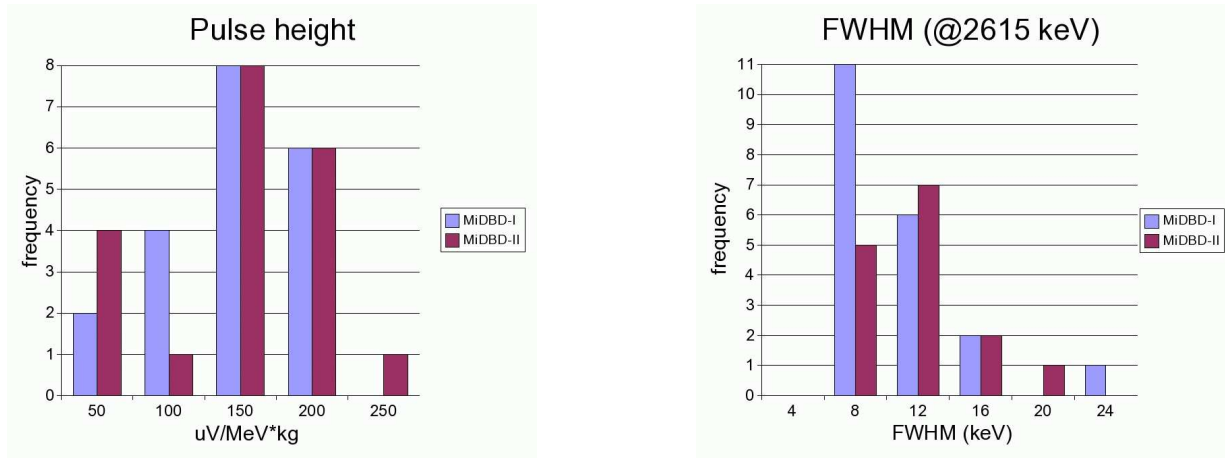
Figure 6.2: *Distributions of the pulse height (left) and FWHM at the 2615 keV ^{208}Tl peak (right) for MiDBD-I and MiDBD-II.*

where n_i is the number of events in the ith spectrum bin and y_i the number of events predicted by the fit model. Fit parameters were estimated by minimizing χ^2_L, while limits were obtained, after proper renormalization, just considering the χ^2_L distribution in the physical region [3]. A global fit procedure based on the minimization of $\chi^2_T = \sum_i \chi^2_i$ was adopted to combine different measurements. Similar results were however obtained following the approach proposed by G.J. Feldman and R.D. Cousins [113].

Isotope	Transition	Cuts	E_0 (keV)	Efficiency (%)	$T_{1/2}$ (years)
^{130}Te	$0\nu : 0^+ \rightarrow 0^+$	a.c.	2528.8	84.5	$> 2.1 \times 10^{23}$
^{130}Te	$0\nu : 0^{+*} \rightarrow 0^+$	none	1992.8	7.9	$> 3.1 \times 10^{22}$
^{130}Te	$0\nu : 0^{+*} \rightarrow 2^+$	none	1992.8	37.5	$> 1.4 \times 10^{23}$
^{130}Te	$2\nu : 0^+ \rightarrow 0^+$	a.c.			$\left(6.1 \pm 1.4^{+2.9}_{-3.5}\right) \times 10^{20}$
^{130}Te	$1\chi : 0^+ \rightarrow 0^+$	a.c.			$> 2.2 \times 10^{21}$
^{130}Te	$2\chi : 0^+ \rightarrow 0^+$	a.c.			$> 0.9 \times 10^{21}$
^{128}Te	$0\nu : 0^+ \rightarrow 0^+$	a.c.	867.2	97.9	$> 1.1 \times 10^{23}$

Table 6.3: *Half lifetime limits (90 % C.L.) on lepton violating and conserving channels deduced from the MiDBD data analysis. E_0 is the energy analyzed to obtain $T_{1/2}$, while* a.c. *indicates that the anticoincidence spectrum was used. [86]*

For the effective neutrino mass $< m_\nu >$ we obtained upper limits in the ranges (1.1-2.6) eV, taking into account theoretical uncertainties in the calculation of the nuclear matrix elements.

The 90% C.L. limit for DBD2ν of ^{130}Te , reported in Tab. (6.3), already excludes a relevant loss of the daughter isotope in geochemical experiments, which has been considered by O.K. Manuel [45]. We attempted also an evaluation of the rate for this lepton conserving process by analyzing the subtraction between the sum of the two spectra of the crystals isotopically enriched in ^{130}Te and the sum of those of the crystals enriched in ^{128}Te (Fig. (6.4)), for the data collected in the second run.

The spectrum resulting from this subtraction is positive in the region of DBD2ν with an excess of 269$\pm$60 counts, corresponding to $T_{1/2} = \left(6.1 \pm 1.4 stat.\right) \times 10^{20}$ years. However a precise evaluation of the half life is not straightforward because the background differs among the four
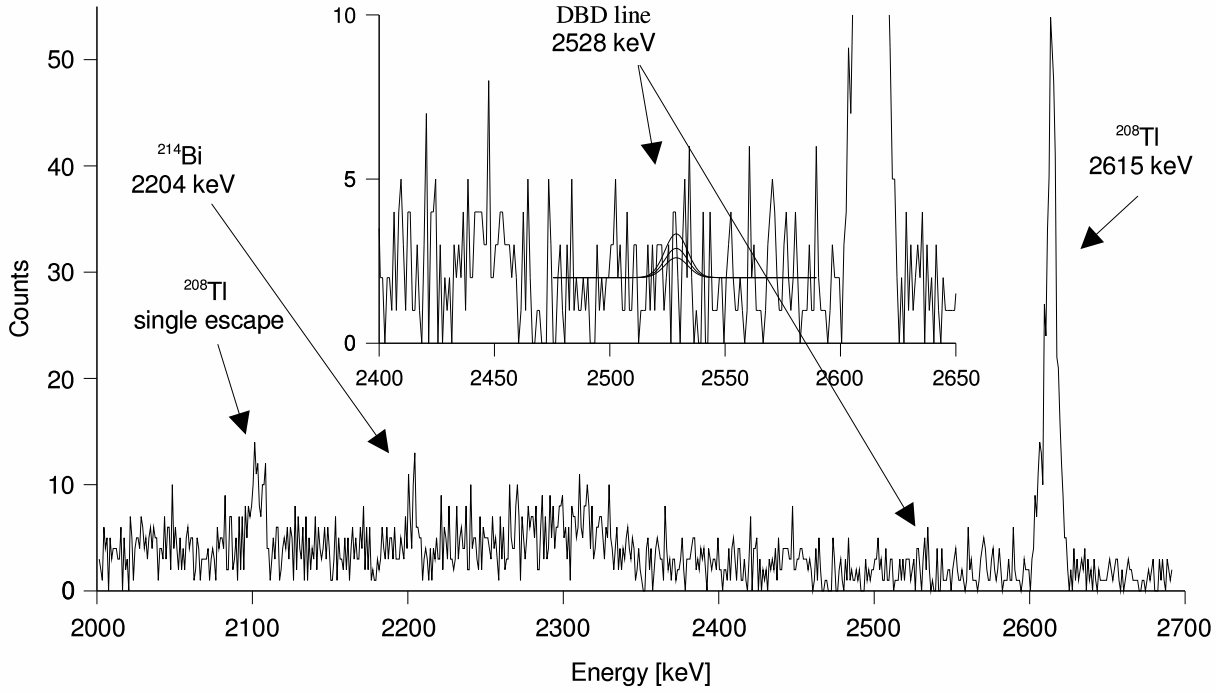
Figure 6.3: *Total spectrum (in anticoincidence) in the region of DBD0ν obtained with the twenty crystal array. The solid curves represent the best fit (lowest curve) and the 68 % and 90 % C.L. excluded signals.*

enriched crystals. In particular different rates are observed for the 1460 keV gamma line of ^{40}K and for the alpha lines in the 4-6 MeV energy region (Tab. (6.6) and (6.4)). In addition the two crystals enriched in ^{128}Te have different rates in the energy region between 600 and 1000 keV.

	40 K c/h·10^{-2}	400-1400 c/keV/h·10^{-4}	400-600 c/keV/h·10^{-4}	600-800 c/keV/h·10^{-4}	800-1000	1000-1400
130-1	1.3+/-0.5	7.2+/-0.2	14.9+/-0.8	8.1+/-0.6	6.4+/-0.5	3.5+/-0.3
130-2	5.0+/-0.8	7.2+/-0.2	13.7+/-0.7	8.6+/-0.6	6.6+/-0.5	3.7+/-0.3
128-1	2.3+/-0.6	6.6+/-0.2	13.8+/-0.7	7.8+/-0.5	5.4+/-0.5	3.1+/-0.2
128-2	1.6+/-0.5	5.8+/-0.2	13.1+/-0.7	6.5+/-0.5	4.0+/-0.4	2.9+/-0.2
nat.	0.6+/-0.1	4.85+/-0.06	10.7+/-0.2	5.7+/-0.2	4.1+/-0.1	1.92+/-0.06

	1500-2000 c/keV/h·10^{-4}	2000-3000 c/keV/h·10^{-4}	3000-4000 c/keV/h·10^{-4}	4000-5000 c/keV/h·10^{-4}	5000-6000 c/keV/h·10^{-4}
130-1	0.8+/-0.1	0.30+/-0.05	0.58+/-0.07	5.5+/-0.1	2.2+/-0.2
130-2	1.0+/-0.1	0.28+/-0.05	0.28+/-0.05	3.0+/-0.1	1.8+/-0.2
128-1	0.8+/-0.1	0.30+/-0.05	0.73+/-0.08	7.4+/-0.2	2.2+/-0.2
128-2	0.8+/-0.1	0.40+/-0.06	0.44+/-0.06	4.4+/-0.2	2.1+/-0.2
nat.	0.57+/-0.03	0.23+/-0.01	0.11+/-0.01	0.71+/-0.02	0.80+/-0.03

Table 6.4: *Background integrals for the gamma and alpha energy regions evaluated for the four isotopically enriched crystals in MiDBD-II.*

With the aid of a Montecarlo simulation of the possible background contributions, we were able to restrict the possible sources responsible of these lines. Both the sources responsible for the differences in the rates measured by the four isotopically enriched crystals (^{40}K and alpha contaminations)
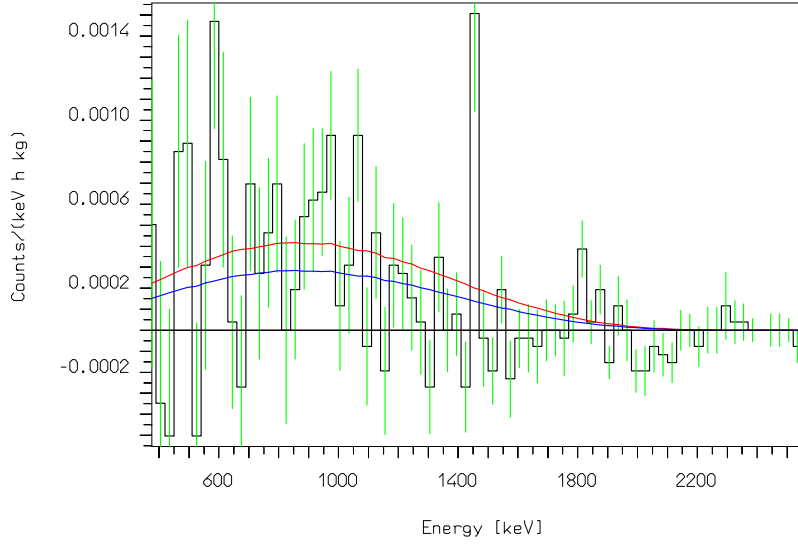
Figure 6.4: *Total difference spectrum between ^{130}Te and ^{128}Te detectors (no background subctraction). The solid curves represent the best fit (lowest curve) and the 90% C.L. excluded signal (Tab. (6.3)).*

can contribute to the background in the DBD2ν energy region. It's therefore necessary to evaluate these contributions and the systematic errors we face while considering the subtraction between spectra of detectors having different backgrounds.

As it is shown in Tab. (6.4) the intensity of the ^{40}K line is higher in the isotopically enriched crystals than in the natural ones. In addition the measured rate differs from crystal to crystal also within the enriched ones. Although the most naive explanation for these differences would be a different bulk contamination in ^{40}K for the four enriched crystals, this hypothesis must be rejected. The Montecarlo simulations in fact show that the continuum background that would arise in this case from the beta decay, is higher than the measured one. Tests performed by simulating various localizations for a ^{40}K source, permitted to find the best reproduction of the relative intensities of the 1460 keV line for the four enriched crystals, by considering a point-like source on the bottom surface of the copper holder. By means of the Montecarlo code we have then evaluated the contribution that this source would give to the background measured by each of the four enriched crystals, and consequently also to the ^{130}Te -^{128}Te difference spectrum. The maximum expected difference due to background from ^{40}K is positive and corresponds to 86 counts, which should therefore be subtracted from the actually evaluated DBD2ν signal.

The alpha peaks observed in the spectra of the four isotopically enriched crystals can be ascribed to surface contaminations of the crystals in ^{238}U , ^{232}Th and ^{210}Pb . The intensity of these peaks is different from one crystal to another, and therefore the sources responsible of these contributions will give rise to different rates in the DBD2ν energy region. In order to evaluate the continuum contribution due to the identified surface contaminations, we have used the mc2exp code. Using this fit procedure we have found the best linear combination of the contaminations spectra (we have also added contributions from the copper surfaces), able to reproduce the measured background. We have then evaluated the contribution of the surface impurities of ^{238}U , ^{232}Th and ^{210}Pb to the DBD2ν energy region of each of the four enriched crystals spectrum, and therefore also to the
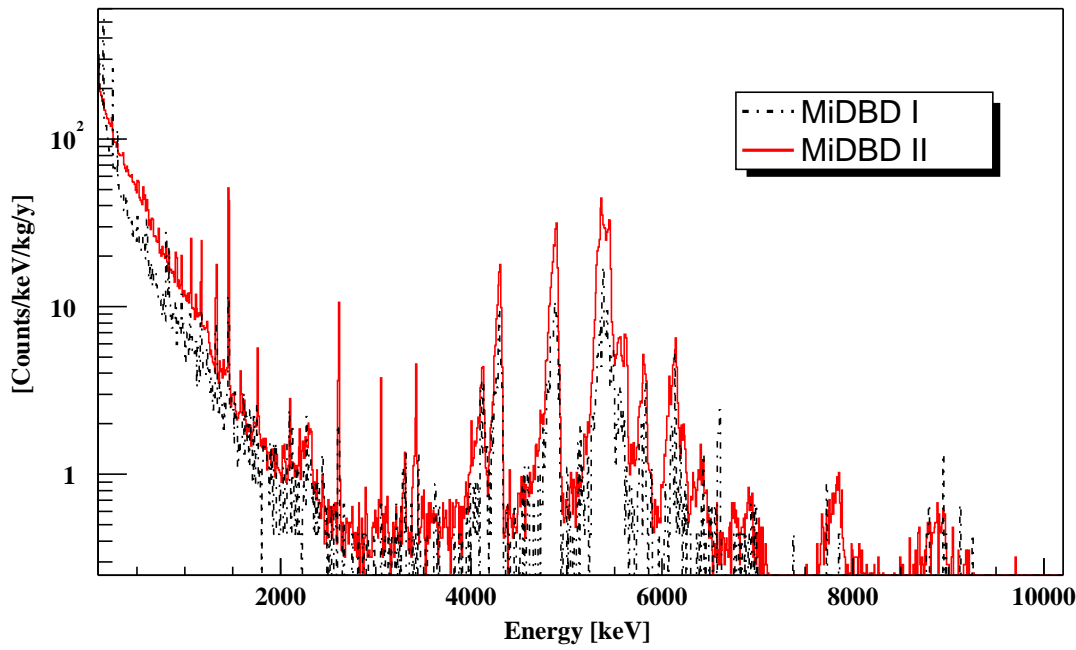
Figure 6.5: *MiDBD-I (continuous line) and MiDBD-II (dashed line)background spectra after anticoincidence cut.*

^{130}Te -^{128}Te spectrum. The maximum expected difference due to these contaminations is negative and corresponds to 380 counts, which should therefore be added to the actually evaluated DBD2ν signal.

We concluded that the differences in the crystal background rates could not account for the DBD2ν effect, but introduce a large systematic in the half life time evaluation. Our analysis of the measured background of the enriched crystals was performed in order to find out the sources configuration that could give the maximum contribution to the DBD2ν energy region of the ^{130}Te -^{128}Te spectrum. Other configurations, able to account for the background measured by the four crystals, could give minor contributions to the ^{130}Te -^{128}Te spectrum. For this reason the above quoted background rates have been assumed as the maximum possible contribution to the systematic error, obtaining the final result $T_{1/2} = \left(6.1 \pm 1.4 stat._{-3.5}^{+2.9} sys.\right) \times 10^{20}$ years. This value, while in agreement with most geochemically obtained results, looks somewhat higher than most of those predicted theoretically [114]. The already running NEMO 3 experiment [115], as well as an improved search to be carried out with the larger mass CUORICINO array, will allow to reduce soon the present uncertainties.

6.3 Background results

The sum spectra of the two runs obtained after applying the anti-coincidence cut are compared in Fig.(6.5). In Fig. (6.6) the gamma and the alpha energy regions are separately shown. Analyzing the structures observed in the measured background spectra we can make some considerations with respect to the radioactive contaminants contributing to the observed background.

In both the spectra the main gamma lines due to the natural activity of the ^{232}Th and ^{238}U chains, of ^{40}K and the lines at 1173 and at 1332 keV due to cosmogenic ^{60}Co are observed. The exposure of
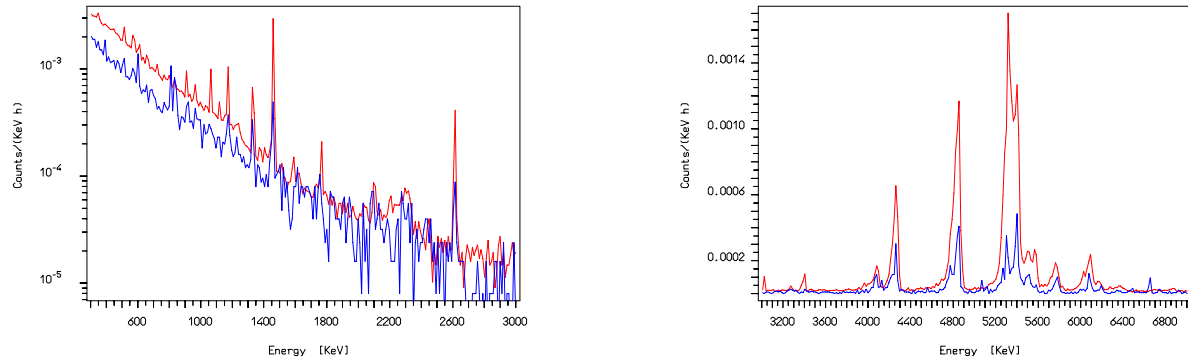
Figure 6.6: *Background comparison between MiDBD-I (red) and MiDBD-II (blue) in the gamma region (left) and in the alpha region (right).*

the crystals to the cosmic radiation during the assembling of the second run results in the presence of Te activation lines in the energy spectrum.

The intensities of the main gamma lines observed in both MiDBD-I and MiDBD-II are shown in Tab. (6.5). A clear reduction in the intensities of the main gamma lines due to natural activity is observed in MiDBD-II.

"Internal peaks" at the transition energy of alpha decays due to ^{238}U and ^{232}Th contaminations are clearly visible in both the spectra. An "external peak" with a low energy tail is also visible at 5.3 MeV, at the alpha energy of the ^{210}Pb decay. The rate of the ^{210}Po alpha peaks at 5.3 and 5.4 MeV (alpha and alpha + recoil energy) is stable in time, thus indicating that they should be ascribed to ^{210}Pb contaminations and not ^{210}Po (T$_{1/2}$=138.4 d). The integral in the 3-4 MeV region and the alpha peaks intensities, measured in MiDBD-I and MiDBD-II, are shown in Tab. (6.6), separately for natural and enriched crystals. As previously quoted the enriched crystals show higher intensities for the alpha lines and at the same time a poorer statistics. They have been therefore separately analyzed. In the 3-4 MeV energy region a gaussian peak at about 3250 keV is observed. Its contribution was therefore subtracted to the measured rate in 3-4 MeV energy region, in order to evaluate the continuous background in this interval. From Tab. (6.6) we can clearly see that the ^{238}U line at 4.2 MeV line is not in secular equilibrium with the ^{210}Po line at 5.4 MeV; the ^{238}U chain could therefore be broken. The ^{232}Th chain, on the other hand, seems to be in secular equilibrium. In the energy spectrum summed over all the natural crystals working in MiDBD-I we have also observed the presence of the nuclear recoil peak at $\sim$ 100 keV, relative to the ^{210}Po decay, with an intensity comparable to that of the corresponding 5.3 MeV alpha peak. In the energy spectrum obtained with the data collected in the second run the high contribution at low energy due to tellurium activation prevent us from seeing the recoil peak at 100 keV.

A clear reduction in both continuum and γ/α peaks intensities is observed in MiDBD-II with respect to the first run (Fig. (6.6) and Tab. (6.7)). In particular a reduction factor of about two is observed for the ^{238}U and ^{232}Th alpha and gamma peaks and for the 3-4 MeV continuum. A reduction of a factor of about 1.5 is observed in the gamma continuum between 1 and 3 MeV (including the DBD0ν region). A higher reduction factor of $\sim$ 4 is obtained for the 5.3 and 5.4 MeV peaks of ^{210}Po.

The background reduction obtained in the second run (Tab. 6.7), both for the intensities of gamma and alpha lines and for the continuum between 3 and 4 MeV, proves the effectiveness of the changes applied in MiDBD-II (increased roman lead shields and cleaning procedure applied to crystals and

E (keV)	Isotope	MiDBD-I counts/h/kg	MiDBD-II counts/h/kg	CUORICINO ($5\times5\times5$ cm^3) counts/h/kg
88	123mTe+127mTe		5.62E-01± 2.37E-02	1.33E-02 ± 1.63E-03
105	129mTe		1.12E-01± 1.05E-02	
145	125mTe	1.25E-02 ± 3.14E-03	5.69E-01± 2.31E-02	1.61E-02 ± 1.57E-03
238	212Pb	2.02E-02 ± 2.93E-03		9.38E-03 ± 1.46E-03
241	214Pb	5.64E-03 ± 1.70E-03		2.25E-03 ± 1.97E-03
247	123mTe		2.43E-01± 1.82E-02	7.23E-03 ± 1.59E-03
294	214Pb	9.50E-03 ± 2.16E-03	7.43E-02± 8.80E-03	1.39E-02 ± 1.61E-03
337	228Ac	5.09E-03 ± 1.74E-03		
351	214Pb	1.45E-02 ± 2.63E-03		6.80E-03 ± 1.27E-03
583	208Tl	1.35E-02 ± 1.53E-03	< 1.18E-02	1.44E-02 ± 1.52E-03
603	121mTe+121Te	3.94E-03 ± 1.19E-03	3.41E-02± 7.15E-03	3.75E-03 ± 1.03E-03
609	214Bi	9.24E-03 ± 1.40E-03		1.60E-02 ± 1.42E-03
728	212Bi	4.71E-03 ± 1.31E-03		1.54E-03 ± 8.55E-04
752	228Ac		7.15E-03± 3.30E-03	
768.4	214Bi			
804	210Po	4.11E-03 ± 1.10E-03	< 5.88E-03	9.46E-03 ± 9.24E-04
911	228Ac	1.39E-02 ± 1.27E-03	< 6.76E-03	6.06E-03 ± 9.75E-04
934	214Bi	2.25E-03 ± 7.63E-04		
965	228Ac	2.97E-03 ± 8.48E-04		
970	228Ac	6.91E-03 ± 9.75E-04	< 1.03E-02	
1002	238U(234mPa)	1.78E-03 ± 7.21E-04		
1120	214Bi	4.41E-03 ± 7.63E-04	< 4.41E-03	1.34E-02 ± 9.06E-04
1156	214Bi	1.65E-03 ± 6.78E-04		
1173	60Co	2.45E-02 ± 1.57E-03	1.49E-02± 4.95E-03	1.85E-02 ± 9.68E-04
1238.2	214Bi			5.85E-03 ± 6.28E-04
1333	60Co	2.21E-02 ± 1.91E-03	1.16E-02± 3.85E-03	1.90E-02 ± 9.29E-04
1461	40K	9.73E-02 ± 3.43E-03	1.73E-02± 4.79E-03	3.98E-02 ± 1.24E-03
1509.5	214Bi			2.37E-03 ± 4.72E-04
1590	228Ac	3.18E-03 ± 5.94E-04		
1628	228Ac	2.04E-03 ± 5.09E-04		
1661.5	214Bi			1.05E-03 ± 3.45E-04
1731	214Bi	7.21E-04 ± 3.82E-04		3.67E-03 ± 5.26E-04
1766	214Bi	5.98E-03 ± 8.48E-04	< 3.24E-03	1.75E-02 ± 8.23E-04
1847.7	214Bi			2.29E-03 ± 3.72E-04
2104	208Tl(f.s.)	2.59E-03 ± 5.94E-04	3.85E-03± 1.65E-03	1.11E-03 ± 2.57E-04
2118.9	214Bi			1.61E-03 ± 2.93E-04
2203	214Bi	1.65E-03 ± 4.66E-04		5.56E-03 ± 4.67E-04
2448	214Bi			1.94E-03 ± 3.01E-04
2615	208Tl	1.49E-02 ± 1.36E-03	4.95E-03± 2.20E-03	9.16E-03 ± 5.71E-04

Table 6.5: *Intensities of the observed gamma lines for MiDBD-I, MiDBD-II and CUORICINO.*

copper surfaces) and can provide useful informations to localize the main background sources.

natural crystals					
	3-4 MeV continuum [c/keV/h 10^{-5}]	4.1 MeV 232 Th [c/h 10^{-1}]	4.3 MeV 238 U [c/h 10^{-1}]	4.8 MeV 238 U [c/h 10^{-1}]	5.3 + 5.4 MeV Po [c/h 10^{-1}]
MiDBD-I	1.9+/-0.1	0.063+/-0.001	0.29+/-0.01	0.79+/-0.03	1.8+/-0.1
MiDBD-II	0.9+/-0.1 S	0.033+/-0.003	0.17+/-0.02	0.30+/-0.03	0.47+/-0.04
enriched crystals					
	3-4 MeV continuum [c/keV/h 10^{-5}]	4.1 MeV 232 Th [c/h 10^{-1}]	4.3 MeV 238 U [c/h 10^{-1}]	4.8 MeV 238 U [c/h 10^{-1}]	5.3 + 5.4 MeV Po [c/h 10^{-1}]
MiDBD-I					
130	5.5+/-0.3	0.71+/-0.04	2.63+/-0.09	3.22+/-0.11	0.48+/-0.03 + 8.0+/-0.2
128		1.51+/-0.08	6.98+/-0.22	8.08+/-0.28	1.1+/-0.1 + 23.0+/-0.4
MiDBD-II					
130	3.1+/-0.7	0.23+/-0.02	1.6+/-0.1	1.6+/-0.1	0.9+/-0.1
128	3.5+/-0.7	0.30+/-0.02	2.3+/-0.2	2.0+/-0.2	0.7+/-0.1

Table 6.6: *Background integrals for the continuum between 3 and 4 MeV and the alpha peaks for natural (top) and enriched (bottom) crystals in MiDBD-I and MiDBD-II.*

Reduction factors - peaks			
U and Th γ's	^{60}Co	^{40}K	U and Th α's
≥ 2	~ 2	~ 6	~ 2
Reduction factors - continuum			
[1 - 2] MeV	[2 - 3] MeV	DBD region	[3 - 4] MeV
~ 1.3	~ 1.6	1.5 ± 0.3	~ 2.4

Table 6.7: *Background reduction factors measured between the two runs of MiDBD.*

6.4 Background analysis

A semi-quantitative analysis of the measured background was carried out considering only MiDBD-I data, for which the available statistics was more significative. As quoted in chapter (5) the analysis is performed in three separate steps, attempted to identify the sources responsible of the alpha peaks in the first step, of the continuum above 3 MeV in the second, and of the gamma lines and continuum in the last step.

Alpha peaks

The alpha peaks visible in the background spectra above 3 MeV, clearly show the presence of con-taminations of ^{238}U , ^{210}Pb and ^{232}Th that in principle could be localized in the crystals bulk, in the crystals surface and on the surface of materials facing the detectors themselves.

By analyzing the peaks shape and position, the coincidence spectrum and the scatter plots we could conclude that these peaks are due to a surface (and not a bulk) contamination of the crystals. Indeed the peaks energy position corresponds to the transition energies of the decay, implying that

both the alpha particle and the nuclear recoil contribute to the signal: the decaying atoms can only be "contained" in the crystal. The shape of the alpha peaks observed is clearly non gaussian with an energy tail extending to low energies. This low energy tail indicates that the contamination producing the peak is localized on the crystal surface. The observed shape of the alpha peaks is well reproduced by Montecarlo spectra generated for contamination of the crystals surface between .1 and 1 μm.

The straight lines clearly visible in the scatter plot in Fig. (6.7) unequivocally indicate the presence of contaminations on the crystals surface. Alpha particles or nuclear recoils, emitted in a decay occurring very near to the surface, can in fact loose part of their energy outside the crystal and can therefore be detected by a faced detector.
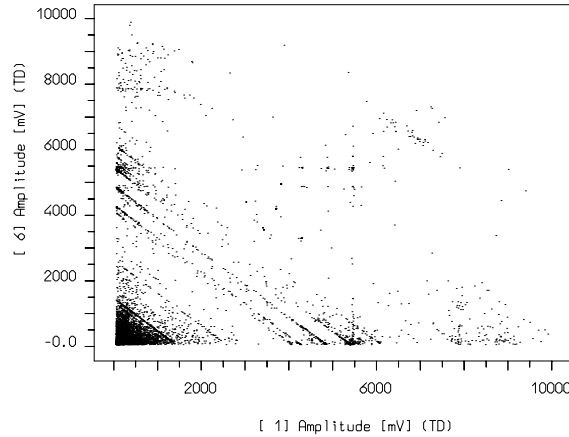
Figure 6.7: *Scatter plot of coincident events between all possible MiDBD-I detectors.*

By comparing the measured scatter plots with the ones simulated for different depths and density profiles for surface contaminations of the crystals, we concluded that the distribution of the coincidence events on the plots are better reproduced for contaminations on the crystals surface with a depth between .1 and 1 μm with exponential density profile. In this case, in fact, the events are distributed over all the lenght of the straight lines, but with a higher density near the borders (Fig. 6.8).

An additional proof of the existence of surface contaminations of the crystals is the presence of the alpha peaks in the coincidence spectrum, obtained by plotting events with multiplicity 2 (i.e. events in which 2 facing crystals are simultaneously hit).

In order to verify the indications of high contributions to alpha peaks from surface contaminations, independent measurements were carried on in the hall C of LNGS. These measurements showed that the intensity of the alpha peaks is decreased if the crystals surface is polished with powders with lower radioactivity than the ones used by the crystals factory in China or alternatively if it is subjected to an etching procedure (Fig. 6.9). The same results have been obtained after the polishing of the surfaces of the 20 crystals of the array for MiDBD-II (Fig. 6.6(right)).

These preliminary considerations helped us in identifying the possible sources of the alpha peaks as ^{238}U , ^{210}Pb , ^{232}Th and ^{238}U -^{230}Th (^{238}U broken chain) contaminations located on the crystals surfaces at a depth ranging between 0.1 and 1 μm with an exponential density profile. The Montecarlo spectra corresponding to these sources were then used as input to the mc2exp code in order to reproduce the measured background spectrum by a linear combination of simulated spectra. The radioactive sources, corresponding to the linear combination that better reproduces the observed spectrum in the alpha energy region, were therefore found. With this procedure we have identified
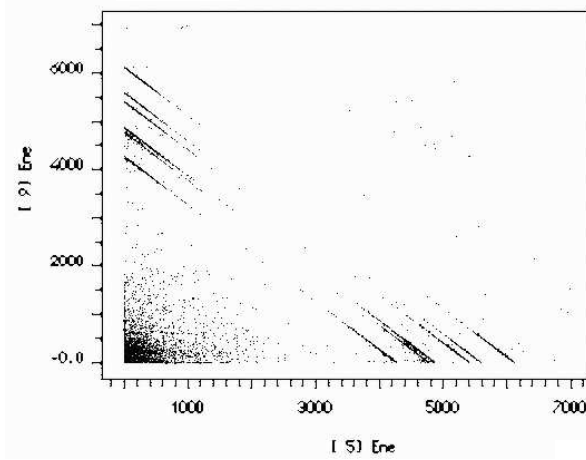
Figure 6.8: *Simulated scatter plot for ^{238}U contamination on the crystal surface at 1 μm depth with exponential density profile.*

the contaminations whose contribution to the measured background in this energy region is most relevant.

The identified sources are ^{238}U , ^{238}U -^{230}Th and ^{232}Th distributed with exponential density profile on the crystals surface at a depth ranging between 0.2 and 1 μm. This surface contamination can probably be ascribed to the highly contaminated polishing powders, used for the surface treatment of the MiDBD crystals (Tab. 4.3). The reduction in the alpha peaks intensity, observed in MiDBD-II, can therefore be ascribed to the crystals surface cleaning performed with selected low activity powders (Tab. 4.2). The evaluated contaminations of the crystals surfaces in ^{238}U and ^{232}Th cannot however account completely for the 5.4 and 5.3 MeV peaks of ^{210}Po. These peaks seems to be produced by the α or α+recoil particles, emitted by ^{210}Po, daughter of ^{210}Pb . Since, as quoted before, the counting rates of the two peaks are almost stable in time, the contamination responsible of the peaks must be ascribed to ^{210}Pb impurities. The analysis of the coincidence spectrum, where a clear peak at 5.3 MeV and another at ∼100 keV are observed, shows that part of he ^{210}Pb contamination must be located on the crystal surface. The comparison with the Montecarlo spectra obtained for ^{210}Pb contaminations on the crystal surface at different depths, suggest a very shallow impurity distribution to account for the nuclear recoil peak at ∼100 keV. Normalizing the simulated spectrum in order to completely account for this peak, we have noticed that some contribution is still missing to the 5.3 MeV peak in the anticoincidence spectrum. A surface contamination of the passive materials facing the crystals (mainly copper of the mounting structure) at a depth between 0.2-1 μm has been found to fit properly the missing contribution. Such surface contaminations of ^{210}Pb could be ascribed to a deposition in ^{210}Pb produced by Rn decays occurred during the crystals handling. Indeed in this case a contamination in a very thin layer could be produced on surfaces exposed to Rn.

A weak indication of a low intensity peak at 3250 KeV is also present in the background spectrum. This peak is probably due to a ^{190}Pt contamination of the crystals. Indeed the crucibles in which the TeO$_2$ crystals are grown, are made of this material and inclusions in the crystal of small fragments of ^{190}Pt are therefore possible. The isotope ^{190}Pt decays via alpha emission with a lifetime of 6.5×10^{11}y and the transition energy is 3249 MeV, that is compatible with the measured peak position. The shape of the peak appears to be simmetric and no indication of coincidence events are

83
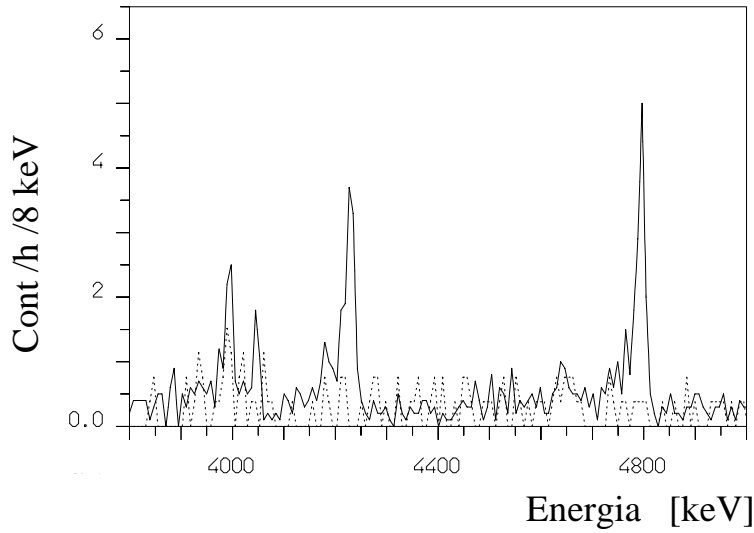
Figure 6.9: *Comparison between background spectra measured in hall C with TeO$_2$ crystals before (continuous line) and after (dashed line) etching procedure.*

found, pointing to the conclusion that the contamination should be in the crystals bulk. [190]Pt is the only contribution from crystals bulk contaminations found to be necessary to reproduce the anticoincidence background spectrum. Recent ICPMS measurements performed on small fragments of the TeO$_2$ crystals have not revealed the presence of this contaminant. This fact excludes the presence of a uniform contamination of [190]Pt in the crystals bulk, but a not uniform distribution of [190]Pt atoms in the crystals volume is however possible.

With the adopted analysis procedure we were able to find the best linear combination of radioactive sources able to account for the alpha peaks intensities measured in the background spectrum (Fig. 6.10) and at the same time we could evaluate the contribution at lower energies arising from the so far identified contaminations. In particular this sources can partially (but not completely) account for the rather flat continuous background measured between 3 and 4 MeV, a region where no known γ nor α lines from natural and cosmogenic radioactivity are present. By the analysis of the coincident events from α particles we obtained a rate R$_D$=0.13 counts/keV/kg/y, in the 3-4 MeV interval, for the events with multiplicity 2 (i.e. events in which 2 crystals are simultaneously hit). The only possible origin for these events, is a radioactive decay produced in the fraction of crystal surface facing other crystals (S$_{Active}$). On the other hand, the decays occurring in the fraction of crystal surface (S$_{Inert}$) which faces inert materials (e.g. copper), would contribute to the anticoincidence background spectrum. By simply considering the geometric evaluation of the ratio S$_{Inert}$/S$_{Active}$ (average Montecarlo evaluation) we can obtain from R$_D$ the expected contribution to the anticoincidence spectrum in the 3–4 MeV region: 0.16$\pm$ 0.05 counts/keV/kg/y. In order to extrapolate this rate back to the DBD0ν region we need to know the shape of the background spectrum. In particular, various estimates of the ratio R$^s_{3-4}$/R$^s_{\beta\beta}$ (where R^s are the counting rates in the energy regions of interest after the anticoincidence cut) were obtained on the basis of Montecarlo simulations of crystal surface contaminations of different depths and density profiles. Unfortunately the ratio depends critically on these parameters and the average Montecarlo evaluation of the ratio has therefore a large error. The extrapolated contribution to the DBD0ν region background is 0.27$\pm$ 0.1 counts/keV/kg/y corresponding to $\sim$46$\pm$ 10% of the measured rate.
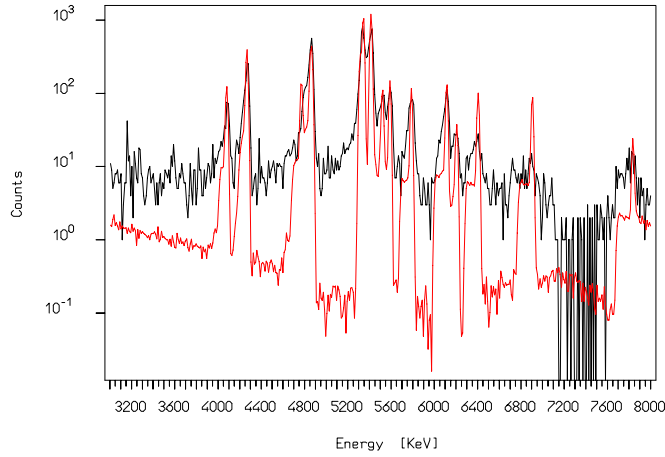
Figure 6.10: *Comparison between measured spectrum (black) and the Montecarlo spectrum (red) obtained like the best linear combination of the simulated spectra, that reproduces the alpha peaks intensities and shapes.*

3-4 MeV energy region

As quoted above, the sources responsible of the alpha peaks cannot completely account for the rather flat continuous background, measured above 3 MeV, and in particular above 3 MeV.

Other possible sources for this background were taken into account and excluded as relevant for MiDBD: neutrons (ruled out since no variation of the background rates measured with and without the neutron shield was observed), muon induced neutrons (ruled out by simulation of the production rate of neutrons in the experimental set up), bulk contamination of other components close to the detectors (such as the Teflon spacers placed between the copper frame and the crystals, the NTD thermistors, the Si heaters, for which the contamination, measured with Ge γ spectroscopy, seems to be too low to account for the observed background, even if more accurate and sensitive measurements are needed). Finally, some tests done with dedicated detectors in the hall C set-up, proved that the etching of the copper structure in a clean environment yields a reduction of the background in the 3-4 MeV region, while the cleaning of the crystals surface, gives a reduction in the alpha peaks intensity but does not give any change in the 3÷4 MeV energy region rate.

This fact, and the agreement of the Montecarlo simulations with the measured spectra, indicate that ^{238}U or ^{232}Th or ^{210}Pb surface contamination of the copper should be the missing background source (Fig. 6.11(top)). In fact, by applying the fit procedure to the energy range between 3 and 10 MeV, we have found that the best agreement with the experimental spectrum is obtained for ^{238}U , ^{232}Th and ^{210}Pb surface contamination of the copper structure and holder at a depth or the order of 1-5 μm (Fig. 6.11(bottom)). The absence of "external alpha peaks" in the background spectrum (apart the 5.3 MeV ^{210}Po peak about which we have quoted above) is in fact a clear indication of a not too shallow contamination depth (deeper than 1 μm). There is some difference in the shape of the spectra generated for contaminations in a 1μm or 5μm depth surface layer (Fig. 5.9(left)), but this difference does not seem significant, since the fit procedure chooses one or the other contamination indifferently. In addition the shape of the background above 3 MeV generated by 1-5 μm depth contaminations of the copper surfaces does not change so much when choosing ^{238}U , ^{232}Th or ^{210}Pb sources and therefore the three of them or, more likely, a combination of them, could be the
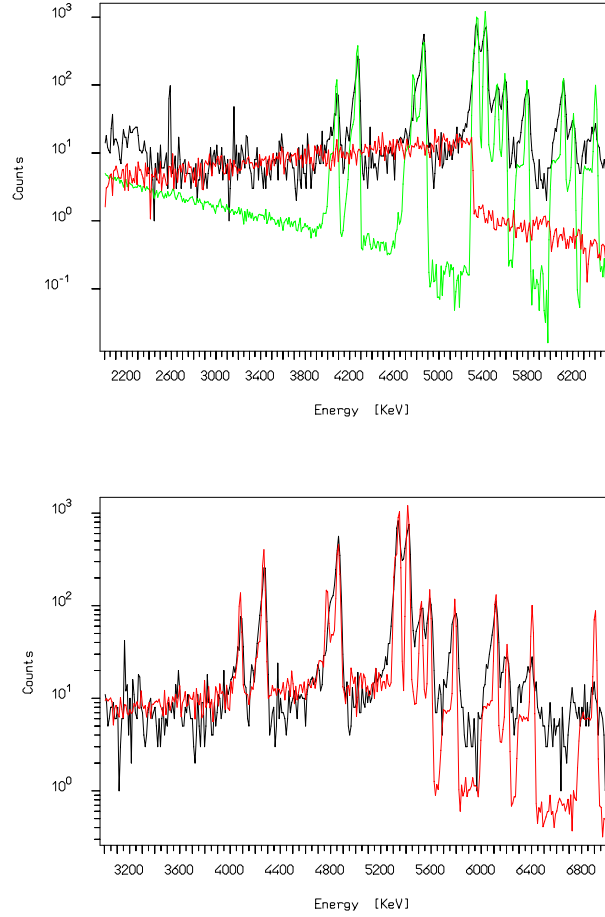
Figure 6.11: *Top: Comparison between measured spectrum (black) and Montecarlo spectra obtained as linear combination of simulated spectra that better reproduce the alpha peaks (green) and the continuum above 3 MeV(red). Bottom:comparison between measured spectrum (black) and Montecarlo spectra obtained as linear combination of simulated spectra that better reproduce the alpha peaks and the continuum above 3 MeV (red).*

responsible of the measured background between 3 and 4 MeV.

Since a direct check of the reliability of the obtained results is not available, dedicated and independent measurements are necessary to find out the contamination levels of the surface of copper and of the other parts facing the detectors and at the same time the nature and the depth of such contaminations. Other sources of flat background in the 3-4 MeV energy region could in fact have not been taken into account. Independent measurements to confirm or reject our hypothesis are therefore of fundamental importance also to better focalize our efforts in material selection, radiation shieldings and surface cleaning optimization.

The contribution of copper surface contaminations (after the anticoincidence cut) to the rate in the 3÷4 MeV energy region can be evaluated by subtracting the crystal surface contribution to the total rate: 0.33 ± 0.1 counts/keV/kg/y. Once again the extrapolation to the DBD0ν region is model dependent (it depends on the chosen contamination depth and nature). With our model the contribution of the copper surface contamination to the DBD0ν region background is 0.2 ± 0.1 counts/keV/kg/y ($\sim 34 \pm 10\%$).
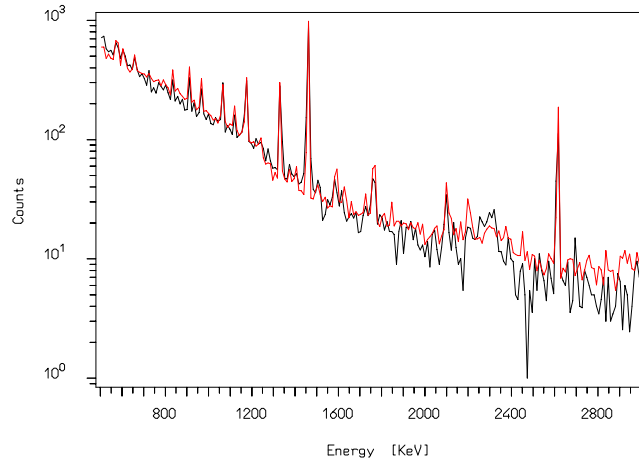
Figure 6.12: *Comparison in the gamma region between measured spectrum (black) and Montecarlo spectra obtained as linear combination of simulated spectra that better reproduce the entire energy range.*

Gamma region

The spectrum resulting from the best fit of the alpha region is used, together with the Montecarlo spectra generated for contaminations that contribute to the energy region below 3 MeV, to fit the experimental spectrum in the entire energy range (Fig. 6.12). With this procedure we have tried to reproduce also the background measured in the gamma energy region.

^{40}K contaminations on the crystals and copper surfaces were considered in order to account for the 1460 keV line. Bulk contaminations in the crystals are also possible sources of ^{40}K but they would generate a peak at 1463 keV. The 3 keV energy difference from the nominal value is due to the inclusion of a 3 keV X-ray, that for decays occurring in the crystals bulk has a small probability to escape from the detector. This fact doesn't exclude ^{40}K bulk contaminations of the crystals as a possible source, but give indications of the fact that it shouldn't be the dominant contribution to the ^{40}K peak at 1460 keV. In addition the detection of the electron associated to the beta decay would increase the continuum in the energy spectrum to a level higher than the measured one. High contribution to the background due to ^{40}K bulk contaminations of the crystals must therefore be exscluded. Bulk ^{40}K contaminations of the other experimental materials can also contribute to the 1460 keV line intensity and are therefore considered as possible sources.

Other sources we have taken into account are bulk contaminations in ^{238}U , ^{232}Th , ^{210}Pb of all the copper experimental parts (copper holder and mounting structure, thermal shields, cryostat shields), in the internal roman lead shield and also in 10 cm of the external lead shield (we have limited our analysis to 10 cm because the simulation of deeper contamination in the external lead shield would have required too much time in order to obtain a good statistics). Bulk contaminations of ^{60}Co due to cosmogenic activation in the crystals and in the copper parts were also considered as possible sources of background. The fluxes of environmental radioactivity measured in the LNGS have also been taken into account. The evaluated contribution to the measured background due to this source has been evaluated to be negligible.

The analysis of the measured background spectrum in the entire energy range (i.e. 10 keV-10 MeV) by means of the minimization procedure (mc2exp) performed taking into account all the above quoted radioactive sources, led to the following conclusions:

- the threshold energy region (i.e. between 10 and 100 keV) seems to be dominated by a ^{210}Pb surface contamination located either on the crystals surface and on the Cu mounting box surface. This contamination is clearly identified on the basis of the 46 keV peak and of the 5.3 and 5.4 MeV alpha lines, whose intensities are compatible with ^{210}Pb contamination not in secular equilibrium with the ^{238}U chain;

- the continuum in the energy region between 100 and 1500 keV seems to be determined by a ^{40}K surface contamination of the crystals and/or of the copper mounting structure and holder;

- the gamma peaks above ∼ 500 keV of the ^{238}U and ^{232}Th chains and the two ^{60}Co peaks at 1173 and 1332 keV are mainly due to sources outside the detector. This result is confirmed by the reduction observed in the peaks intensity after the increasing of the roman lead shield in the second run of the experiment (Tab. 6.7). The value of the environmental gamma flux in the underground laboratory, measured with Ge detector just close to our experimental setup led us to rule out this possible source for the high energy gamma lines arising from ^{238}U and ^{232}Th chains. According to the Montecarlo simulation, the contamination responsible for these peaks could reasonably be the sum of the contamination of the external lead shield and of the various thermal shields that surround our detector.

- the alpha peaks of the ^{238}U and ^{232}Th chains, clearly visible in the background spectrum above 4 MeV, can be ascribed to surface contamination of the crystals. The reduction observed in their intensities in the second run is coherent with the surface treatment of the crystals;

- ^{238}U and ^{232}Th gamma peaks below ∼ 500 keV are ascribed to surface contaminations of the copper mounting structure;

- low intensities gamma lines of rather short living isotopes are explained by the cosmogenic activation of both copper and tellurium.

- sources responsible of the background measured in the DBD0ν energy region are ^{238}U , ^{238}U - ^{230}Th, and ^{232}Th surface contaminations of the crystals and of the copper holder and mounting structure (alpha, beta and gamma emissions from these chains contribute to the background) and ^{232}Th contaminations external to the detector structure (only the gamma emission from this chain can contribute to the background in the DBD0ν region, mainly through the 2615 keV line of ^{208}Tl).

According to our Montecarlo simulation of the MiDBD detectors, the foregoing sources can completely account for the observed background (peaks and continuum), measured in the two runs.

The contribution to the DBD0ν energy region arising from ^{232}Th contaminations external to the detector structure is evaluated on the basis of the calibration spectrum obtained with an external ^{232}Th source located just outside the cryostat. The shape of the calibration spectrum is in fact in good agreement with the shape of the simulated spectra for radioactive ^{232}Th contaminations distributed over the cryostat thermal shields. The ratio between the area of ^{208}Tl line at 2615 keV and the integral in the DBD0ν region observed in calibration is 14± 2. When compared with the 2615 keV rate observed in the background spectrum (129 counts/kg/y), this translates into a contribution of 0.11 counts/keV/kg/y which is ∼20% of the total DBD0ν background rate.

In Fig. (6.13) the contribution to the DBD0ν energy region from the contamination responsible for the alpha peaks (blue), for the continuum above 3 MeV (red) and for the gamma region background (green) are shown. The results of the performed analysis are summarized in Tab.(6.8). The clear correlation between the reduction factors in the DBD0ν and in the 3-4 MeV energy regions,
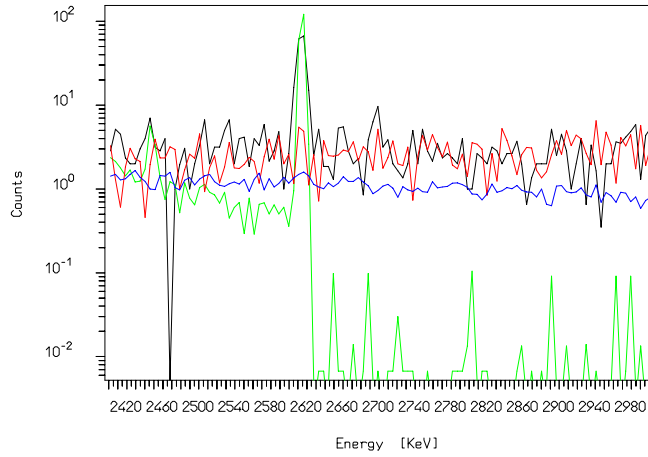
Figure 6.13: *Different contributions to the DBD0ν energy region background: contamination responsible or the alpha peaks(blue), for the continuum above 3 MeV (red) and for the gamma region background (green) are shown. In black the measured background in this region is shown.*

obtained after the surface treatments of the crystals and of the copper mounting structure and holder (Tab. 6.7) is a further prove of the reliability of the obtained results.

Table 6.8: *Estimate of the weight of the different sources responsible for the background measured in the MiDBD-I run.*

Source	^{208}Tl	DBD0ν region	3-4 MeV region
TeO$_2$ ^{238}U and ^{232}Th surface contamination	-	46± 10%	33± 10%
Cu ^{238}U and ^{232}Th surface contamination	∼10%	34± 10%	67± 20%
^{232}Th contamination of cryostat Cu shields	∼90%	20± 5%	-

6.5 Contamination levels for the experimental materials

The analysis performed up to now allowed us to obtain very useful results. Through it we have been able to identify the main sources responsible of the measured background and to evaluate the main contributions to the background in the different energy regions. As it was explained in section (5.6) the quantitative values of the contamination levels of the various experimental parts and materials that we can obtain from this procedure, are strongly dependent on the simulated spectra used to reproduce the the experimental spetrum.

For this reasons we have evaluated upper values for the 90% C.L. limits for bulk and surface contaminations in ^{238}U , ^{232}Th , ^{40}K , ^{60}Co and ^{210}Pb of the TeO$_2$ crystals, the copper and the roman lead used in MiDBD-I and MiDBD-II by direct comparison between measured and simulated spectrum for each contaminant in each experimental part (Tab. 6.9).

89

Bulk contaminations

	TeO$_2$					Copper				Roman lead			
	^{232}Th	^{238}U	^{40}K	^{60}Co	^{210}Pb	^{232}Th	^{238}U	^{40}K	^{60}Co	^{232}Th	^{238}U	^{40}K	^{210}Pb
	pg/g	pg/g	pg/g	μBq/kg	μBq/kg	pg/g	pg/g	pg/g	μBq/kg	pg/g	pg/g	pg/g	mBq/kg
MiDBD-I	<1.2	<0.8	<2.5	<238	<78	<36	<5.7	<30	<237	<27	<10	<19	<360
MiDBD-II	<0.6	<0.1	<1.5	<167	<15	<14	<5.5	<8.2	<187	<12	<3	<2.8	<245

Surface contaminations

	TeO$_2$				Copper			
	^{232}Th	^{238}U	^{40}K	^{210}Pb	^{232}Th	^{238}U	^{40}K	^{210}Pb
	μBq/cm^2	μBq/cm^2	μBq/cm^2	μBq/cm^2	μBq/cm^2	μBq/cm^2	μBq/cm^2	μBq/cm^2
MiDBD-I	<0.04	<0.07	<5.9	<0.4	<0.2	<0.14	<13.6	<1
MiDBD-II	<0.02	<0.07	<3	<0.08	<0.09	<0.07	<3.6	<0.6

Table 6.9: *Estimate of the upper 90% C.L. limits for bulk and surface contaminations of TeO$_2$ crystals, copper and roman lead used in MiDBD-I and MiDBD-II.*

Chapter 7

Cuoricino background analysis

Introduction

The experience gained with MiDBD-I, MiDBD-II and with the R&D carried out in the hall C of LNGS, with respect to detector optimization and background identification and reduction, was of fundamental importance for the following bigger experiment CUORICINO. As already quoted, while being a self-consistent experiment for the DBD research, CUORICINO finds its place in the CUORE project as a test facility intended to verify the technical feasibility of CUORE. The particular care devoted to materials selection and surfaces cleaning makes CUORICINO also a fundamental test with respect to background understanding and reduction.

7.1 Data and detector performances

CUORICINO was cooled down at the beginning of 2003. During the cooling procedure some of the signal wires disconnected so that in the first run only 32 of the large crystals and 16 of the small ones could be read, resulting in an active mass of 8.73 kg of ^{130}Te .

The performance in the first run of the electrically connected detectors was quite good: the average FWHM resolution measured during the calibration of the detectors with a ^{232}Th source was ~ 7 keV for the big crystals, and ~ 9 keV for the small crystals. Both these values were measured on the ^{208}Tl gamma line at 2615 keV. An evaluation of the average FWHM resolution at low energy in a calibration measurement is not possible since the radioactive source used for calibration is located far away from the detectors and low energy gammas arre absorbed before reaching them. The sum calibration spectra of all the operating large and small crystals are shown in Fig.(7.1).
The detectors response and FWHM, evaluated in calibration, are shown in Tab. (7.1) and Tab. (7.2). The distributions of the single detector energy responses and of the energy resolutions are shown in Fig. (7.2). In spite of the larger mass, the detector performances measured in CUORICINO are comparable to the ones obtained in the MiDBD experiment. We would have expected a worsening in the energy resolution due to the larger mass of the detectors. An increase of the detector mass implies in fact an increase of the heat capacity and hence a reduction of the signal amplitude. The performances measured for the CUORICINO $5\times5\times5$ cm^3 detectors have shown that this fact influences only marginally the energy resolution in the DBD0ν energy region.

On April 19th 2003 the first background measurement started. The live time was $\sim 72\%$, including the time required for the periodic calibration (usually every 15 days) of the detectors. The performance of the large size crystals during the entire run was quite good but three detectors that have not been used to compute the background. Indeed two detectors showed cross talk and a third
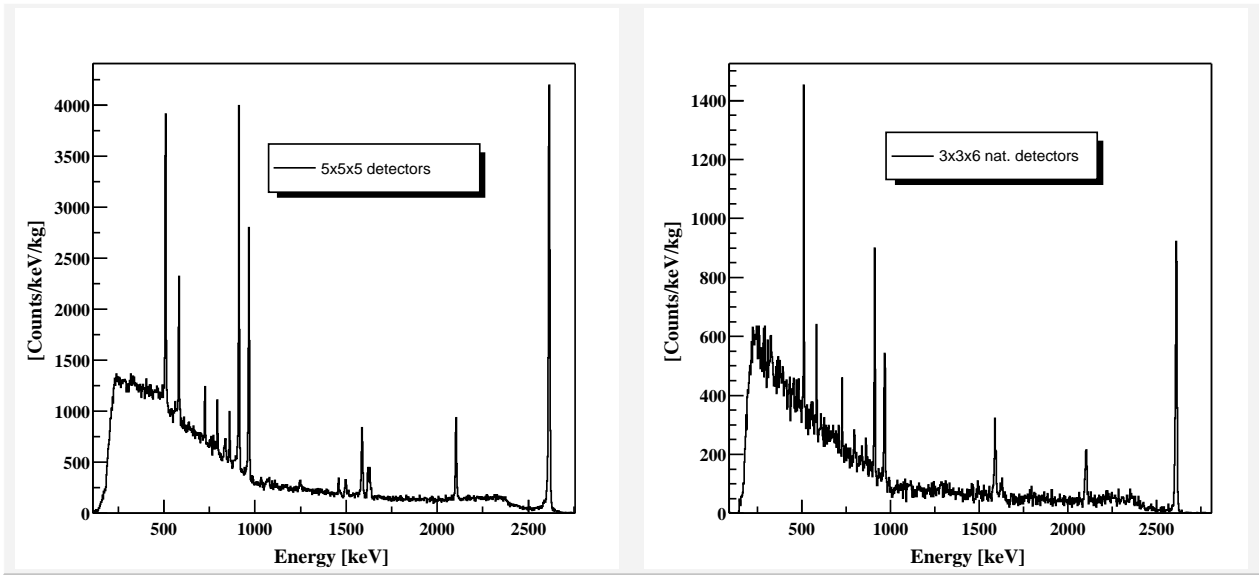
Figure 7.1: *Summed calibration spectrum (^{232}Th source just outside the cryostat) from all the operating $5 \times 5 \times 5$ cm^3 and $3 \times 3 \times 6$ cm^3 crystals.*

had excessive spurious noise. Therefore we used only 29 of the large crystals for background studies. As respect to the small crystals, one detector showed a variation in the reference pulse position after some weeks of measuring and one of the two central detectors had its Si heater disconnected. Therefore the number of well-working $3 \times 3 \times 6$ cm^3 detectors was reduced to 11 natural crystals and 4 enriched ones.

At the end of October 2003 CUORICINO was stopped to undergo substantial operations of maintenance and to recover the lost electrical connections and hence increase the number of working detectors. The technical problem responsible for the disconnection of the wires was identified and in November 2003 the array was warmed to room temperature to repair the lost connections. The disconnected wires were recovered, and some cryogenic problem solved. These operations required a few months and at the end of April CUORICINO started taking data again. Unfortunately two of the $5 \times 5 \times 5$ cm^3 crystal wire connections had broken during the cooling down. Actually we have 42 big crystals over 44 and all the 18 small crystals working. The active mass actually working corresponds therefore to 11.3 kg of ^{130}Te .Unfortunately two $5 \times 5 \times 5$ cm^3 and one $3 \times 3 \times 6$ cm^3 crystals cannot be computed to evaluate the background. One big crystal has in fact high spurious noise, while another $5 \times 5 \times 5$ cm^3 crystal and one $3 \times 3 \times 6$ cm^3 crystal have the silicon heater disconnected. The disconnected Si heater could not be in fact restored, since this operation would have required the opening of the entire tower copper box. Therefore the number of well-working detectors was reduced to 40 over 44 $5 \times 5 \times 5$ cm^3 crystals and 13 natural and 4 enriched over 18 $3 \times 3 \times 6$ cm^3 crystals.

The collected statistics in this second run is 1.35 kg·y for the $5 \times 5 \times 5$ cm^3 and 0.19 kg·y for the $3 \times 3 \times 6$ cm^3 crystals respectively. The average FWHM resolution measured during the calibration of the detectors with a ^{232}Th source was ~ 8 keV for the big crystals, and ~ 11 keV for the small crystals. The performance of the detectors during the second run are summarized in Tab. (7.1) and (7.2) and the distributions of the pulse height and average FWHM (calculated at the 2615 keV calibration line) evaluated for the $5 \times 5 \times 5$ cm^3 and the $3 \times 3 \times 6$ cm^3 crystals are shown Fig. (7.4).

5x5x5 CUORICINO crystals - runI		
crystal	Pulse height*kg μV/MeV*kg	FWHM(@2615) keV
B15	185	14
B47	130	17.2
B7	152	7.3
B60	77	7.5
B56	102	6.4
B46	60	7.1
B28	50	7.2
B42	46	6.8
B29	133	5.1
B27	38	7.7
B44	220	6
B51	103	9.8
B36	56	8.8
B18	104	7
B13	100	7
B55	138	10.2
B16	277	6.2
B54	222	5.6
B31	198	5.6
B12	46	7.5
B52	286	7.2
B41	212	8.7
B57	50	7
B26	81	5.4
B10	102	5.8
B40	58	5.8
B37	41	11.9
B17	43	11.9
B45	52	5.3
B61	98	7.1
B53	237	5
B34	58	5.7

5x5x5 CUORICINO crystals - runII		
crystal	Pulse height*kg μV/MeV*kg	FWHM(@2615) keV
B60	88	9.91
B51	121	5.77
B62	69	4.93
B56	91	5.08
B43	331	8.86
B42	52	7.79
B23	61	7.95
B15	207	10.4
B31	245	5.96
B14	132	5.73
B24	115	5.34
B25	204	17.1
B47	137	
B46	67	7.07
B28	62	6.06
B29	151	9.42
B27	43	6.16
B40	69	7.28
B18	124	8.97
B13	106	7.77
B35	65	13.21
B55	147	7.47
B16	296	7.37
B30	234	7.61
B54	229	5.59
B32	207	8.23
B12	52	5.67
B52	216	5.83
B53	193	7.17
B41	212	16.17
B34	75	10.39
B57	49	
B36	44	11.6
B26	132	5.97
B17	50	11.5
B37	87	13.12
B49	71	19.69
B45	77	5.7
B61	119	7.79

Table 7.1: *Detector performances in the first (left) and in the second (right) run of CUORICINO for the 5x5x5 cm^3 crystals.*

3x3x6 CUORICINO crystals - runI			3x3x6 CUORICINO crystals - runII		
crystal	Pulse height*kg μV/MeV*kg	FWHM(@2615) keV	crystal	Pulse height*kg μV/MeV*kg	FWHM(@2615) keV
5	81	9.5	6	129	10
130-2	21	18.8	B	96	8.67
F	161	7.8	16	104	20
2	76	8.3	H	62	9.21
130-1	15	13.5	5	89	13.02
128-2	37	12.8	130-2	24	16.12
4	130	7.9	F	176	6.93
6	103	7.7	2	92	7.33
B	85	9.8	130-1	18	14.1
16	103	13.5	128-2	38	16.7
0	55	13.1	4	152	8.46
I	126	4.6	I	148	5.25
E	82	7.1	E	92	6.77
13	82	6.2	13	93	6.87
14	21		128-1	17	13.56
128-1	12	8.7	9	208	8.15
9	165	8.1	0	79	12.23

Table 7.2: *Detector performances in the first (left) and in the second (right) run of CUORICINO for the 3x3x6 cm³ crystals.*

7.2   DBD results

The effective exposure totalled with CUORICINO until June 2004 is of $\sim$4.76 kg·y and $\sim$0.53 kg·y for the $5\times5\times5$ cm^3 and the $3\times3\times6$ cm^3 crystals respectively. No peak appears in the anticoincidence background spectrum in correspondence of the ^{130}Te DBD0ν searched line at 2528 keV (see Fig. 7.5).

Using a Maximum Likelihood procedure [112, 3] to evaluate the maximum number of DBD0ν events compatible with the measured background, it was possible to set a lower limit on the ^{130}Te halflife for the DBD0ν of 1.0 x 10^{24} years at 90%C.L. The corresponding upper bound on the Majorana effective mass ranges from 0.26 to 1.45 eV depending on the QRPA nuclear model used to make the calculation (these models seem the most suitable for heavy nuclei). The reported data already show that CUORICINO is a competitive experiment in the field of Neutrinoless Double Beta Decay [116]. Once completely working CUORICINO will have a 5 year sensitivity (at 68% C.L.) of about 7.8 x 10^{24} year for the $\beta\beta(0\nu)$ of ^{130}Te . This means that CUORICINO will be able to test the Majorana mass in the 100-500 meV range.

7.3   Background results

The background spectra corresponding to the data collected in the first run of CUORICINO, on which the following analysis has been performed, are shown in Fig. (7.3) and Fig. (7.7). The gamma lines due to the single isotopes ^{60}Co, ^{40}K and to the ^{238}U and ^{232}Th chains are clearly visible. Also visible are the gamma lines due to Te activation (^{121}Te, ^{121m}Te, ^{123m}Te, ^{125m}Te and ^{127m}Te) and those

Figure 7.2: *Distribution of the single CUORICINO detector energy responses normalized to 1 kg of TeO$_2$ (left) and energy resolutions (FWHM) at the Tl^{208} 2615 keV line(right) in the first run.*
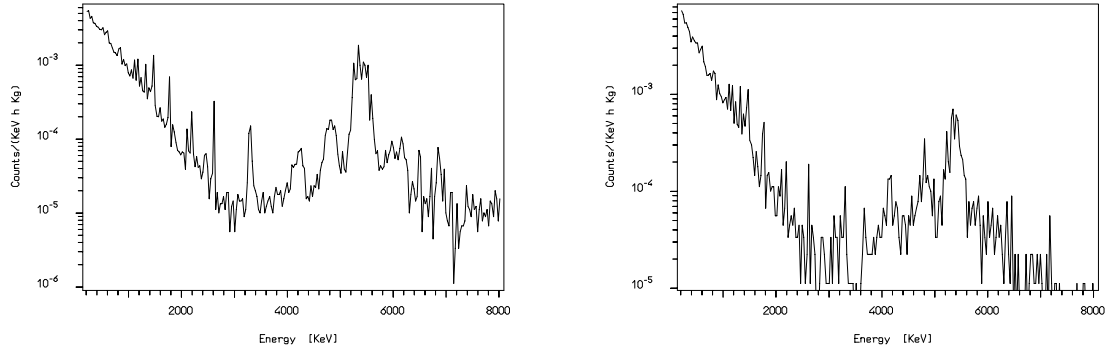
Figure 7.3: *Summed background spectra from the operating 5x5x5 cm^3 (left) and natural 3x3x6 cm^3 crystals (right).*

due to Cu activation (^{57}Co, ^{58}Co, ^{60}Co and ^{54}Mn) by cosmic ray neutrons while above ground.

The FWHM resolution of $5\times5\times5$ cm^3 detectors at low energy, as evaluated on the 122 keV gamma line of ^{57}Co, is $\sim$2.8 keV. The energy resolution in the DBD0ν energy region is evaluated on the 2615 keV line of ^{208}Tl , clearly visible in the background sum spectrum and it is 8.7 keV FWHM. The background in the DBD0ν region (i.e. 2510-2580 keV) is 0.19 $\pm$ 0.03 counts/keV/kg/y.

As respect to the $3\times3\times6$ cm^3 crystals the statistical accuracy is much less, nevertheless the gamma lines are clearly visible in the background sum spectrum. The FWHM resolution at low energy is $\sim$1.5 keV. The FWHM resolution on the ^{208}Tl gamma line at 2615 keV is evaluated to be of about 12 keV (this value has a large uncertainty due to the poor statistical significance of the peak). The background in the DBD0ν region (i.e. 2510-2580 keV) is 0.22 $\pm$ 0.1 counts/keV/kg/y.

Because of the low collected statistics, it's quite difficult to evaluate the possible background sources. It's however possible to extrapolate some considerations from the analysis of the sum spectra of the operating crystals.

The measured background spectra for the $5\times5\times5$ cm^3 and $3\times3\times6$ cm^3 CUORICINO crystals are compared in Fig. (7.7). General spectral shapes and counting rates (when normalized to the mass of the crystals) are quite similar. As respect to the gamma lines, as it can be seen from Tab.(7.3),
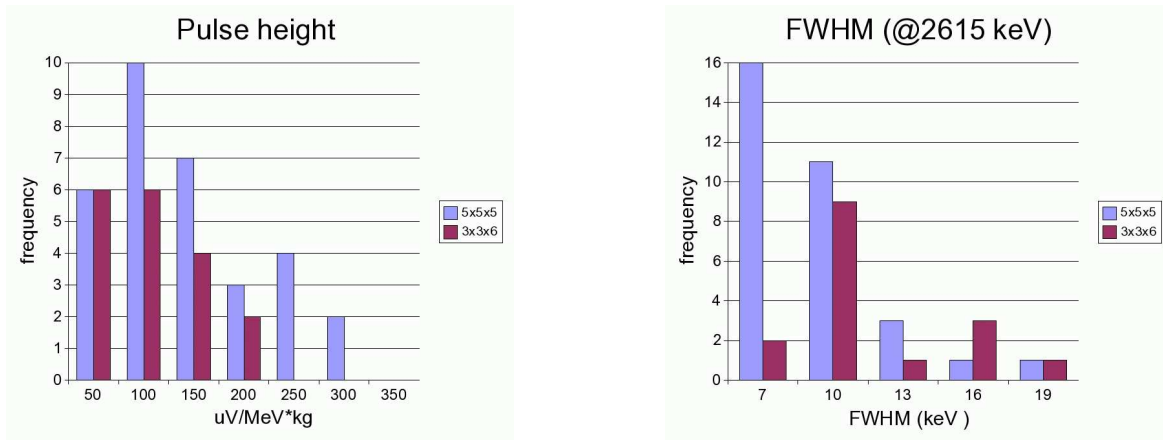
95
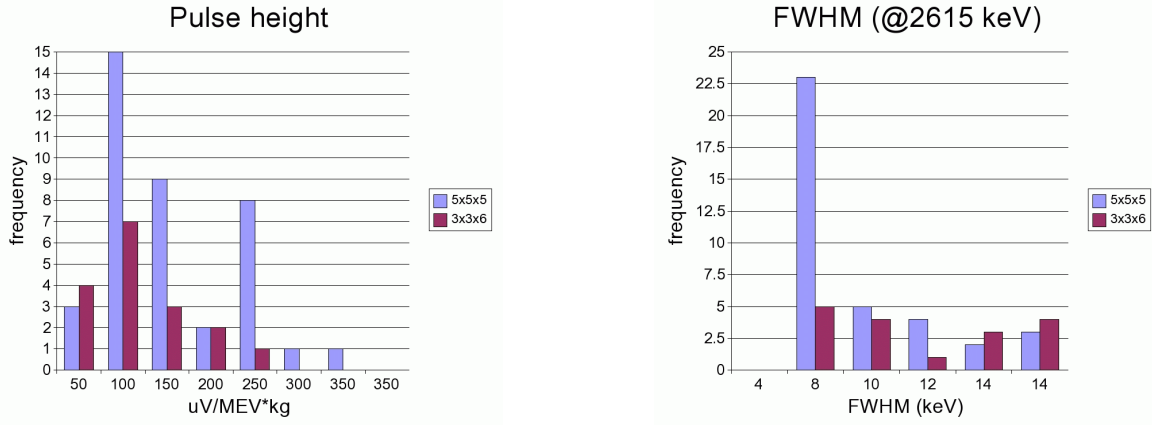
Figure 7.4: *Distribution of the single CUORICINO detector energy responses normalized to 1 kg of TeO$_2$ (left) and energy resolutions (FWHM) at the Tl^{208} 2615 keV line(right) in the second run.*

the ^{208}Tl 2615 keV line has and intensity per unit mass that scales with the Montecarlo calculated efficiency of the two kinds of detectors for contaminations localized in the external parts of the cryostat. The ^{40}K 1460 keV line and the two lines at 1173 and 1332 keV of ^{60}Co have compatible intensities per unit mass in the two kind of crystals. This difference in the behavior of the considered lines gives indication a different localization of the sources.

gamma lines		CUORICINO-5×5×5 cm^3	CUORICINO-3×3×6 cm^3
Energy(keV)	Isotope	c/h/kg	c/h/kg
1173	60Co	1.85E-02 $\pm$ 9.68E-04	1.58E-02 $\pm$ 4.53E-03
1333	60Co	1.90E-02 $\pm$ 9.29E-04	2.19E-02 $\pm$ 3.21E-03
1461	40K	3.98E-02 $\pm$ 1.24E-03	3.34E-02 $\pm$ 3.77E-03
1764	214Bi	1.75E-02 $\pm$ 8.23E-04	1.41E-02 $\pm$ 2.44E-03
2615	208Tl	9.16E-03 $\pm$ 5.71E-04	4.18E-03 $\pm$ 1.40E-03

Table 7.3: *Main gamma lines intensity of CUORICINO for the 5×5×5 cm^3 and the 3×3×6 cm^3 crysrtals*

In Fig. 7.7b the comparison between the background spectra of 5×5×5 cm^3 and 3×3×6 cm^3 CUORICINO crystals in the alpha region is shown. The background in this region seems to be a bit higher for the small crystals than for the big ones. In both the spectra is clearly visible a line at ∼3250 keV, due probably to a bulk contamination of the crystals in ^{190}Pt.

By comparing the measured background in MiDBD and CUORICINO it is possible to test the effectiveness of the modifications made in CUORICINO with respect to surface treatments and materials selection. In Tab. (6.5) the gamma lines intensity measured in CUORICINO, MiDBD-I and MiDBD-II are compared. Gamma peaks due to natural radioactivity of ^{232}Th , ^{238}U and ^{40}K have a higher intensity in CUORICINO, probably due to the reduced roman lead shield thickness. Also copper activation gamma lines have a higher intensity in CUORICINO, probably owing to the longer exposure to cosmic rays of the copper thermal shields of CUORICINO. On the contrary tellurium activation gamma lines have a smaller intensity in CUORICINO than in MiDBD-II, since much care has been devoted in CUORICINO to avoid a long exposition of the crystals to cosmic rays.

In Tab. 7.4 and Fig. (7.6) the counting rate in different energy regions and the background spectra
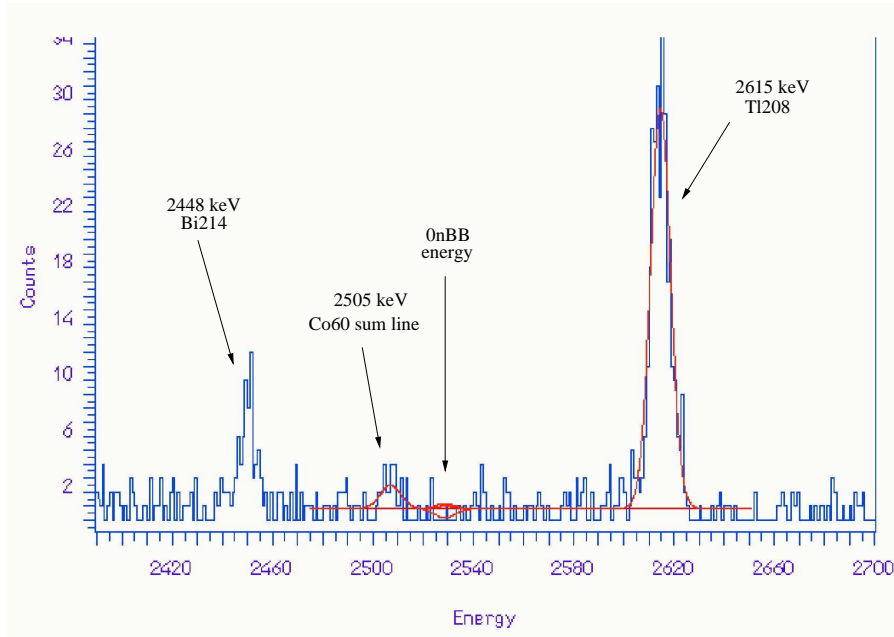
Figure 7.5: *Summed background spectrum from all the operating crystals in the region of neutrinoless double beta decay of* ^{130}*Te (Q-value=2528.8 keV).*

(2÷5 MeV) measured with MiDBD-II and with the 5×5×5 cm^3 and 3×3×6 cm^3 CUORICINO crystals are compared. It is clearly evident that a big improvement was obtained in the alpha and in the 3-4 MeV region, where, once subtracted the contribution due to the ^{190}Pt line, the background is mainly dominated by surface contaminations. The reduced contribution from these sources has given also an improvement in the 2-3 MeV region, where a reduction of ∼30% in the counting rates per unit mass either of the small and of the large crystals is obtained, despite the reduced internal lead shield used in CUORICINO with respect to MiDBD-II . The improvements observed in the CUORICINO background can be probably ascribed to the surface treatments of the copper structure and of the crystals. As it can be seen from Fig. (7.5), in the CUORICINO background spectrum of the 5×5×5 cm^3 crystals the ^{60}Co sum gamma line at 2505 keV is visible . This fact is probably due to the lower background level reached in CUORICINO with respect to MiDBD and to the higher rate of the ^{60}Co lines measured in the CUORICINO 5×5×5 cm^3 crystals.

With better statistical accuracy it will be possible to analyze the reasons for the variation observed in the counting rates of MiDBD and CUORICINO and also for the differences between small and large crystals. To accomplish that, it is indeed necessary to disentangle the different sources of background by considering the counting rates in small (and significant) regions. This is the case, for example, of the energy interval between the two gamma peaks at 2448 and 2615 keV (^{238}U and ^{232}Th chains respectively). Indeed this is the energy region where the DBD0ν line should appear. Here we expect two main contributions to background: one from degraded alpha particles from surface contaminations, the other from the multi-Compton events of the ^{208}Tl gammas from both bulk and surface contaminations in ^{232}Th . Another interesting region is the one just above the ^{208}Tl 2615 keV line, where background sources should be limited to surface contaminations. By disentangling the sources responsible of contributions in this region (surface contaminations of the crystals or of the materials directly facing them) it should be in principle possible to extrapolate the contributions to the DBD0ν energy region due to these sources. The two central crystals of the 9 crystals modules were intended to disentangle the background contributions due to surface
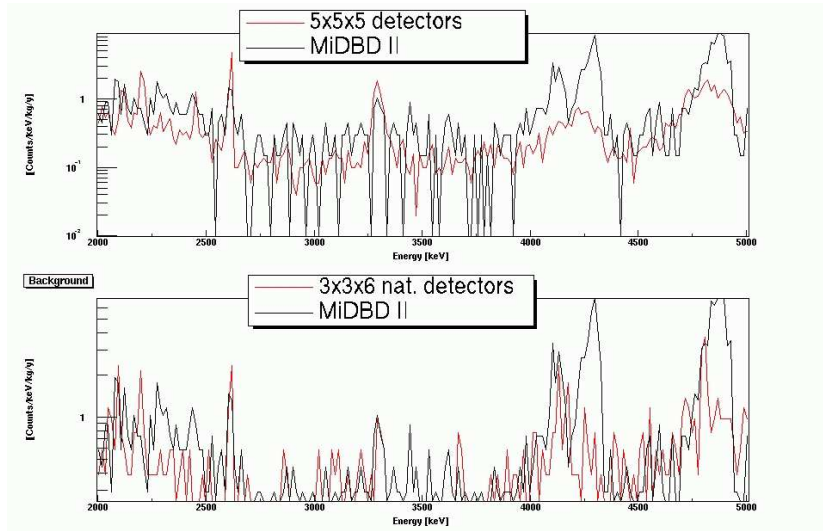
Figure 7.6: *Comparisons between the background spectra of MiDBD-II (black) and of the 5×5×5 cm³ (upper plot) and 3×3×6 cm³ (lower plot) CUORICINO crystals.*

contaminations of the TeO$_2$ crystals from that of the copper mounting structure. Indeed the two central crystals face a copper surface that is $\sim$3 times smaller than the one faced by the crystals placed at the edges of the modules. This kind of analysis requires a good statistical accuracy in the 3-5 MeV region, with a good calibration of the detectors even in the alpha region. Presently we do not meet these requirements, so this kind of analysis has to be postponed. It should be stressed, moreover, that the effect of disconnected detectors in reducing the efficiency of the anti-coincidence cut is not negligible. With the increase of the CUORICINO statistical accuracy and the gain in coincidence efficiency that we expect with all the detectors working, we will have higher possibilities to disentangle the different sources of the background.

counts/keV/kg/year	1-2 MeV	2-3 MeV	3-4 MeV	3-4 MeV (-^{190}Pt)	4-5 MeV
MiDBD-II	3.14±0.08	0.59±0.04	0.3± 0.03	0.27±0.03	1.85±0.06
3×3×6 natural	3.28±0.11	0.37±0.04	0.24± 0.03	0.22±0.04	0.79±0.05
5×5×5	3.92±0.03	0.45±0.01	0.21± 0.01	0.14±0.01	0.55±0.01

Table 7.4: *Counting rates per unit mass in MiDBD-II and in CUORICINO.*

Finally as respect to the 4 enriched crystals we have found an improvement in the measured background. They show in fact a considerable reduction (of the order of 20%) of their counting rates between 1 and 3 MeV. The alpha peaks counting rate in the region 4-6 MeV also show a considerable reduction (Fig. 7.8). The ^{40}K line now seems to have a similar counting rate in the four detectors while in MiDBD-II we had an excess in one of the ^{130}Te enriched crystals (Fig. 7.9). A longer measurement is however required to improve the evaluation (reducing the statistical and systematic errors) obtained with the MiDBD-II data for the DBD2ν half-life (Tab. 6.3).
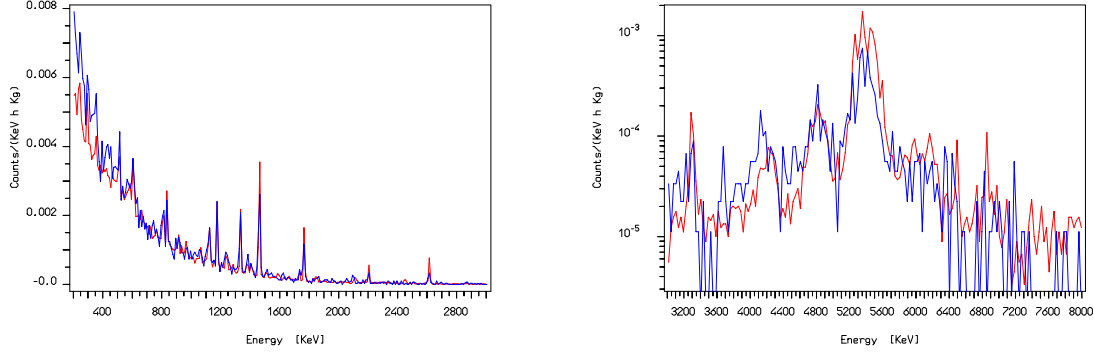
Figure 7.7: *Comparison between the background spectra of 5×5×5 cm³ crystals (continuous line) and 3×3×6 cm³ crystals (dashed line).*
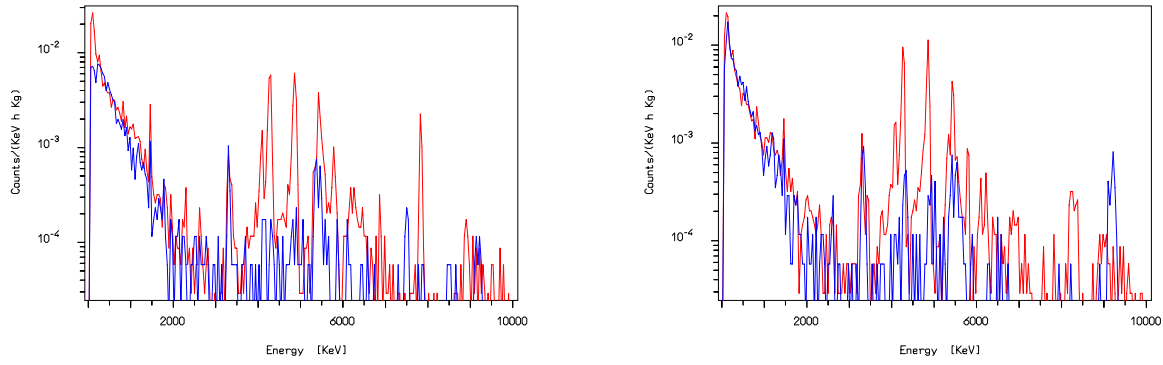
Figure 7.8: *Comparison between MiDBD (red) and CUORICINO (blue) ¹³⁰Te (left) and ¹²⁸Te (right) enriched crystals background.*

7.4 Background analysis

A background model able to describe the observed spectra in terms of environmental radioactivity, radioactive bulk contaminations of the whole detector setup (cryostat, shields and detector) and surface contaminations of the materials directly facing the detector (mainly Cu detector holder and TeO$_2$ crystals) was developed. Supported by detailed Montecarlo simulations of the detector geometry, this model allowed us to account for the background (peaks and continuum) measured in the two MiDBD runs (see chapter 6). We have used this same background model with the geometry of the CUORICINO setup, to disentangle the origin of the background measured with this experiment. Because of the poor statistical significance of the data so far collected, the analysis is preliminar (it was in particular limited to the 5×5×5 cm³ detectors for which the statistical accuracy is better) even if its results already tend to identify the most important sources of the CUORICINO background giving also a first quantitative guess of their relevance.

The analysis is based on both the coincidence and the anticoincidence spectra collected with the 5×5×5 cm³ detectors during the first run of CUORICINO and is mainly devoted to the study of the different contributions to the background in the DBD0ν energy region. A good calibration up to the alpha region is fundamental, since the shape and the position of the peaks can give us important
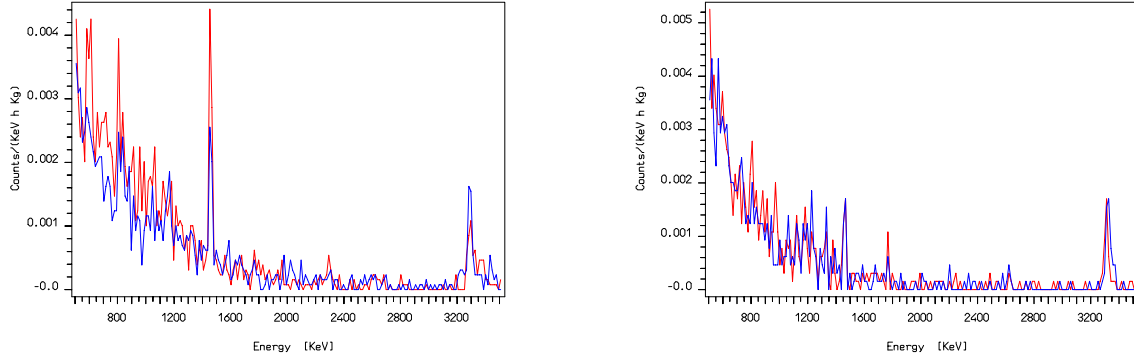
Figure 7.9: *Comparison between ^{130}Te (red) and ^{128}Te (blue) enriched crystals background in MiDBD (left) and CUORICINO (right).*
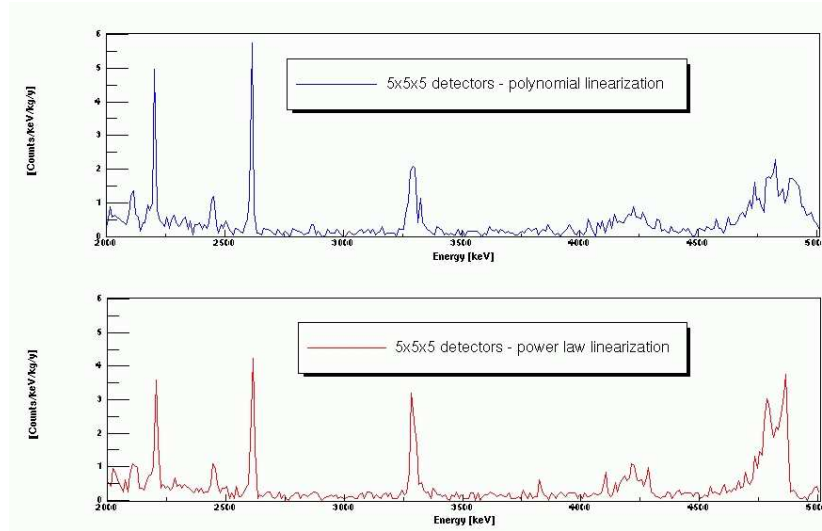
Figure 7.10: *Comparison between spectra obtained with different linearization methods. The appearence of clear alpha structures with the power law method is evident.*

informations to localize and disentangle the different sources of background. The techniques used in MiDBD-I and MiDBD-II to evaluate the relationship between pulse amplitude and particle energy ($\Delta V, E$) were based on theoretical detector models or polynomial fits. These linearization methods give good results in interpolation (as proved by the good energy resolution of the gamma peaks in the sum spectra) but very bad results in extrapolation up to the alpha region (extremely large alpha peaks) if no alpha peak is included. The low rate of the ^{210}Po alpha line measured with the CUORICINO crystals, prevented us in using it for the linearization. A new linearization technique based on a power low fit of the calibration points has then been tested. This new method has given rather good results in interpolation (even if poorer than with the previous two models) but better results in extrapolation with respect to the other methods. The anticoincidence sum spectrum of 5×5×5 cm^3 detectors calibrated in this way is compared in Fig. (7.10) with the analogous spectrum calibrated only with gamma lines and assuming a polynomial relationship between pulse amplitude and particle energy.

The two most probable sources of the background measured in the DBD0ν energy region have

been taken into account to study its origin: surface contaminations that mainly contribute via energy degraded alpha and beta particles, and bulk contaminations of ^{232}Th that contribute via the multi-Compton events of the 2615 keV line.

As already mentioned in previous discussions, alpha and beta particles, produced by environmental radioactivity, can give important contributions to the background above 3 MeV. Because of their low range these particles can only be emitted by sources located either in the crystals or on the surfaces of the materials directly facing the crystals: the copper holder or small components placed near the detectors or on the crystal surface such as the NTD thermistor, the Si heater, their gold wires, the glue and other smaller parts. Montecarlo simulations of the coincidence and anti-coincidence sum spectra of the 5×5×5 cm^3 detectors produced by radioactive contaminations of the above mentioned elements have been obtained using our GEANT4 based code. These spectra have been compared with the measured ones in order to identify the actual contaminations responsible of the measured background.

Alpha peaks

As a first step bulk and surface contaminations of the crystals have been considered. Both these contaminations give rise to peaks (centered at the transition energy of the decay) in the anticoincidence spectrum, but in the case of bulk contaminations these peaks are gaussian and symmetric while in the case of surface contaminations the peaks show a low energy tail (with a shape that depends on the depth and density profile assumed for the contamination). On the contrary, the only possible sources contributing to the coincidence spectrum are the surface contaminations of the crystals. The general shape and the structures appearing in the coincidence spectrum strongly depend on the depth and density profile assumed for the contamination (an exponentially decreasing function characterized by a depth λ: $\rho(x) = A\ e^{-\lambda x}$). The results of the comparison between Montecarlo simulations and measured spectra allow to prove that the alpha peaks of the anticoincidence spectrum of CUORICINO are due to a surface (and not bulk) ^{232}Th and ^{238}U contamination of the crystals with the only exception of the 5.3 and 5.4 MeV ^{210}Po lines. The first must be ascribed to a ^{210}Pb surface contamination of the copper holder, while the 5.4 MeV line must be ascribed to a ^{210}Po bulk contamination of the crystals . The observed decreasing intensity of the 5.4 MeV line during time is in fact in good agreement with the ^{210}Po half-life, proving that it is due to a ^{210}Po contamination not in secular equilibrium with the ^{238}U chain. The existence of this contamination was also observed for the MiDBD crystals as soon as they arrived from China. This signature can therefore to be ascribed to a ^{210}Po contamination of the tellurium powder from which the crystals were grown and to a possible contamination of the crystals during their production. Due to the short lifetime of ^{210}Po this contamination undergoes a fast decrease in time. It is therefore not considered an important contribution in CUORE background studies.

We have tested different contaminations depths for the ^{238}U and ^{232}Th surface contaminations of the crystals. The shape of the peaks in the anticoincidence spectrum and the shape of the coincidence spectrum is fully accounted for when a surface contamination depth of the order of 1 μm is assumed. As shown in Fig. (7.11) the identified crystal contaminations yield a satisfactory explanation of the coincidence spectrum.

Energy region above 3 MeV

Some contribution to the continuous part of the anticoincidence spectrum seems still missing.

In order to explain this continuum, a further source, not contributing to the coincidence spectrum, has to be considered. We have considered various possible sources for this background, as previously

Figure 7.11: *Comparison between Montecarlo and CUORICINO anticoincidence (top) and coincidence (bottom) spectra in the case of TeO₂ crystal surface contaminations ($\lambda \sim 1\mu m$).*

done for MiDBD, such as neutrons and muon induced neutrons and bulk contamination of small components closed to the detectors (Teflon spacers, NTD thermistors, Si heaters).We have finally focalized our attention to sources responsible of degraded alpha and beta particles, that means surface contaminations of the materials facing the detectors. The most probable source is a ^{232}Th or ^{238}U contamination (including the possible break of the secular equilibrium that in the most common case is represented by ^{210}Pb contaminations). Since the material with the bigger surface facing the crystals is the copper mounting structure we have focalized our study to the simulation of surface contaminations of this experimental component (Fig. 7.12), even if other parts, with bigger surface contamination density, could give contributions to the measured background in this energy region. The depth of the contamination should be of the order of $\sim$5 μm (a deeper contamination would produce too high gamma peaks (when normalized in order to account for the continuum rate in the 3-4 MeV region) while a thinner contamination would give rise to structures in the anticoincidence spectrum) with a total activity in the first 1.5 μm of the order of 10 ^{9} g/g either in ^{238}U or ^{232}Th or both.

Unfortunately no direct check of the obtained results is available, since surface contaminations of the copper parts give rise just to a flat continuum in the anticoincidence energy spectrum, and no alpha peak is produced. Low energy gamma peaks intensities can be used to set a limit on such contaminations, but does not give indication to establish if their origin is a bulk or a surface contamination. More statistics and at the same time independent measurements are necessary in order to evaluate the surface contaminations of the experimental parts directly facing the detectors and prove or reject the hypothesis of a main contribution coming from surface contaminations of the copper structure. On this purpose Inductive Coupled Plasma Mass Spectroscopy (ICPMS) measurements of the copper parts treated and handled with the same procedures used for CUORICINO are under work. Preliminary results give indications of surface contaminations in a layer of some μm depth of the order of 10 ^{9} g/g either in ^{238}U or ^{232}Th , in good agreement with our background model.

More sensitive and accurate measurements, able to account also for surface contaminations of the small parts facing the detectors (teflon spacers, gold wires etc.) need also to be performed, in order
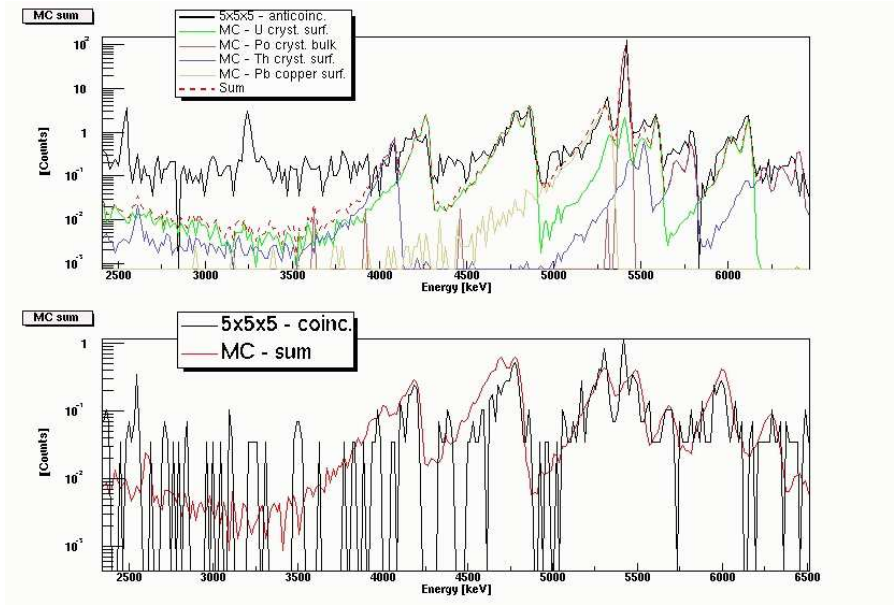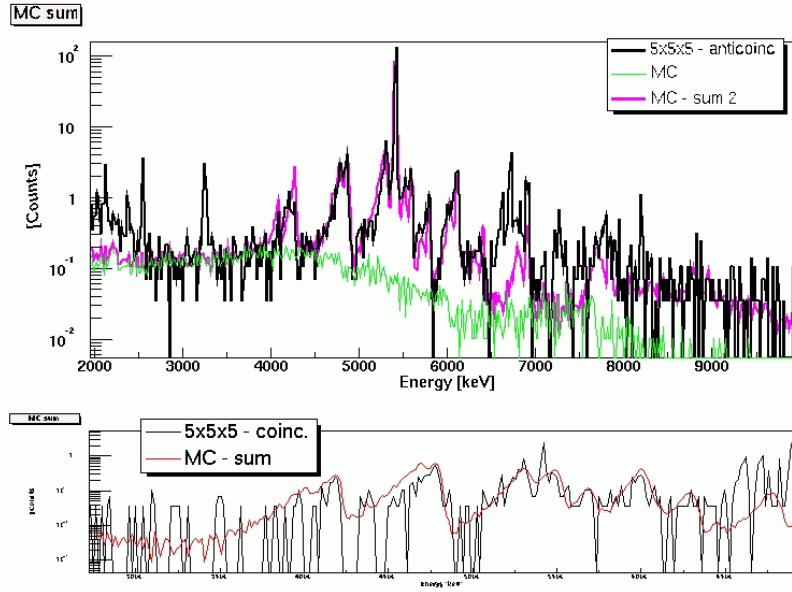
Figure 7.12: *Comparison between Montecarlo and CUORICINO anticoincidence (top) and coincidence (bottom) spectra in the case of TeO$_2$ crystal surface contaminations ($\lambda \sim 1\mu m$) + copper surface contamination in ^{238}U /^{232}Th ($\lambda \sim 5\mu m$).*

to safely exclude relevant contributions arising from these components. Measurements performed at LNBL gave in fact indications of a not negligible contamination of the teflon, used for the realization of the CUORICINO spacers. The amount of teflon facing the crystals, even if reduced with respect to MiDBD-I, is still not negligible and could represent an important source of background.

Contributions to the DBD0ν energy region

In order to quantify the different contributions to the DBD0ν region background, we need to evaluate the rate arising from the multi Compton scattering of the ^{208}Tl gamma at 2615 keV. Also for CUORICINO the analysis of the relative intensity of the gamma lines belonging to the ^{232}Th chain, give indications of a contamination localized far away from the detectors. As previously done for MiDBD, the contribution in the DBD0ν region due to this source, has been evaluated from the ratio observed in calibration between the area of ^{208}Tl line at 2615 keV and the integral in the DBD0ν region (Fig. 7.13).

The contributions evaluated for the DBD0ν and the 3÷4 MeV energy region from the identified sources, are summarized in Tab. (7.5). The correspondent contamination levels for crystals and copper structure surfaces, evaluated by means of Montecarlo simulations of the CUORICINO detector, are reported in Tab. (7.6). In evaluating these contamination levels we have attributed the crystals contribution to ^{238}U and the copper contribution half to ^{232}Th and half to ^{238}U surface contaminations.
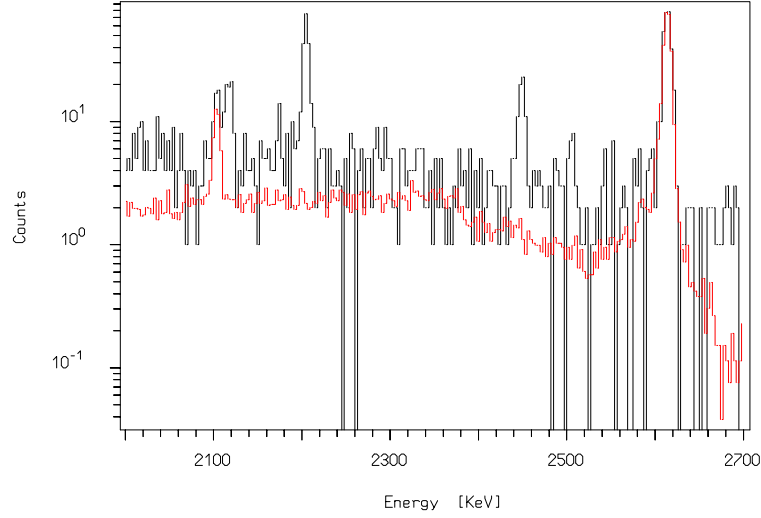
Figure 7.13: *Contribution to the DBD0ν region from the 2615 keV ^{208}Tl line, evaluated by a calibration spectrum.*

Source	^{208}Tl	$\beta\beta(0\nu)$ region	3-4 MeV region
TeO$_2$ ^{238}U and ^{232}Th surface contamination	-	10$\pm$ 10%	20$\pm$ 10%
Cu ^{238}U and ^{232}Th surface contamination	$\sim$15%	50$\pm$ 20%	80$\pm$ 10%
^{232}Th contamination of cryostat Cu shields	$\sim$85%	40$\pm$ 10%	-

Table 7.5: *Estimate of the weight of the different sources responsible for the background measured in the first run of CUORICINO.*

Source	Contribution to the DBD0ν bkg c/keV/kg/y	Contamination Bq/cm^2
TeO$_2$-U238	0.02 $\pm$ 0.01	1.9E-08 $\pm$ 9.8E-09
Cu-U238	0.05 $\pm$ 0.02	4.9E-08 $\pm$ 1.9E-08
Cu-Th232	0.05 $\pm$ 0.02	3.4E-08 $\pm$ 1.3E-08

Table 7.6: *Estimate surface contamination levels for CUORICINO crystals and copper mounting structure.*

Chapter 8

R&D and perspectives for CUORE

Introduction

As discussed in the previous sections, a number of recent theoretical interpretations of atmospheric, solar and accelerator neutrino experiments imply that the effective Majorana mass of the electron neutrino $|\langle m_\nu \rangle|$, could be in the range 0.01 eV to the present bounds.

The CUORE project originates as a natural extension of the successful MiDBD and CUORI-CINO ^{130}Te experiments, described before, with the objective of going to larger detector masses and of improving the sensitivity achieved in the smaller arrays. The good results obtained so far prove that the bolometric technique, although novel, is competitive and alternative to the traditional calorimetric Ge technique.

Due to the low rates of the searched process, the essential requirement of experiments devoted to this research is to achieve extremely low radioactive background rates and large masses. Accordingly, the use of radiopure detector components and shieldings, the development of methods and instrumentations for background identification, the operation in an ultra-low background environment or the use of the state-of-the-art of low background techniques, is mandatory. The construction of the CUORE detector will require about five years; a dedicated R&D is foreseen, aiming at reducing as much as possible the background sources that could limit the sensitivity of the experiment.

8.1 What can we learn from MiDBD and CUORICINO?

The material selection and the surface treatments performed with the CUORICINO detector led to a background in the DBD0ν region improved by a factor 1.5 with respect to the one measured in MiDBD-II. This fact and the background study performed on the MiDBD and CUORICINO data have shed light on how the radioactive sources, dominating the region of interest, are due to bulk and surface contaminations of the constructing materials.

The goal of CUORE is to achieve a background rate in the range 0.001 to 0.01 counts/(keV·kg·y) at the DBD0ν transition energy of ^{130}Te (2528.8 keV). An evaluation of the background reachable with CUORE can be obtained by means of a GEANT4 based code, able to reproduce the events expected in the CUORE detector for radioactive contaminations simulated in the various experimental parts. A real prediction of CUORE background would be possible only when we will have a complete knowledge of the intensities and distributions of all the background sources (radioactive contaminations of all the materials and of the cryostat that will be actually used in CUORE, materials exposure to cosmic rays, etc.). At the moment we miss several informations but we can in any case evaluate the background reachable with CUORE on the basis of the background model developed

for MiDBD and CUORICINO and on the basis of the radioactive contaminations measured so far for the various materials commercially at our disposal.

Due to its ability in evaluating the contributions expected from the different experimental material contaminations to the CUORE background, the developed Montecarlo method is also a very useful tool with respect to:

- *material selection:* we want to evaluate the intrinsic radiopurity levels necessary for the various experimental materials in order to reach with CUORE the required sensitivity. With the use of the Montecarlo developed method, we can in fact identify the experimental parts whose contaminations could give high contributions to the CUORE background in the DBD0ν energy region and for which it is therefore necessary a very accurate selection, with high sensitivity measuring techiques. At the same time we can identify the materials for which this is not necessary, thus leaving a bigger flexibility in the choice of the materials and permitting to save time and money.

- *material surface treatment:* the extrapolation of the background attainable in CUORE with the surface contaminations evaluated in MiDBD and CUORICINO is a good starting point to know the reduction we need in the surface contamination levels of the various materials in order to reach the wanted background level. Appropriate surface treatments and measuring techniques sensitive to very low surface radioactivity levels are therefore necessary.

- *detector geometry and shields optimization:* with the use of Montecarlo simulations of the CUORE detector we can test different geometries for the detector array and shieldings, in order to evaluate the best experimental setup with respect to radioactive background suppression and mechanical feasibility;

- *underground storage requirements:* by means of specific codes we can evaluate the cosmic ray induced radioactivity in the CUORE crystals and copper for different exposure to the cosmic radiation and different underground storage times. We can therefore optimize the production, assembling and storage procedure of the TeO$_2$ crystals and of the copper parts in order to reduce the cosmogenic activation.

8.2   Background evaluation

The code used to evaluate the background attainable in CUORE is based on the GEANT-4 package. It models the shields, the cryostat, the detector structure and the detector array. Even the smallest details of the detector apparatus (copper frames, screws, signal wires, NTD thermistors, etc.) and of the cryogenic setup were taken into account. In order to meet mechanical feasibility requirements for the cryostat, in addition to the first chosen cubical structure of the detector, a cylindrical structure has also been simulated. Like the Montecarlo code used in the analysis of the MiDBD and CUORICINO background, also the one used for CUORE includes the propagation of photons, electrons, alpha particles and heavy ions (nuclear recoils from alpha emission) as well as neutrons and muons. For radioactive chains or radioactive isotopes alpha, beta and gamma/X rays emissions are considered, according to their branching ratios. The time structure of the decay chains is taken into account and the transport of nuclear recoils from alpha emissions is included. The considered background sources are:

1. bulk and surface contamination of the construction materials, located inside the outer lead shield. The considered contaminants are ^{238}U , ^{232}Th chains and ^{40}K and ^{210}Pb isotopes;

2. bulk contamination of construction materials due to cosmogenic activation;

3. neutron and muon flux in the Gran Sasso Laboratory;

4. gamma ray flux from natural radioactivity in the Gran Sasso Laboratory;

5. background from the DBD2ν decay.

As explained in section (4.2) ^{238}U , ^{232}Th , ^{40}K , ^{210}Pb are the radioactive contaminants that are most commonly found in nature and are the main responsible of the radioactive background measured in low activity experiments. The analysis of the background measured in MiDBD and CUORICINO has shown their presence in bolometric experiments looking for the DBD0ν of TeO$_2$, and we have therefore to take them into account to make a real prediction of the background attainable with CUORE. Also cosmogenic activated isotopes must be taken into account, even if their activity is usually negligible. As discussed in section (4.2), due to the high cross section for cosmic activation of copper and tellurium, we can't in fact neglect the contribution of these isotopes to the background. The most dangerous cosmic activated isotope in these materials is ^{60}Co , due to its long lifetime. As respect to copper activation, the ^{60}Co production rate is well studied and the copper cross section for cosmic activation is well known. As respect to tellurium, the cross sections for cosmic activation found in literature [120] still have some uncertainty, and the evaluation of its activation is still under study with various routines and reactor measurements.

In our background model we have not simulated contaminations coming from the experimental parts located externally as respect to the outer lead shield (the dilution unit etc.). This choice is justified by the fact that in the selection of these materials we will require a contamination level lower or at least comparable to the environmental gamma background, already considered in our model.

8.2.1 Bulk contaminations

The main contribution to background from bulk contaminants comes from the cryostat structure (cryostat radiation shields), the heavy structures close to the detectors (the copper mounting structure of the array, the Roman lead box and the two lead disks on the top of the array) and from the detectors themselves (the TeO$_2$ crystals). The concentration of radioactive impurities used in the computations for these materials are given in Tab. (8.1).

Contaminant	^{232}Th	^{238}U	^{40}K	^{210}Pb	^{60}Co
TeO$_2$	0.5	0.1	1	10 μBq/kg	0.2 μBq/kg
copper	4	2	1	0	10 μBq/kg
Roman lead	2	1	1	4 mBq/kg	0

Table 8.1: *Bulk contamination levels (in picograms per gram) used in the simulation for TeO$_2$, copper and lead.*

These levels are nearly equal to the best upper limits obtained for the radioactive content of these same materials as shown in Tab. (8.2).
All the values reported in Tab. (8.2) are 90% upper limits. Indeed in all cases no evidence of the presence of radioactive contaminants was obtained for the material examined. The contamination levels of TeO$_2$ reported in Tab. (8.2) are the best upper limits obtained from the analysis of the data collected in MiDBD (Tab. 6.9) and in the first run of CUORICINO with the 5×5×5 cm^3 crystals.

A bolometric measurement was performed by the Milano group in order to determine the contamination of ^{210}Pb in the Roman Lead [119]. Copper [117] and lead [118, 117] contaminations were determined through low activity Ge spectrometry. The data presented in Tab. (8.2) are the best presently available in the literature for the radioactive contaminations of TeO$_2$, copper and lead.

From a comparison between Tab. (8.2) and Tab. (8.1) it is clear that the contamination levels assumed for the CUORE simulation are perfectly compatible with the presently available upper limits. The only exception is that of ^{60}Co in TeO$_2$ crystals, due to the impossibility of performing such a measurement to the required sensitivity with the available techniques. We will be probably able to reach such a sensitivity only with the CUORE detector itself. We have studied, together with the crystals factory, and on the basis of our present knowledge of the cosmic rays production rates and of the tellurium cross section for cosmic activation, a possible time schedule for the crystals growth and shipping to Gran Sasso, that can guarantee the required low level of ^{60}Co . A bulk contamination of the crystals in ^{60}Co can be very dangerous since, through the absorption of the two gammas and the beta emitted in the decay, it generates a continuum spectrum that can give a strong contribution to the DBD0ν region (Fig. 5.10). A minor contribution is due to the activated isotopes ^{110m}Ag and ^{124}Sb, whose activity is 4 times lower and fast decreasing with time.

In the case of CUORE, the control on crystal production will be severe. A single 750 g crystal can be grown in about two months, while it will require 18 months to grow the 1000 CUORE detectors. Once grown, the crystals will be shipped to Italy and stored underground. Their total exposure to cosmic rays could be therefore limited to about 4 months. The total residual cosmogenic activities after 2 years underground have been estimated (Sec. 5.4.2) using the COSMO code [109]. This code is studied to evaluate the production cross section and the activity of radio-nuclides produced by primary protons and secondary neutrons of the cosmogenic radiation. The results depend on two parameters: the cosmic ray flux, that is almost well known, and the energy dependency of the cross section, that must then be convoluted with the flux. The maximum value of the cross section of tellurium for cosmic rays activation is evaluated to range between 1 and 3 GeV. The residual cosmogenic activity of ^{60}Co in TeO$_2$ evaluated with COSMO is of $\sim$0.2 μBq/kg, for a total exposure to cosmic rays of 4 months and after 2 years of underground storage. A recent experimental determination of the ^{60}Co production cross section on tellurium by 1.85 GeV protons has been obtained at LNBL [121]. The measured value (0.63$\pm$0.15 mb) is in disagreement with the value used by the COSMO program (0.85 mb). Another measurement was made at CERN, measuring the production cross section of ^{60}Co by 24 GeV irradiating protons (far away from the interesting energy range), obtaining again a smaller value than that of COSMO. A new estimate of the production cross section of ^{60}Co using the YIELDS routine, containing the most updated version of the Silberberg and Tsao equations, produces results in much better agreement with the experimental measurements and gives an activity for ^{60}Co in the CUORE crystals almost one order or magnitude smaller than

Contaminant	method	^{232}Th	^{238}U	^{40}K	^{210}Pb	^{60}Co
TeO$_2$	bolometric	0.5	0.1	1.	15 μBq/kg	1 μBq/kg
Copper [117]	Ge diodes	5.6	2	0.3	-	10 μBq/kg
Roman lead [117]	Ge diodes	0.2	0.9	1.1	-	-
Roman lead [119]	bolometric				4mBq/kg	-
Low act. lead [118]	Ge diodes	3.4	2.7	1.7$\pm$ 0.3	23.4$\pm$ 2.4 Bq/kg	18$\pm$ 1 μBq/kg

Table 8.2: *Available 90% C.L. upper limits for bulk contaminations of TeO$_2$, copper and lead (levels in picograms per gram if not differently indicated).*

the previous estimate. The contribution to the DBD0ν energy region of the CUORE background by cosmogenic ^{60}Co discussed above, could be therefore overestimated by about one order of magnitude and the allowed exposure period for TeO$_2$ crystals could be consequently much longer.

Less critic is the ^{60}Co cosmogenic activation of copper. As shown in Fig. (5.10) in fact such a contamination contributes at high energies with the sum gamma line at 2505 keV, that can easily be separated from the searched signal at 2528 keV. As it will be shown later on the measured limit for the Cu contamination level in ^{60}Co (Tab. 8.2), guarantees a not relevant contribution to the CUORE background from this contamination.

Concerning small (mass) components of the CUORE detector, which we have not yet considered so far in the simulation (e.g. NTD Ge thermistors, Si heaters, glue layers, pins, wires and soldering material,etc.), a very careful selection according to their contamination is planned for the future. As it will be illustrated in more details in section 8.3, we can in fact set, by means of the Montecarlo code, upper bounds for the contamination levels of the small components, in order to have a negligible contribution to the CUORE background in the DBD0ν energy region.

The results of the Montecarlo simulations (see Fig. 8.1) for the background in the DBD0ν region, for both the detector structures (cubical and cylindrical), obtained using the contamination levels discussed here, are given in Tab. (8.3) (see also Fig. 8.2). Unfortunately the inclusion of the Roman Lead contribution in the computation of the CUORE background was not possible. A bug in the generation step for contaminations in this elements has been in fact recently found in the Montecarlo code. The problem will be solved in a short time but in any case we don't expect contributions from this source to the DBD0ν energy regions to be higher than the ones obtained for copper box impurities.

Figure 8.1: *Simulated spectra for bulk contaminations of the TeO$_2$ crystals (green), the Copper structure (red), the Copper 50mK shield (blue), the sum (black). Each spectrum is obtained by summing the simulated anticoincidence spectra of all the CUORE detectors.*

The assumed threshold is 10 keV and only values obtained after requiring an anti-coincidence between detectors are indicated. The reduction we expect, with the applied anti-coincidence cut ,of the contribution due to bulk contaminations in the crystals is about a factor of 4 for both the structures. This gives a reduction in the total background in the DBD0ν energy region of a factor $\sim$2. As it can be seen from Tab. (8.3) the results obtained for the cubical and cylindrical structures are compatible,
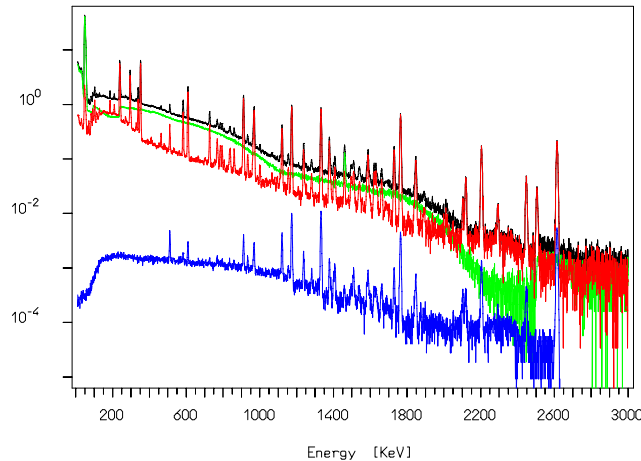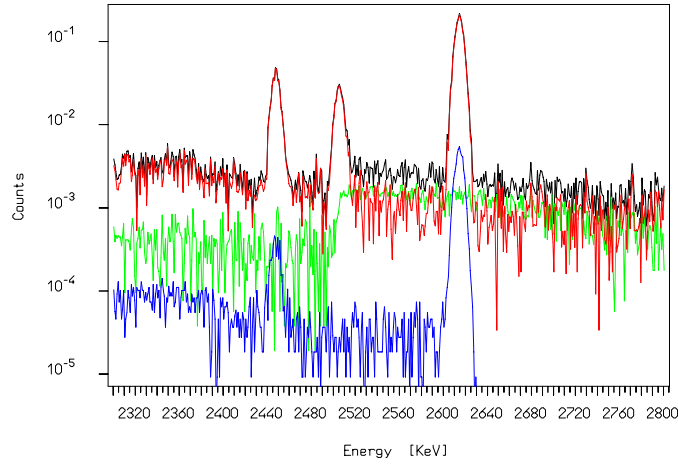
Figure 8.2: *Double beta decay region of the simulated spectra of CUORE for bulk contaminations of the TeO$_2$ crystals (green), the Copper structure (red), the Copper 50mK shield (blue), the sum (black). Each spectrum is obtained by summing the simulated anticoincidence spectra of all the CUORE detectors and by assuming as contamination levels the 90% C.L. limits evaluated for the materials actually at our disposal.*

this leaving much freedom in choosing one or the other structure in order to meet mechanical feasibility requirements. The values indicated in Tab. (8.3) have to be considered as upper limits on the possible contribution of bulk contaminations to the CUORE background. They prove that with the already available materials and without any optimization in the geometrical structure of the detector and shieldings the background in the DBD0ν region is lower than $\sim 4 \times 10^{-3}$ count/keV/kg/y (as discussed above the contribution due to the copper activation has been neglected).

We have also tested the possibility of an enriched (^{130}Te enriched crystals) detector with two different structures: 4 towers of 10 planes each or 9 towers of 5 planes each. The obtained background in the DBD0ν region after the anti-coincidence cut is reported in Tab. (8.4). The background obtained is higher than in the previous cases, since with a lower number of detectors the anti-coincidence cut is less efficient.

8.2.2 Surface contaminations

Surface contaminations contribute to the background only when they are localized on the crystals or on other materials directly facing them. In our model we have considered contaminations on the crystal surfaces and on the surface of the copper mounting structure, due to its large surface facing the detectors. As learned in MiDBD and CUORICINO, the presence of even a very low level of radioactive impurities on the surfaces of the detectors can produce a non negligible contribution to the DBD0ν background level. Unfortunately this kind of contamination, that is important mainly for detectors without a surface dead layer (as is the case of bolometers), is poorly studied. Lacking any data coming from direct measurements of the typical impurity levels present on TeO$_2$ and copper surfaces, we rely on the results obtained in MiDBD and CUORICINO (Tab. 7.6). These indicate that both a surface contamination of the crystals and of the copper surface of the mounting structure is present. In the case of TeO$_2$, we know that the contamination is mainly ^{238}U and that its presence is strictly connected to the kind of surface treatment undergone by the crystals. In the CUORICINO $5 \times 5 \times 5$ cm^3 crystals this contamination produces a background counting rate in the DBD0ν region

Cubical structure

Simulated element	Th232 c/keV/kg/y	U238 c/keV/kg/y	Co60 c/keV/kg/y	Sum c/keV/kg/y
TeO2	2.38E-04±2.48E-05	1.43E-05 ± 5.05E-06	1.17E-03 ±1.91E-05	1.42E-03 ± 3.17E-05
Cu Box	5.87E-04±5.38E-05	7.66E-05 ± 2.55E-05	0.00E+00 0.00E+00	6.64E-04 ± 5.96E-05
CuBar	4.48E-05±4.98E-06	3.06E-05 ± 5.40E-06	0.00E+00 0.00E+00	7.54E-05 ± 7.35E-06
Cu cell	2.14E-04±2.44E-05	1.58E-04 ± 2.76E-05	0.00E+00 0.00E+00	3.72E-04 ± 3.68E-05
Cu50mK	2.83E-05±2.31E-06	0.00E+00 ± 0.00E+00	0.00E+00 0.00E+00	2.83E-05 ± 2.31E-06
Sum	1.11E-03±6.43E-05	2.80E-04 ± 3.83E-05	1.17E-03±11.91E-05	2.56E-03 ± 7.73E-05

Cylindrical structure

Simulated element	Th232 c/keV/kg/y	U238 c/keV/kg/y	Co60 c/keV/kg/y	Sum c/keV/kg/y
TeO2	2.12E-04±2.36E-05	1.45E-05±5.11E-06	1.20E-03±1.95E-05	1.42E-03±3.10E-05
Cu Box	3.93E-04±4.63E-05	8.48E-05±2.83E-05	0.00E+00±0.00E+00	4.78E-04±5.43E-05
CuBar	2.97E-05±4.08E-06	2.71E-05±5.12E-06	0.00E+00±0.00E+00	5.68E-05±6.55E-06
Cu cell	1.63E-04±2.15E-05	2.33E-04±3.37E-05	0.00E+00±0.00E+00	3.97E-04±3.99E-05
Cu50mK	3.19E-05±2.21E-06	0.00E+00±0.00E+00	0.00E+00±0.00E+00	3.19E-05±2.21E-06
Sum	8.30E-04±5.64E-05	3.60E-04±4.46E-05	1.20E-03±1.95E-05	2.39E-03±7.45E-05

Table 8.3: *Computed background (after the anti-coincidence cut) in the DBD0ν energy region for bulk contaminations in the different elements for cubical and cylindrical structures.*

of about $(2\pm 1)\times10^{-2}$ counts/keV/kg/y. Concerning the copper surface contamination, we still miss a clear indication of its origin and identity (i.e. we are not yet able to distinguish between contributions generated by different sources), but we have an evaluation of the DBD0ν background counting rate that can be ascribed to them (whatever they are, ^{238}U or ^{232}Th): $\sim 0.1\pm 0.05$ counts/keV/kg/y.

According to a Montecarlo simulation of radioactive contaminations of the CUORE detector materials, based on the CUORICINO contamination levels (Tab. 7.6), we have extrapolated a background counting rate in the DBD0ν region (after the anticoincidence cut) that can range between ~ 1 and 2.5×10^{-2} counts/keV/kg/y for the TeO$_2$ crystals and between ~ 5 and 7×10^{-2} counts/keV/kg/y for the copper structure. The big spread is due to the high uncertainty level we have in the evaluation of the different radioactive contributions to the the CUORICINO background in the DBD0ν energy region (Tab. 7.5). The evaluated contributions to the DBD0ν energy region of CUORE are summarized in Tab. (8.5).

The goal of CUORE is to reduce the surface contributions by a factor at least 20 with respect to this evaluation, obtaining a background coming from surfaces of about 3×10^{-3} counts/keV/kg/y. Improvements of a factor of $\sim1.5\div2$ are expected simply by possible reductions of the copper mounting structure dimensions (the Montecarlo simulation we used so far refers to an identical mechanical structure for the CUORE and CUORICINO single detector modules). A reduction by a factor of about ten of the copper (TeO$_2$) surface contamination is therefore the first milestone of CUORE.

The expected shape of the background, produced by surface contaminations in CUORE obtained assuming the same contamination levels and the same mechanical structure of CUORICINO, is

4 towers structure

Simulated element	Th232 c/keV/kg/y	U238 c/keV/kg/y	Co60 c/keV/kg/y	Sum c/keV/kg/y
TeO2	4.68E-04±3.52E-05	1.25E-05±4.78E-06	1.20E-03±1.96E-05	1.68E-03±4.06E-05
Cu Box	7.60E-04±7.95E-05	8.37E-05±3.46E-05	0.00E+00±0.00E+00	8.44E-04±8.67E-05
CuBar	5.59E-05±5.64E-06	1.81E-04±4.22E-05	0.00E+00±0.00E+00	2.37E-04±4.26E-05
Cu cell	2.50E-04±2.67E-05	1.63E-04±2.83E-05	0.00E+00±0.00E+00	4.13E-04±3.90E-05
Cu50mK	4.02E-05±4.09E-06	0.00E+00±1.19E-06	0.00E+00±0.00E+00	4.02E-05±4.26E-06
Sum	1.57E-03±9.12E-05	4.41E-04±6.17E-05	1.20E-03±1.96E-05	3.22E-03±1.12E-04

9 towers structures

Simulated element	Th232 c/keV/kg/y	U238 c/keV/kg/y	Co60 c/keV/kg/y	Sum c/keV/kg/y
TeO2	3.52E-04±3.05E-05	1.07E-05±4.43E-06	1.20E-03±1.96E-05	1.56E-03±3.66E-05
Cu Box	8.73E-04±9.27E-05	6.63E-05±3.36E-05	0.00E+00±0.00E+00	9.39E-04±9.86E-05
CuBar	5.09E-05±5.38E-06	3.44E-05±5.81E-06	0.00E+00±0.00E+00	8.53E-05±7.92E-06
Cu cell	2.89E-04±2.87E-05	2.06E-04±3.19E-05	0.00E+00±0.00E+00	4.96E-04±4.29E-05
Cu50mK	3.69E-05±4.23E-06	0.00E+00±1.03E-06	0.00E+00±0.00E+00	3.69E-05±4.36E-06
Sum	1.60E-03±1.02E-04	3.18E-04±4.69E-05	1.20E-03±1.96E-05	3.12E-03±1.14E-04

Table 8.4: *Computed background (after the anti-coincidence cut) in the DBD0ν energy region for bulk contaminations in the different elements for 4 towers of enriched crystals and cylindrical structures.*

Element	Contamination Bq/cm^2	Contribution to the DBD0ν region c/keV/kg/y
TeO$_2$-U238	1.9E-08 ± 9.8E-09	1.6E-02 ± 8.4E-03
Copper	4.9E-08 ± 1.9E-08	5.8E-02 ± 6.6E-03
Total	3.4E-08 ± 1.3E-08	7.4E-02 ± 1.1E-02

Table 8.5: *Estimated upper contribution to the CUORE DBD0ν region from surface contaminations obtained by using the surface contamination levels evaluated for CUORICINO.*

given in Fig. (8.3).

8.2.3 Underground neutron, μ and γ interactions

As mentioned earlier, neither contributions from underground cosmic muons nor neutrons have been taken into account in detail in the estimation of the background. However, the following simplified arguments will serve to have an approximate idea of their contribution. The depth of the LNGS (3500 m.w.e) reduces the muon flux down to $\sim 2\times 10^{-8}$ cm^{-2}s^{-1}, but a further effective reduction could be obtained with the use of an efficient (99.9%) active veto for muons traversing the CUORE setup in order to tag possible events associated with them. The muon-induced contribution to the
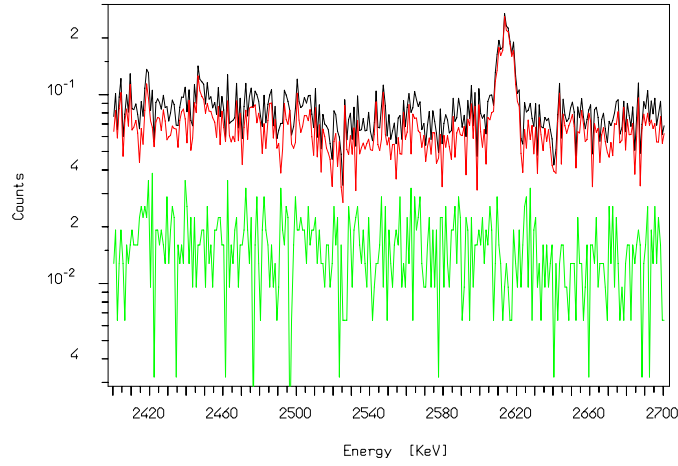
Figure 8.3: *DBD0ν region of the simulated spectra for the surface contaminations of the TeO₂ crystals (green), of the Copper structure (red), the sum (black). Each spectrum is obtained by adding the simulated spectra of all the CUORE detectors after the anticoincidence cut and by assuming the contamination levels evaluated for CUORICINO.*

background is therefore expected to be negligible.

On the other hand, the heavy shieldings surrounding the CUORE detector will substantially reduce the event rate due to environmental radiation of various origin (neutrons and photons), environmental radioactivity (natural decay chains U/Th, ^{210}Pb, ^{40}K, . . .), as well as muon interactions in the surroundings rock or in the shielding itself. In general, one considers neutrons of two origins: from radioactivity in the surroundings or muon-induced. Depending on the overburden of the underground site (i.e., depending on the muon flux), muon-induced neutrons are produced, at lesser or greater rate, both inside and outside the shielding. They are moderated (according to their energies) by the polyethylene/lead shield (when produced outside) or tagged by the muon veto coincidence (when produced within the passive shielding). The flux of external neutrons in the LNGS environment has been measured (section 4.1) and has been evaluated to be well moderated by the polyethylene shield and eventually absorbed or captured. We have carried out a Montecarlo simulation of the propagation of neutrons through the 10 cm thick borated polyethylene shield of CUORE. The result is that the neutron induced event rate on the entire energy range (from threhsold to 10 MeV) is much lower than the contribution due the bulk contamination of crystals. Neutrons produced by muon interaction inside the shielding materials are very scarce and they can be efficiently tagged by the muon veto. We have estimated that for the LNGS muon flux (2.5×10^{-8} μ/(cm^2 s)), muons would produce in the CUORE shielding of polyethylene (10 cm) and lead (20 cm)), about ∼0.04 neutrons/day in the polyethylene shield and ∼25 neutrons/day in the lead shell. So, independent of the mechanism used to reject or tag the events associated to neutrons, their rather small number is expected to play a secondary role in the total background compared with other main sources of background.

A preliminary evaluation of the influence of the environmental γ background in Gran Sasso resulted in a negligible contribution for the DBD0ν region.

A more complete and detailed study of the background rates from external sources for CUORE is underway and will be used for the optimization of shieldings and muon veto.

113

8.2.4 Two neutrinos double beta decay background

Using the present upper limits for the ^{130}Te DBD2ν half-life and the foreseen energy resolution in the DBD0ν energy region of ~5 keV FWHM, the unavoidable background produced in the DBD0ν region by the DBD2ν has been evaluated to be completely negligible.

8.3 Background R&D for CUORE

CUORE construction will require about five years. During that period we plan to spend much effort in trying to further reduce the achievable background. There are indeed several points on which it is possible to work.

Material selection

The maximum acceptable value (Tab. 8.6) for the contamination level of the small components of the CUORE detector, has been evaluated by means of the Montecarlo code, by setting their computed overall contribution to the CUORE background in the DBD0ν energy region to a resonable value of ~ 0.001 c/keV/kg/y (Tab. 8.7).

Contaminant element	^{232}Th mBq/kg	^{238}U mBq/kg	^{60}Co mBq/kg	^{210}Pb mBq/kg
copper	16E-03	25E-03	10E-03	-
roman lead	8E-03	12E-03	-	4
normal lead	8E-03	12E-03		
NTD	3	1	0.1	30
Si heaters	4	2	0.2	0.3
Araldit	3E+03	1E+03	0.1E+03	30E+03
Cu pin	20	10	0.3	30E+03
teflon	40	25	2E-03	0.3
Au wires	3	2	1.7	30
Cu screws	0.2	0.1	3e-3	3

Table 8.6: *The maximum acceptable value for the contamination of the various CUORE materials.*

A program of measurements is therefore necessary, in order to test and consequently select the most radiopure materials. The working program shown in Tab. (8.8) is based on the performances of the best germanium facility we can access at the LNGS (Fig. 8.4). Also materials used in the detector assembling (i.e. vacuum grease and tin, acids, gloves, paper tissues, tools, varnish and stycast glue, etc.) must be measured.

A very high radiopurity level is required for copper and lead, since the mass of these materials that surrounds the detector is quite large (~1500 kg of Roman Lead and 150 kg of copper inside the Roman Lead shield). Copper measurements with the wanted sensitivity level have already been done by Prof. G.Heusser [117], with a dedicated germanium detector. With respect to roman lead, neutron activation measurements are under study.

Concerning the crystals, as it can be seen from Tab. (8.3), the higher evaluated contribution to the DBD0ν energy region, due to their bulk impurities, arises from ^{60}Co activation. As discussed above the actual cross sections to be used to compute the tellurium activation, after a supposed 4

Simulated element	Th232 c/keV/kg/y	U238 c/keV/kg/y	Co60 c/keV/kg/y	Pb210 c/keV/kg/y
NTD	4.52E-05± 9.03E-06	3.59E-05 ± 5.29E-06	5.48E-05 ± 6.84E-07	6.00E-05±1.55E-05
Wires	4.07E-05± 2.96E-06	4.27E-05 ± 2.81E-06	5.10E-05 ± 8.30E-07	5.84E-05±5.27E-06
Araldit	4.24E-05± 8.49E-06	3.37E-05 ± 4.97E-06	5.15E-05 ± 6.42E-07	5.64E-05±1.46E-05
PTFE	5.34E-05± 7.40E-06	5.31E-05 ± 6.13E-06	4.25E-05 ± 5.24E-07	5.45E-05±9.95E-06
Si-heaters	5.08E-05± 7.05E-06	5.06E-05 ± 5.84E-06	4.05E-05 ± 4.99E-07	5.19E-05±9.48E-06
Pin	4.25E-05± 2.46E-05	3.91E-05 ± 1.95E-05	4.45E-05 ± 1.13E-06	5.02E-05±5.02E-05
CuScrews	5.71E-05± 3.30E-05	5.25E-05 ± 2.62E-05	5.98E-05 ± 1.51E-06	6.74E-05±6.74E-05

Table 8.7: *Computed background (after the anti-coincidence cut) in the DBD0ν energy region for bulk contaminations in the small components set to the maximum accettable value.*
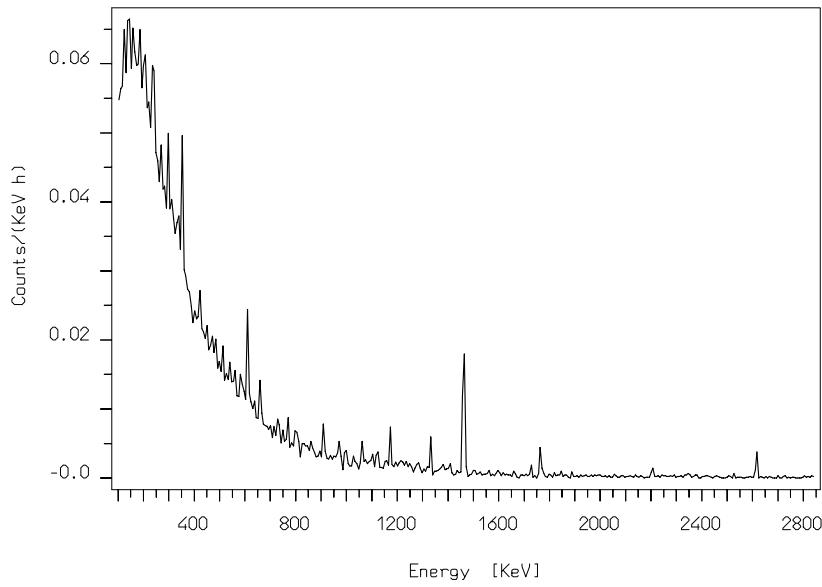
Figure 8.4: *Background measured with the best Ge facility accessible at LNGS.*

element	mass [g]	measure time [h]
NTD	30	1000
Si heaters	30	3000
Araldit	300	300
Cu pin	2E+03	300
teflon	4E+03	300
Au wires	50	4000
Cu screws	5E+03	1000

Table 8.8: *Germanium measurement program for the CUORE materials.*

months period of exposure to cosmic rays and 2 years of underground storing, could be one order of magnitude lower than the ones used by the COSMO code. The ^{60}Co contribution could therefore be not so relevant. For ^{238}U and ^{232}Th impurities the surface contaminations prevent us from obtaining a sensitive measure and actually we have only upper limits of the order of 10^{-13}g/g. However we know that before crystallization the TeO$_2$ powder is much more contaminated (Tab. 4.2) and that the crystallization procedure usually reduces the contamination level of the final crystal with respect to the bare material. Therefore the selection of a lower contamination TeO$_2$ powder, together with the efficient reduction of impurities by the crystallization procedure should guarantee a contamination level of $\sim 10^{-14}$ g/g. A complete over all control of every single step the crystals undergo during their production from the original metallic powder is of fundamental importance to ensure that no additional contaminations are introduced. As already discussed in section (4.2), for example, the presence of contaminants in the water used to clean the TeO$_2$ powders just after their production and before the growing procedure could be transferred to the powder. Also the material used for the crucible in which the crystals are grown is critical in order to avoid the implantation of some contaminant (eg. ^{190}Pt) in the crystals bulk.

Material surface treatment

As discussed in section (8.2.2) the most dangerous radioactive source is the surface contamination of the crystals and of the parts with a large surface facing the detector. Particular care must therefore be devoted to choose the best materials, tools and procedures to be used to guarantee the required purity level after machining and cleaning.

As discussed in section 6.4, the MiDBD crystal surfaces were contaminated, probably during the polishing procedure, due to the use of highly contaminated powders. Polishing powders with a much lower radioactive content are however commercially available [122] and have already been used for CUORICINO (Tab. 4.2) obtaining a clear improvement in the surface contamination. A complete over all control of the surface treatments undergone by the crystals after growth, and the use of radiopure substances should guarantee an even better result than that obtained in CUORICINO.

A similar situation holds for copper. In MiDBD and in CUORICINO the copper surfaces were treated with an etching procedure [123] optimized in order to reduce impurities on surfaces before the sputtering process. This procedure significantly improved the surface quality of copper and reduced its surface contamination level. However it was not optimized from the point of view of background. The use of low activity materials (thumbler) and of low contaminated liquids (water and inorganic acids are available with ^{238}U and ^{232}Th contamination levels lower than 0.1 pg/g) in a low background environment will allow a sizeable improvement of the surface contamination of copper.

This (i.e. a slight improvement of the technique used with CUORICINO) and other cleaning procedures are under study and are going to represent a consistent part of the CUORE R&D activities during the first two years after approval.

A bolometric measurement aiming to test a new cleaning procedure, for TeO$_2$ crystals and copper frames, performed with low radioactivity measured materials, is in progress in the R&D setup, located in the hall C of LNGS. First results seems to indicate a reduction of a factor ~ 5 in the contribution due to the crystal surface contaminations (reduction of the alpha peaks and of the background above 6 MeV). The measured background in the 3÷4 MeV energy region seems however to be compatible with respect to the corresponding value obtained in CUORICINO, despite the different and more accurate cleaning procedure. A higher statistics is however necessary in order to perform a more accurate analysis and to take precise conclusions.

Very important is also to find a good technique able to measure with the proper sensitivity the

surface contamination of the various materials that will face the detectors. While the surface contamination level of the crystals can be deduced by the alpha peaks intensities visible in the energy spectrum of a bolometric measurement, more difficult is the realization of a surface measurement for the copper and for other parts facing the detectors, as for instance the teflon spacers.

Fast diagnostic methods to measure the surface contamination levels of Copper and determine the effectiveness of the adopted surface cleaning procedures are under investigation. Preliminary results indicate that high resolution ICPMS could satisfy our requirements [124]. Sensitivities achievable with this technique for ^{238}U and ^{232}Th are in the range of $10^{-(3-2)}$ ppt of solution under investigation. Since the maximum solution concentration can be 2×10^{-3}, the expected sensitivity on the solute contamination (Copper) would be in the range 1–10 ppt of ^{238}U and ^{232}Th, i.e. enough for our requirements. From the above discussion in fact, the surface contamination measured in CUORICINO (assuming a 1 μm copper layer) is of the order of $\sim$1–10 ppb of ^{238}U and ^{232}Th. Of course very low radioactive levels comparable or even lower than the instrumental sensitivity are required for liquids (mainly acids and water) to be used in the solution preparation (i.e. copper surface removal). Liquids satisfying this requirement are however already commonly available.

Promising results have also been obtained with test performed on surface sensitive bolometers. The basic idea consists in the realization of active shields in the form of thin, large-area, ultrapure, Ge or Si bolometers, by which the TeO$_2$ crystals is surrounded so as to get rid of possible events originating in the germanium (which could release part of their energy in the main detector) or outside the detector with the anti-coincidence technique. The Ge or Si auxiliary bolometers are attached at the main crystal, providing almost complete coverage. In this way, a composite bolometer is realized with multiple read-out, capable to distinguish the origin of the event (active shields or TeO$_2$ crystal) by means of the comparison among pulses coming from the different elements. A degraded alpha coming from outside would release its energy in the shield, originating a thermal pulse that, seen by the shield thermistor, would be much higher and fast than a corresponding pulse of the same energy released directly in the main TeO$_2$ crystal. In Fig. (8.5) it is possible to appreciate the efficiency of the separation method. A scatter plot is shown, where the amplitude of the pulses collected with the TeO$_2$ thermistor is plotted against the amplitude of the corresponding pulses collected with the shield thermistor. Two clearly separated curves identify the events generated in the shield with respect to the events generated in the main crystal. With such a technique we could therefore be able to disentangle the contributions to the background due to the copper surface contaminations. Measurements of this kind are planned within 6 months in the hall C facility of LNGS.

Test on neutron activation measurements of teflon and araldit samples (0.13 and 7.5 grams respectively) have been performed at the McClellan Nuclear Reactor Facility of Sacramento, with a neutron flux of 1.8 $\times10^{13}$neutrons/cm^2/sec. No useful results have been however obtained due to large amounts of disturbing contaminants (i.e.^{24}Na, ^{82}Br, ^{124}Sb, ^{65}Zn, etc.). The only obtained result regards the ^{232}Th contamination of teflon that has been found to be 0.6 mBq/kg before the acid etching and 0.2 mBq/kg after the etching procedure. This reduction after surface etching could indicate the existence of a not negligible surface contamination of the measured teflon samples. Standard alpha measurements of teflon and araldit samples are planned in a short time in order to evaluate the surface contamination of these components.

Detector geometry and shieldings optimization

The CUORE structure described up to now is based on the results obtained in CUORICINO and on the experience gathered with the test-runs performed in the hall C cryostat on the $5\times5\times5$ cm^3 crystals. We have been very conservative in the design of every CUORE element. However, we foresee a significant activity of R&D during the next one or two year. In fact, there are indications
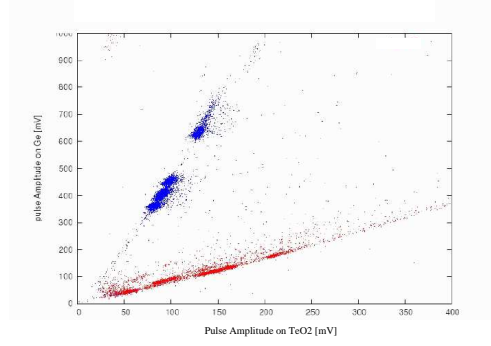
Figure 8.5: *Scatter plot of the pulse amplitude from TeO₂ thermistor vs. the pulse amplitude from the shield thermistor.*

that several aspects of the CUORE detectors can be improved substantially with respect to the present performance (for instance, single element reproducibility) and some of them need to be improved dramatically (mostly, the background level due to surface contamination that could limit the CUORE sensitivity).

As discussed in section (8.2.1) different possibilities for the detector geometry have been tested. Mechanical feasibility requirements for the cryostat would in fact prefer a cylindrical structure of the detector with respect to the initially chosen cubical one. Since Montecarlo simulations have shown compatible results for the two setups, the finally chosen structure was the cylindrical one (Fig. 5.4b), provided also with cylindrical shields.

Still open is the choice of the material and of the thickness of the shields. Cryogenic motivations would in fact prefer copper instead of roman lead for the shieldings composition. Montecarlo simulations are therefore planned in order to to find out the best shielding composition and thickness in order to have a negligible contribution to the background in the DBD0ν energy region from the contamination of the shielding and of all the experimental parts external to the shield itself.

As quoted above, also the geometry of the detector frames need to be optimized, in order to have the least amount of copper and teflon facing the crystals but at the same time have a good holding system, preventing crystals from vibrations. This reduction could give improvements of a factor $\sim 1.5 \div 2$ in the DBD0ν region background. Tests with a new crystal hanging system are planned in a short time in the R&D facility in hall C of LNGS.

8.4   CUORE DBD0ν sensitivity

The main scientific objective of the CUORE detector is the search for neutrinoless double beta decay of the ^{130}Te isotope, contained in the TeO₂ crystals. The detector factor of merit F$_D$ (eq. 1.57), or detection sensitivity, introduced in section (1.2), provides an approximate estimate of the neutrinoless half-life limit (1σ) achievable with a given detector. In the case of $5 \times 5 \times 5$ cm³ TeO₂ bolometers

(for which the DBD0ν detector efficiency is 0.86) we have

$$F_D^{0\nu} \sim 7.59 \times 10^{23} \sqrt{\frac{Mt}{B\Gamma}}$$

(8.1)

with M the crystal mass in kg and B the background in counts per keV per year and per kg of detector mass.

A background of B=0.01 c/keV/kg/y would be achievable with a slight improvement of the current available material selection and cleaning techniques and exploiting the possibility to build a dedicated cryostat with low activity materials and effective shields. Assuming finally an energy resolution Γ(2.5 MeV)=5 keV, we would get F$_D^{0\nu}$ of $9.4 \times 10^{25}\sqrt{t}$ years ($6.5 \times 10^{25}\sqrt{t}$ years for Γ=10 keV), which in t years of statistics would provide $|\langle m_\nu \rangle|$ bounds in the range 0.036–0.2 $t^{-1/4}$ eV (according to QRPA models F$_N$ predictions, Tab. (1.2)). However, the R&D to be carried out in CUORE, if successful, would provide a value of B$\sim$0.001 c/keV/kg/y, i.e. a detection sensitivity of F$_D$$\sim$$2.96 \times 10^{26}\sqrt{t}$ years ($2.1 \times 10^{26}\sqrt{t}$ years for Γ=10 keV), or $|\langle m_\nu \rangle|$ bounds in the range $\sim$$0.02$–$0.11$ $t^{-1/4}$ eV.

8.4.1 Enrichment option

CUORE is the only proposed next generation DBD0ν experiment that plans the use of non-enriched material. Indeed, the high isotopic abundance of ^{130}Te allows very high sensitivities even using the much cheaper natural tellurium. This obviously implies that the construction of a larger array would not only be technically possible but also fisically acceptable. On the other hand the high natural abundance of ^{130}Te allows a much simpler and less expensive enrichment procedure than that for other double beta decay candidates.

The possibility of an enriched detector has been taken into account. TeO$_2$ crystals made with ^{130}Te enriched material have been already operated in MiDBD and CUORICINO, making an enriched CUORE a feasible option. The last proposed geometry for the cUORE detector is made by a core of 144 enriched crystals, arranged in 4 towers of 9 planes each, and surrounded by 844 natural crystals. The sensitivity reachable with this detector configuration has been evaluated. With a background of B=0.01 c/keV/kg/y and an energy resolution Γ(2.5 MeV)=5 keV, we would get F$_D^{0\nu}$ of $1.85 \times 10^{26}\sqrt{t}$ years ($1.28 \times 10^{26}\sqrt{t}$ years for Γ=10 keV), which in t years of statistics would provide $|\langle m_\nu \rangle|$ bounds in the range 0.026–0.14 $t^{-1/4}$ eV (according to QRPA models F$_N$ predictions, Tab. (1.2)). With a value of B$\sim$0.001 c/keV/kg/y, a detection sensitivity of F$_D$$\sim$$5.85 \times 10^{26}\sqrt{t}$ years ($4.14 \times 10^{26}\sqrt{t}$ years for Γ=10 keV) would be possible, corresponding to an $|\langle m_\nu \rangle|$ bounds in the range $\sim$$0.01$–$0.08$ $t^{-1/4}$ eV.

Bibliography

[1] K2K Collaboration, Phys. Rev. Lett. **90** (2003) 041801.

[2] D. N. Spergel et al., Astrophys. J. Suppl. **148** (2003) 175.

[3] R. M. Barnett et al., Physical Review **D 54** (1996) 1.

[4] B. Pontecorvo, J. Exptl. Theoret. Phys. **3**3 (1957) 549. [Sov. Phys. JETP **6** (1958) 429]; J. Exptl. Theoret. Phys. **34** (1958) 247 [Sov. Phys. JETP **7** (1958) 172].

[5] Z. Maki, M. Nakagawa and S. Sakata, Prog. Theor. Phys. **28** (1962) 870.

[6] O. Civitarese and J.Suhonen, Nucl. Phys. **A729** (2003) 867.

[7] S.M. Bilenky and S.T. Petcov, hep-ph/0405237.

[8] Y. Chikige, R.N. Mohapatra and R.D. Peccei, Physical Letters **B 54** (1981) 98:265.

[9] E. Caurier et al., Phys. Rev. Lett. **77** (1996) 1954.

[10] J. Suhonen and O. Civitarese, Phys. Rep. **300** (1998) 123.

[11] A. Staudt, Kuo and H. V. Klapdor-Kleingrothaus, Phys. Rev. C **46** (1992) 871.

[12] G. Pantis et al., Phys. Rev. C **53** (1996) 695.

[13] P. Vogel et al., Phs. Rev. Lett. **57** (1986) 3148.

[14] O. Civitarese, A. Faessler, T. Tomoda, Phys. Lett. B **194** (1987) 11.

[15] T. Tomoda, Rep. Prog. Phys. **54** (1991) 53.

[16] C. Barbero, F. Krmpotic, A. Mariano, and D. Tadic, Nucl. Phys. A **650** (1999) 485.

[17] F. Simkovic, Phys. Rev. C **60** (1999) 055502.

[18] J. Suhonen, O. Civitarese and A. Faessler, Nucl. Phys. A **543** (1992) 645.

[19] K. Muto, E. Bender, and H. V. Klapdor-Kleingrothaus, Z. Phys. A **334** (1989) 187.

[20] S. Stoica and H. V. Klapdor-Kleingrothaus, Phys. Rev. C **63** (2001) 064304.

[21] A. Faessler and F. Simkovic, J. Phys. G **24** (1998) 2139.

[22] J. Engel, P. Vogel, and M. R. Zirnbauer, Phys. Lett. **B 225** (1989)5

[23] M. Aunola and J. Suhonen, Nucl. Phys. A **643** (1998) 207.

[24] V. A. Rodin, A. Faessler, F. Simkovic and P. Vogel, nucl-th/0305005.

[25] W.C. Haxton, G.J. Stephenson, Prog. Part. Nucl. Phys. **12** (1984) 409.

[26] J. G. Hirsh et al., Nucl. Phys. A **589** (1995) 445.

[27] M. Doi, T. Kotani, E. Takasugi, Progr. Theor. Phys. Suppl. **83** (1985) 1.

[28] S.T. Petcov, A.Yu. Smirnov, Phys. Lett. B 322, 109 (1994); H.V. Klapdor-Kleingrothaus, H. Päs, A.Y. Smirnov, Phys. Rev. D 63, 073005 (2001).

[29] S.M. Bilenky, C. Giunti, C.W. Kim, and S.T. Petcov, Phys. Rev. D 54, 4432 (1996); S.M. Bilenky, C. Giunti, W. Grimus, B. Kayser, and S.T. Petcov, Phys. Lett. B 465, 193 (1999); S.M. Bilenky, S. Pascoli and S.T. Petcov, Phys. Rev. D 64, 053010 (2001); S.M. Bilenky, C. Giunti, J.A. Grifols, E. Massó, Phys. Rep. 379, 69 (2003).

[30] S. Pascoli, S.T. Petcov and L. Wolfenstein, Phys. Lett. B 524, 319 (2002); S. Pascoli, S.T. Petcov, W. Rodejohann, Phys. Lett. B 549, 177 (2002); Phys. Lett. B 558, 141 (2003); S. Pascoli and S.T. Petcov, Phys. Lett. B 580, 280 (2004); Phys. Lett. B 580, 280 (2004);

[31] F. Feruglio, A. Strumia, and F. Vissani, Nucl. Phys. B 637, 345 (2002); Nucl. Phys. B 659, 359 (2003).

[32] M. Czakon, J. Gluza, J. Studnik, and M. Zralek, Phys. Rev. D 65, 053008 (2002).

[33] H. Minakata, H. Sugiyama, Phys. Lett. B 567, 305 (2003).

[34] F.R. Joaquim, Phys. Rev. D 68, 033019 (2003).

[35] C. Giunti, hep-ph/0308206.

[36] H. Murayama, C. Pena-Garay, Phys. Rev. D 69, 031301 (2004).

[37] J.N. Bahcall, H. Murayama, C. Pena-Garay, hep-ph/0403167.

[38] V. Barger, S. L. Glashow, D. Marfatia, and K. Whisnant, Phys. Lett. B **532** (2002) 15.

[39] Steven R. Elliott and Jonathan Engel, nucl-ex/0204009;

[40] Heidelberg-Moscow collaboration, H. V. Klapdor-Kleingrothaus *et al.*, Eur. Phys. J. **A** 12, (2001) 147.

[41] CUORE collaboration, O. Cremonesi, Proceedings of the 5th Workshop NOON2004, 11-15 February 2004, Tokyo, Japan.

[42]

[43] S.R. Elliott and P. Vogel, Ann. Rev. Nucl. Part. Sci. **52** (2002) 115; hep-ph/0202264.

[44] G. Gratta, Proceedings of the XXI International Symposium on Lepton and Photon Interactions at High Energies, 1-16 August 2003, Fermilab, Batavia, Illinois USA.

[45] F. T. Avignone, Proceedings of the 5th Workshop NOON2004, 11-15 February 2004, Tokyo, Japan.

T.Kirsten et al., *Phys. Rev. Lett.***50** (1983), 475
T.Kirsten et al., *Nuclear Beta Decay and Neutrino,*World Scientific, (1986), 81
J.F.Richardson et al., *Nucl. Phys.* **A 453** (1986), 26
O.K.Manuel, *Nuclear Beta Decay and Neutrino,* World Scientific, (1086), 71
Elliot et al., *Phys. Rev. Lett.* **59** (1987), 2020
K.Marti, S.V.Murty, *Phys. Lett.* **B 163** (1985), 71
K.Marti, S.V.Murty, *Geochim. Cosmochim. Acta* **51** (1987), 163
K.Y.Chiou, O.K.Manuel, *Neutrino Mass and Related Topics* World Scientific (1988), 178
W.J.Lin et al., *Nucl. Phis.* **A 481** (1988), 477 e **A 481** (1988), 484
J.T.Lee et al., *Nucl. Phis.,* (1990)
N.Takaoka, K.Sagawa, *Neutrino Mass and Related Topics,* World Scientific, (1988), 183
N.Takaoka, K.Sagawa, *45th Annual Meeting, Phis. Soc. Japan Abstract,* **31 a-S-11,** 48

[46] W.C. Haxton, G. J. Stephenson, *Prog. Part. Nucl. Phys.* **12** (1984),409

[47] G. F. Dell'Antonio and E. Fiorini, Suppl. Nuovo Cimento 17 (1960) 132.

[48] H. V. Klapdor-Kleingrothaus, hep-ph/0103074.

[49] IGEX Collaboration, Aalseth, C. E. *et al.,* Phys. Rev. **D65** (2002) 092007, hep-ex/0202026.

[50] Super-Kamiokande Collaboration, S. Fukuda *et al.,* Phys. Rev. Lett. **81** (1998) 1562, **82** (1999) 2644, and **85** (2000) 3999; C. Saji *et al.*, talk given at the Int. Workshop on Neutrino Oscillations and their Origin (NOON2004), February 11 - 15, 2004, Tokyo, Japan.

[51] SNO collaboration, Q.R. Ahmed et al., Phys. Rev. Lett. 87, 071301 (2001); Q.R. Ahmed et al., Phys. Rev. Lett. 89, 011301 (2002); nucl-ex/0204008. Q.R. Ahmed et al., Phys. Rev. Lett 89, 011302 (2002); nucl-ex/0204009; nucl-ex/0309004.

[52] SNO collaboration, S.N Ahmed et al . nucl-ex/0309004.

[53] KamLAND Collaboration, K. Eguchi *et al.*, Phys. Rev. Lett. **90** (2003) 021802; J. Detwiler, SLAC Summer Institute, July 2003, hep-ex/031100.

[54] LSND Collaboration, A. Aguilar *et al.*, Phys. Rev. **D**64 (2001) 112007; hep-ex/0104049.

[55] CHOOZ Collaboration, M. Apollonio *et al.*, Phys. Lett. **B466** (1999) 415, and Eur. Phys. J. **C27** (2003) 331.

[56] A. Bandyopadhyay, S. Choubey, S. Goswami, S.T. Petcov, D.P. Roy, Phys. Lett. **B583** (2004) 134.

[57] Palo Verde Collaboration, F. Boehm *et al.*, Phys. Rev. **D64** (2001) 1120.

[58] C. Weinheimer et al., Phys. Lett. B 460, 219 (1999); J. Bonn et al., Prog. Part. Nucl. Phys. 48, 133 (2002); C. Weinheimer, hep-ex/0210050.

[59] V.M. Lobashev et al.,Phys. Lett. B 460, 227 (1999); V.M. Lobashev et al., Nucl. Phys. Proc. Suppl. 91, 280 (2001).

[60] KATRIN Collaboration, A. Osipowicz et al., hep-ex/0109033; V.M. Lobashev, Nucl. Phys. A 719, 153 (2003).

[61] C.L. Bennet et al., astro-ph/0302207; D.N. Spergel et al., astro-ph/0302209.

[62] M. Tegmark et al., astro-ph/0310723.

[63] S.M. Bilenky and S.T. Petcov, hep-ph/0405237;

[64] S.M. Bilenky, A. Faessler and F. Simkovic, hep-ph/0402250;

[65] S. Pascoli and S.T. Petcov, Phys. Lett. **B544** (2002) 239;

[66] H. V. Klapdor-Kleingrothaus et al., Mod. Phys. Lett. A37 (2001) 2409.

[67] S. Simon, *Nature* **135** (1935) 763

[68] D.H. Andrews *et al., Phys. Rev.* **76** (1949) 154

[69] Y.B. Levinson, Phonon propagation with frequency down-conversion, in *Nonequilibrium Phonons in Nonmetallic Crystals, edited by W. Eisenmenger and A.Kaplyanskii, chap. 3, pp. 91-143, Elsevier Science Publishe B.V., Amsterdam, 1986*

[70] B. Taylor, H.J. Maris, C. Elbrum, Phys. Rev. Lett. **49** (1969) 416

[71] K.D. Irwin *et al., Rev. Sci. Instr.* **66** (1995) 5322 M.J. Penn *et al., Nucl. Instr. and Meth.* **A 364** (1995)118

[72] N.E. Both, B. Cabrera, E. Fiorini, *Ann. Rev. Part. Sci.* **46** (1996) 471

[73] U. Fano, *Phys. Rev.* **70** (1946) 44

[74] C.A. Klein, *J. Appl. Phys.* **39** (1968) 2029

[75] M. Mott, Can. J. Phys. 34 (1956) 1356

[76] E. Haller, J. Appl. Phys. 77 (1995) 2857

[77] A. Miller and E. Abrahams, Phys. Rev. 120 (1961) 761

[78] A. Alessandrello et al., Nucl. Instr. and Meth. A 412 (1998) 454

[79] C. Brofferio *et al., Nucl Phys. Proc. Suppl.* **48,** (1996) 238.

[80] A. Alessandrello *et al., Nucl. Phys.* **B 433** (1998) 156

[81] A.Alessandrello *et al.*, *Nucl. Instr. and Meth. in Phys. Res.* **A 440,** (2000), 397-402

[82] A. Giuliani and S. Sanguinetti, Mat. Sci. and Eng. R 11, 52 (1993).

[83] N. F. Mott. Phil. Mag. 19, 835 (1969).

[84] B. I. Shklovskii and A. L. Efros, Sov. Phys. - JETP 33, 468 (1971).

[85] A.Alessandrello et al., *Low Temp. Det. for Neutr. and Dark Matt. IV,* Ed. Frontieres, (1992) 447

[86] C.Arnaboldi et al., Phys. Lett. B 557 (2003) 167.

[87] F. Pobell, "Matter and Methods at Low Temperatures", Springer - Verlag, Berlin, 1992.

[88] E.Gatti and P.F.Manfredi, Rivista Nuovo Cimento 9 (1986) 1.

[89] W.H. Press, B.P. Flannery, S.A. Teukosky and W.T. Vetterling, *Numerical Recipes in C , The Art of Scientific Computing* - Cambridge University Press 1991

[90] J.A. Simpson *Ann. Rev. Nucl. Part. Sci. ,*33:323 (1983)

[91] *National Council on Radiation Protection and Measurement (NCRP)* Report Nr. 94, Bethesda (1987)

[92] T.K. Gaisser *Cosmic Rays and Particle Physics* Cambridge: University Press (1990)

[93] G.V. Gorshkov *et al.* Natural Neutron Background of the Atmospherre and the Earth Crust Moscow: Atomizdat (1966)

[94] C. Grupen *Zeitschrift Fortschritte der Physik* 23:127 (1976)

[95] C. Arpesella, Nucl. Phys. **A 28** (1992) 420-424

[96] P. Belli et al., Nuovo Cimento **A 101** (1989) 953

[97] M. Ivanovich, R.S. Harmon, *Uranium series disequilibrium: applications to earth, marine and environmental science.* Oxford: Clarendon, (1992)

[98] L. Zanotti, *J. Phys.* **17** (1991) 375

[99] H.L. de Vries, G.W. Bardensen, *Physica* 19:987 (1953)

[100] R.I. Weller, E.C. Anderson and Jr J.L. Barker *Nature* 206:1211 (1965)

[101] O.G. Bartels *Health Phys.* 28:189 (1975)

[102] R.I. Weller *Helath Phys.* 41:15 (1981)

[103] W.A. Kolb *Environment. Intern.* 14:367 (1988)

[104] A. Alessandrello *et al. ,* Nucl. Instr. and Meth. Phys. Res. B61:106 (1991)

[105] A. Alessandrello *et al. ,* Nucl. Instr. and Meth. Phys. Res. B83:539 (1991)

[106] A. Balish *et al., Phys. Lett.* B322:176 (1994)

[107] R.L. Brodzinski85, *et al.,* Nucl. Instr. and Meth. Phys. Res. *A239 (1985) 207*

[108] *Borexino Coll., Nucl.Instr. and Meth.in Phys. Res. A 406 (1998), 411.*

[109] *C.J. Martoff and P.D. Lewin,* Comput. Phys. Commun. 72 (1992)96

[110] http://wwwasd.web.cern.ch/wwwasd/geant4/

[111] A.Nucciotti, Milano Bicocca University researcher, Private Commun.

[112] S. Baker and P.D. Cousins., Nucl. Instrum. and Meth. 221 (1984) 437

[113] G.J. Feldman and R.D. Cousins, Phys. Rev. D57 (1998) 3873

[114] V.I. Tretyak and Yu.G. Zdezenko, Atomic Data and Nuclear Data Tables, 80 (2002) 83.

[115] F. Pinquemal et al.: Start up of the NEMO 3 experiment, hep-ph/0107005.

[116] C. Arnaboldi et al., Phys. Lett.B 584: 260-268 (2004).

[117] Prof. G. Heusser, Heidelberg Max Planck Institute, Private communication.

[118] Private communication.

[119] A. Alessandrello et al., Nucl. Instr. and Meth. B 142 (1998) 163-172.

[120] R. Silberberg and R. Tsao, Astrophys. J. Suppl. Ser. 220 (1973) 315

[121] D.W. Bardayan et al., Phys. Rev. C 55 (1997) 820; E. Norman, Poster Session Neutrino 2004, Paris.

[122] Admatechs Co. Ltd., Japan.

[123] V.Palmieri et al., "Electropolishing of seamless 1.5 GHZ OFHC copper cavities", Proc. of the 7th workshop on RF Superconductivity, Gif Sur Yvette, France 1995, B. Bonin ed., DIST CEA/SACLAY 96 080/1,**2**, 605; V.Palmieri et al., "Besides the standard Niobium bath chemical polishing", Proceedings of the 10th workshop on RF Superconductivity, Sept. 6-11 2001, Tsukuba, Japan, (2002) in press

[124] P.Trincherini, private communication.